# NEW PROBES OF COSMIC MICROWAVE

# BACKGROUND LARGE-SCALE ANOMALIES

by

**Simone Aiola**

B. Sc., University of Rome La Sapienza, 2010

M. Sc., University of Rome La Sapienza, 2012

M. Sc., University of Pittsburgh, 2014

Submitted to the Graduate Faculty of

the Kenneth P. Dietrich School of Arts and Sciences in partial

fulfillment

of the requirements for the degree of

**Doctor of Philosophy**

University of Pittsburgh

2016

UNIVERSITY OF PITTSBURGH

KENNETH P. DIETRICH SCHOOL OF ARTS AND SCIENCES

PHYSICS AND ASTRONOMY DEPARTMENT

This dissertation was presented

by

Simone Aiola

It was defended on

April 28th 2016

and approved by

Arthur Kosowsky, Dept. of Physics and Astronomy, University of Pittsburgh

Ayres Freitas, Dept. of Physics and Astronomy, University of Pittsburgh

Jeffrey Newman, Dept. of Physics and Astronomy, University of Pittsburgh

Glenn Starkman, Dept. of Physics, Case Western Reserve University

Andrew Zentner, Dept. of Physics and Astronomy, University of Pittsburgh

Dissertation Director: Arthur Kosowsky, Dept. of Physics and Astronomy, University of

Pittsburgh

# NEW PROBES OF COSMIC MICROWAVE BACKGROUND LARGE-SCALE ANOMALIES

Simone Aiola, PhD

University of Pittsburgh, 2016

Fifty years of Cosmic Microwave Background (CMB) data played a crucial role in constraining the parameters of the ΛCDM model, where Dark Energy, Dark Matter, and Inflation are the three most important pillars not yet understood. Inflation prescribes an isotropic universe on large scales, and it generates spatially-correlated density fluctuations over the whole Hubble volume. CMB temperature fluctuations on scales bigger than a degree in the sky, affected by modes on super-horizon scale at the time of recombination, are a clean snapshot of the universe after inflation. In addition, the accelerated expansion of the universe, driven by Dark Energy, leaves a hardly detectable imprint in the large-scale temperature sky at late times. Such fundamental predictions have been tested with current CMB data and found to be in tension with what we expect from our simple ΛCDM model. Is this tension just a random fluke or a fundamental issue with the present model?

In this thesis, we present a new framework to probe the lack of large-scale correlations in the temperature sky using CMB polarization data. Our analysis shows that if a suppression in the CMB polarization correlations is detected, it will provide compelling evidence for new physics on super-horizon scale. To further analyze the statistical properties of the CMB temperature sky, we constrain the degree of statistical anisotropy of the CMB in the context of the observed large-scale dipole power asymmetry. We find evidence for a scale-dependent dipolar modulation at $2.5\sigma$. To isolate late-time signals from the primordial ones, we test the anomalously high Integrated Sachs-Wolfe effect signal generated by superstructures in the universe. We find that the detected signal is in tension with the expectations from ΛCDM

at the $2.5\sigma$ level, which is somewhat smaller than what has been previously argued. To conclude, we describe the current status of CMB observations on small scales, highlighting the tensions between Planck, WMAP, and SPT temperature data and how the upcoming data release of the ACTpol experiment will contribute to this matter. We provide a description of the current status of the data-analysis pipeline and discuss its ability to recover large-scale modes.

**Keywords:** Cosmology, Cosmic Microwave Background, Temperature Anisotropies.

# TABLE OF CONTENTS

# LIST OF TABLES

# LIST OF FIGURES

# PREFACE

> [...] fatti non foste a viver come bruti,
> ma per seguir virtute e canoscenza.
>
> *Canto XVI, Inferno — Dante Alighieri*

This thesis is the final step of a wonderful four-year journey that would not have been possible without many people I had the privilege to encounter. I am extremely grateful to my adviser Arthur Kosowsky for his guidance, his encouragement, and the long afternoons spent talking science. His contagious enthusiasm for science has been a great motivation over the past four years and helped changing me from a student in cosmology to a cosmologist.

In the middle of my studies, I had the fortune to meet Jonathan Sievers (Jon), who welcomed me into the nitty-gritty of the data analysis, linear algebra, and Fourier-space magic. I am grateful to Jon for having brought me into the ACT map-making working group and for letting me use, improve, and sometimes break Ninkasi. I warmly thank all the ACT collaborators for trusting and improving my work over the past year and a half, and I specifically thank for their priceless help Francesco De Bernardis, Jo Dunkley, Matthew Hasselfield, Renee Hlozek, Thibaut Loius, Marius Lungu, Sigurd Naess, Lyman Page, and Suzanne Staggs.

I am grateful for having had the chance of collaborating with Craig Copi, Glenn Starkman, and Amanda Yoho, who always challenged my mind with interesting questions. I also thank Ayres Freitas, Jeff Newman, and Andrew Zentner for their precious suggestions and feedback during my thesis committee meetings.

Beyond all the great scientists I had the privilege to work with, I am thankful to all my friends who made these four years an amazing personal experience. I am grateful to Azarin Zarassi for having opened my mind to the beauty of the middle-eastern culture, for

# I. MOTIVATION AND THESIS SYNOPSIS

In the past three decades, the developments in detector technology and the establishment of new ground-based and space-based observatories have turned cosmology into a vibrant data-driven field. Mapping the sky at multiple wavelengths allows us to characterize the dynamics, energy content, and past and future of our universe. Therefore, we can test fundamental physics on a wide range of energy, length, and time scales, opening the era of precision cosmology. It is commonly assumed that the main scientific contribution from observational cosmology is constraining the parameters of the $\Lambda$CDM model. Indeed, the 2015 list of most cited papers of all time celebrates this task as one of the landmarks in the field, where the parameter constraints from supernovae [1, 2] and Cosmic Microwave Background anisotropies data [3] seem to suggest a remarkably simple universe. For the case of the Cosmic Microwave Background (CMB) radiation, the cosmological parameter constraints are mostly determined from temperature and polarization on small scales, as they are less affected by cosmic variance than the large-scale modes. However, several CMB "large-scale anomalies" have been identified in the temperature maps (for a recent review see [4]), and the findings are consistent between WMAP and Planck. This suggests that full-sky CMB maps contain more information on large scales than what is summarized by cosmological parameters, and the extra information can be exploited to test fundamental assumptions of our model [5, 6]. This thesis illustrates my contribution on defining novel methods to study and characterize the anomalous sky. My work features the synergy between the use of new statistical quantities on temperature data and the analysis of different cosmological observables. Specifically, we focus on (i) probing the measured large-scale suppression of the temperature correlation function with CMB polarization, (ii) characterizing the detected temperature power asymmetry by constraining the degree of large-scale dipole modulation,

1

and (iii) analyzing the anomalously high integrated Sachs-Wolfe signal generated by superstructures in the universe. In addition, this thesis benefits from a two-pronged research to leverage both theoretical and data-oriented analyses, which are currently focused on data from the Atacama Cosmology Telescope.

In Chapter II, we review the basics of the currently-accepted Standard Model of Cosmology, highlighting the connections between Inflation and Dark Energy with the CMB radiation. We describe the methods commonly used in CMB cosmology for isotropic Gaussian random fields and discuss how different statistical measures can be used to test the assumptions of our model. In Chapter III, we present theoretical estimates for the correlation functions of the CMB polarization fields. The analysis aims to test the measured lack of large-scale correlation in the temperature sky with a somewhat independent observable. In Chapter IV, we probe the degree of statistical anisotropy of the CMB temperature maps, by estimating the off-diagonal correlations between multipole moments. This work allows us to go beyond the usual statistical techniques that rely on the isotropy of the CMB field and to possibly explain the observed temperature power asymmetry. In Chapter V, we test the anomalously high integrated Sachs-Wolfe signal generated by superstructures in the universe. The integrated Sachs-Wolfe is only one of the physical processes giving rise to temperature fluctuations on large scales, making the understanding of temperature anomalies more puzzling. In Chapter VI, we present the maximum-likelihood mapping pipeline of the Atacama Cosmology Telescope used to make high-fidelity and high-resolution CMB maps. We report on the status of the current analysis of the data and how the upcoming scientific results will possibly shed light on the tensions between the Planck, WMAP, and South Pole Telescope data. We also discuss the main challenges for ground-based experiments that aim to recover the large-scale fluctuations. In Chapter VII, we provide a final summary of my work and prospects to move forward in the future.

## II.  INTRODUCTION

This chapter reviews the theoretical background of physical and observational cosmology, with particular focus on the CMB. The information here presented does not constitute original work, however it is fundamental in this thesis for sake of completeness and to introduce concepts that have then led to original work. Most of the figures in this chapter are plots of quantities computed with the public cosmological Boltzmann code CLASS [7].

## A.  THE STANDARD MODEL OF COSMOLOGY

The Standard Model of Cosmology, often called Lambda Cold Dark Matter ($\Lambda$CDM), consists of a spatially flat[1], homogeneous and isotropic universe on large scales. Initially hot and dense, the universe features four principal energy components: photons (relativistic species), baryonic matter, Dark Matter, and Dark Energy in the form of a cosmological constant $\Lambda$ [8]. The latter dominates the energy content of the universe at late times and is responsible for the current accelerated expansion. Inflation provides a mechanism to seed the structures we see today, which are originated from the hierarchical gravitational collapse of small over-densities generated in the early universe.

---

[1]Although flatness is by far the best-constrained property of our universe (see $\Omega_K$ constraints from CMB data [8]), the calculations in this chapter will not assume a spatially flat geometry. The purpose of this choice is to show how a curved geometry affects the expansion history of our universe and gives rise to particular features in the CMB temperature power spectrum.

## 1. Cosmic Dynamics: $H_0$, $\Omega_M$, $\Omega_\Lambda$, $\Omega_K$

As far as gravity is concerned, General Relativity is assumed to hold on cosmological scales, therefore the energy content of the universe affects the the spacetime curvature by means of Einstein's equations [9]. The cosmological principle (i.e. isotropy and homogeneity) allows us to restrict the family of possible solutions of Einstein's equations:

$$R_{\mu\nu} - \frac{1}{2}g_{\mu\nu}R = \frac{8\pi G}{c^4}\left(T_{\mu\nu} + \frac{\Lambda c^4}{8\pi G}g_{\mu\nu}\right), \tag{II.1}$$

leading to a diagonal Ricci tensor, $R_{\mu\nu}$. The metric tensor $g_{\mu\nu}$ for a homogenous and isotropic universe is described by the Friedmann-Lemaître-Robertson-Walker metric:

$$ds^2 = g_{\mu\nu}dx^\mu dx^\nu = -c\ dt^2 + a^2(t)\left[\frac{dr^2}{1 - kr^2} + r^2(d\theta^2 + \sin^2\theta d\phi^2)\right], \tag{II.2}$$

where $a(t) = r(t)/r(t_0)$ is the scale factor that describes the time-evolution of the spatial components of the metric tensor, and $k$ is the curvature parameter. In Eq. II.1, we can calculate the Ricci tensor $R_{\mu\nu}$ and the Ricci scalar $R$ from the metric tensor $g_{\mu\nu}$, whereas the stress-energy tensor $T_{\mu\nu}$ depends on the energy components featuring the universe. Assuming the four (or more) components to be perfect fluids, the stress-energy tensor simply becomes $T^\mu_\nu = \mathrm{diag}(-\rho, P, P, P)$, where the density $\rho$ and the pressure $P$ are the combined quantities for all the fluids present in the model (i.e. $\rho = \sum_i \rho_i$ and $P = \sum_i P_i$). This leads to the well-known Friedmann equations for the time-evolution of the scale factor:

$$H^2 = \left(\frac{\dot{a}}{a}\right)^2 = \frac{8\pi G}{3c^2}\sum_i \rho_i - \frac{kc^2}{a^2} + \frac{\Lambda c^2}{3}, \tag{II.3}$$

$$\frac{\ddot{a}}{a} = -\frac{4\pi G}{3c^2}\sum_i \left(1 + 3w_i\right)\rho_i + \frac{\Lambda c^2}{3}, \tag{II.4}$$

where Eq. II.4 has been obtained by using the equation of state for a perfect fluid, $w_i = P_i/\rho_i$. From the time derivative of Eq. II.3, it is straightforward to show that the density of each fluid evolves with the scale factor as $\rho_i(t) = \rho_i(t_0)\ a(t)^{-3(1+w_i)}$, highlighting the fact that each component dominates the energy budget at different times [10].

In order to present the current composition of the universe in a more intuitive way, it is useful to introduce dimensionless density parameters, $\Omega_i \doteq \rho_{i,t_0}/\rho_{cr,t_0}$, where $\rho_{cr}(t_0) = 3c^2 H_0^2/8\pi G \approx 1.88 H_0^2 10^{-33}$ g cm$^{-3}$. We can then rewrite Eq. II.3 as follows:

$$\left(\frac{H}{H_0}\right)^2 = \sum_i \Omega_{i,0} a^{-3(1+w_i)} - \frac{kc^2}{H_0^2 a^2},\qquad \text{(II.5)}$$

where we introduce the energy density for the cosmological constant to be $\Omega_\Lambda = \Lambda c^2/3H_0^2$. If we evaluate Eq. II.5 for $t = t_0$ we find that $\sum_i \Omega_i = 1 + kc^2/H_0^2$, which implies that a spatially flat universe (i.e. $k = 0$) has currently a total energy density $\rho = \rho_{cr,0}$.

In the context of $\Lambda$CDM, Eq. II.5 can be rewritten in a more explicit form by using the equations of state for each component: $w_r = 1/3$ for radiation, $w_M = 0$ for matter (both baryonic and Dark Matter), and $w_\Lambda = -1$ for the cosmological constant. This leads to:

$$H(z)^2 = H_0^2 \Big[ \Omega_r (1+z)^4 + \Omega_M (1+z)^3 + (1 - \Omega_r - \Omega_M - \Omega_\Lambda)(1+z)^2 + \Omega_\Lambda \Big],\qquad \text{(II.6)}$$

where we used the definition of cosmological redshift $z = 1/a - 1$, which is directly linked to the measurable Doppler shift of spectral lines of objects in the sky via $z = \Delta\lambda/\lambda_0$.

Current data from CMB temperature and polarization anisotropies, CMB lensing potential, Supernovae Ia and baryonic acoustic oscillations (see [8] and references therein) jointly constrain the parameters in Eq. II.6 to be: $H_0 = 67.74 \pm 0.46$, $\Omega_M = 0.3089 \pm 0.0062$, and $\Omega_\Lambda = 0.6911 \pm 0.0062$. The radiation component is usually neglected, but it can be estimated from the black-body temperature of the CMB spectrum, leading to $\Omega_r h^2 = \Omega_{\text{CMB}} h^2 \simeq 10^{-5}$. These values are obtained with the constraint of a flat universe (i.e. $\Omega_M + \Omega_\Lambda = 1$); however a 1-parameter extension to the $\Lambda$CDM model can be used to constrain $\Omega_K \doteq 1 - \Omega_M - \Omega_\Lambda$ resulting in $\Omega_K = 0.0008 \pm 0.0040$ (at 95% C.L.), showing that our universe looks remarkably flat.

## 2. Inflation: $A_s$, $A_t$, $n_s$, $n_t$, $r$

Cosmic inflation consists of a rapid exponential expansion of the universe at early times, assumed to be driven by a primordial scalar field that dominates the energy density of the universe before the radiation-domination era. This theory represents a possible mechanism to generate an extremely flat universe even from an otherwise curved initial state [11]. More importantly, inflation provides a compelling mechanism to produce curvature perturbations in the early universe from quantum fluctuations in the primordial scalar field, called the inflaton, which serve as initial conditions to the process of hierarchical structure formation.

Let us describe the physics of inflation in more detail to understand what prediction the theory makes and which tests we can develop (for a short review see [12]). If we consider a single-scalar-field inflation model, we can write down the Lagrangian associated with the inflaton field $\phi$ (assuming homogeneity) as $\mathcal{L} = (1/2)\dot{\phi}^2 - V(\phi)$, where the potential $V(\phi)$ is what characterizes a specific model of inflation. By means of Noether's theorem, we can calculate the energy density $\rho$ and the pressure $p$ from the Lagrangian under the assumption that the field behaves as prefect fluid (see Section II.A.1) and is spatially homogeneous. This leads to the following equations:

$$\left.\begin{array}{l} \rho = \frac{1}{2}\dot{\phi}^2 + V(\phi) \\ p = \frac{1}{2}\dot{\phi}^2 - V(\phi) \end{array}\right\} \rightarrow H^2 = \frac{8\pi G}{3c^2}\left[\frac{1}{2}\dot{\phi}^2 + V(\phi)\right] - \frac{kc^2}{a^2}, \tag{II.7}$$

In the last step, we used the density of the field $\phi$, which dominates the energy density of the universe, into Eq. II.5. We immediately notice that if $a$ grows by many orders of magnitude, the term $kc^2/a^2 \rightarrow 0$ leading to a spatially flat universe. Indeed, a fast accelerated expansion can be achieved under the slow-roll approximation, $\dot{\phi}^2 << V(\phi)$. In this case the ratio $\rho/p$ is negative and the scale factor will grow as $a \propto \exp\left(\int H(t)dt\right)$, where $H(t) \approx$ const for slowly varying potentials. The inflationary exponential expansion will stop only when the kinetic term becomes comparable to the potential $V(\phi)$ (i.e. the equation of state of the inflaton field evolves in time). In the final phase, called reheating, the field reaches the minimum of the potential and decays into all the standard model particles, thus starting the radiation-dominated era.

The presence of the inflaton field in the early universe is also responsible for (i) seeding the density fluctuations (i.e. galaxies, cluster of galaxies, filaments, voids) and (ii) generating a background of weak gravitational waves. This is possible because quantum fluctuations around the homogeneous solution for the inflaton field couple to metric fluctuations via Einstein's equations. If we assume the conformal Newtonian gauge and we ignore possible vector perturbations of the metric, the perturbed line element can be written as:

$$ds^2 = -(1 + 2\Phi)dt^2 + a^2(t)\Big[(1 - 2\Psi)\delta_{ij} + h_{ij}\Big]dx_i dx_j \tag{II.8}$$

where $\Phi$ and $\Psi$ are known as Bardeen potentials (or variables) and the term $h_{ij}$ describes tensor fluctuations, which can propagate as gravitational radiation [13]. For scalar fluctuations, it is useful to define the comoving curvature $\mathcal{R} = -\Psi - \frac{H}{\dot{\phi}}\delta\phi$, which connects the Bardeen potential, the dynamics (via $H$ in Eq. II.7), and the initial quantum fluctuations $\delta\phi$. Under the assumption of a homogeneous and isotropic universe, we seek to estimate only the variance of such fluctuations, which can be simply defined as:

$$\langle \mathcal{R}_k \mathcal{R}_{k'} \rangle = \frac{2\pi^2}{k^3} P_{\mathcal{R}}(k)\delta^3(k - k') \rightarrow P_s(k) \doteq P_{\mathcal{R}}(k) = \frac{1}{2\pi^2}\frac{V^3}{(V')^2}\Bigg|_{k=aH} \tag{II.9}$$

where the variance of each $k$ mode is defined at the horizon exit (i.e. $k = aH$).

Similar calculations can be carried out for tensor perturbations. The tensor $h_{ij}$ can be decomposed into two independent components $h_+$ and $h_\times$, and isotropy ensures that the amplitude of the tensor fluctuations is equally partitioned between these two components. This leads to

$$\langle h_{+,k} h_{+,k'} \rangle + \langle h_{\times,k} h_{\times,k'} \rangle = \frac{\langle h_k h_{k'} \rangle}{2} + \frac{\langle h_k h_{k'} \rangle}{2} = \langle h_k h_{k'} \rangle = \tag{II.10}$$

$$= \frac{2\pi^2}{k^3} P_h(k)\delta^3(k - k') \rightarrow P_t(k) \doteq 2P_h(k) = \frac{2}{3\pi^2}V\Bigg|_{k=aH}. \tag{II.11}$$

If we rescale the amplitude of the tensor perturbations relative to the amplitude of the scalar ones, we can estimate the characteristic scale at which inflation took place in the early universe as

$$E = 3.3 \times 10^{16} \ r^{1/4} \ \text{GeV}, \quad \text{where} \quad r = \frac{P_t(k_\star)}{P_s(k_\star)} \tag{II.12}$$

where we assumed a pivot scale $k_\star$ [14].

Constraining the full shape of the inflationary potential $V(\phi)$ would be extremely interesting, but not easy to achieve. A parametric description is often used for the scalar and tensor fluctuations power spectra in Eq. II.9 and Eq. II.10, which can be written as:

$$P_s(k) = A_s\left(\frac{k}{k_\star}\right)^{n_s-1}, \quad P_s(k) = rA_s\left(\frac{k}{k_\star}\right)^{n_t} \tag{II.13}$$

where $r, A_s, n_s, n_t$ are evaluated at the pivot scale $k_\star = 0.05 Mpc^{-1}$. Current data from CMB temperature and polarization anisotropies, CMB lensing potential, supernovae Ia and baryonic acoustic oscillations (see [8] and references therein) constrain the scalar perturbation parameters to be $10^9 A_s = 2.141 \pm 0.049$ and $n_s = 0.9667 \pm 0.0040$. These results indicate that the primordial power spectrum of the density perturbations is nearly scale-invariant, meaning that even on very large scales (i.e. small $k$) points in the sky are expected to be somewhat correlated. This concept will be further analyzed in Section II.B.1 and it motivates the analysis presented in Section III. For the tensor perturbations, the amplitude is limited to $r < 0.07$ (at 95% C.L.) from recent measurements of the CMB B-mode polarization by the the BICEP2/Keck team, which is consistent with no detection of primordial tensor modes [15].

### 3. Dark Energy: $\Omega_{DE}$, $w$

The presence of a cosmological constant in Eq. II.1 represents only one possible phenomenological description of a yet unknown dark component. Although introduced by Einstein to allow for a static solution to his set of equations, a non-zero value for the cosmological constant was first compellingly measured by using Supernovae Ia data [1, 2]. An independent analysis performed with CMB-only data by the Atacama Cosmology Telescope team confirmed this scenario [16], which is now part of the standard model of cosmology.

The effect of $\Lambda$ on the expansion history is to eventually produce an exponential expansion of the universe, such that $a(t) \propto \exp(H_0\sqrt{\Omega_\Lambda}t)$. Given the constraint on the value of $\Omega_\Lambda$ in Section II.A.1, this component started dominating the total energy density of the universe only at recent time for $z \simeq 0.3$, and leaves imprints in the CMB sky and in the distribution of matter on large scales (see section II.B.1 and V). From the theoretical point of view, particle

physics supports the presence of a cosmological constant by invoking the energy associated to the vacuum. However, theoretical estimates of the vacuum energy density overestimate the measured $\rho_\Lambda$ by many orders of magnitude [17].

Several other models that are based on the presence of a scalar field driving the expansion have been proposed (for a review see [18]). This class of models is particularly appealing especially after the discovery of a well-known scalar field particle, the Higgs boson, and also because such models resemble the main features of the Inflationary expansion (see Section II.A.2). For these reasons, the experimental effort is focused on constraining the Dark Energy equation of state and looking for departures from the value $w = -1$. For $w$CDM models, we need to modify the fourth term in Eq. II.6, such that $\Omega_\Lambda \to \Omega_{\mathrm{DE}}(1+z)^{3(1+w_{DE})}$, and we can further allow for time-evolution by Taylor expanding the equation of state as $w_{\mathrm{DE}} = w_0 + w_a(1-a)$ (see [19] and references therein). A 1-parameter extension of the ordinary $\Lambda$CDM model leads to the constraint of $w_{DE} = -1.019^{+0.075}_{-0.080}$ when using CMB, supernovae Ia, and baryonic acoustic oscillations data. 2-parameter extensions are also largely consistent with the standard case of $w_0 = -1$ and $w_a = 0$. However, it is worth pointing out that the constraining power of the current probes is not particularly powerful when applied to the $w_0 - w_a$ parameter space [8, 20].

## B.   THE COSMIC MICROWAVE BACKGROUND RADIATION

The Cosmic Microwave Background (CMB) was first serendipitously detected in 1965 by Arno Penzias and Robert Wilson, working on long-distance radio communications at the Bell Laboratories [21]. This radiation at a black-body temperature of about 3K is a relic of the initial hot and dense state of the universe; hence it provided the first compelling evidence for the Hot Big Bang model proposed by George Gamow in 1948 [22]. Theoretical estimates of the CMB black-body temperature from the early 1950's gave an upper limit of about 40 K, which was used as an experimental target for unsuccessful searches at the time. Initially classified by Penzias and Wilson as an unknown highly isotropic excess of antenna temperature, scientists from the Palmer Laboratory in Princeton first pointed out that the

detected uniform cold background was indeed the CMB [23].

In the early universe, protons $(p)$, electrons $(e^-)$, and photons $(\gamma)$ were tightly coupled. Protons and electrons interact via Coulomb scattering, whereas photons mainly interact with electrons by means of Compton scattering, maintaining the three species in thermal equilibrium via

$$p + e^- \leftrightarrow H + \gamma \tag{II.14}$$

$$e^- + \gamma \leftrightarrow e^- + \gamma. \tag{II.15}$$

The photo-baryonic fluid can therefore be described by a thermal distribution at a temperature $T$, common for all the species. As the universe expands and cools down, the density of photons with energy $E_\gamma > 13.6 eV$ (required to unbind the proton and electron in the hydrogen) drops, and the reaction in Eq. II.14 is no longer balanced, leading to $p + e^- \to H + \gamma$. This process, called recombination, happens at a redshift $z_{\text{rec}} \simeq 1400$ or $T_{\text{rec}} \simeq 3900$ K, when roughly 50% of the free electrons are combined with protons into hydrogen atoms[2]. Such a condition is not sufficient for the universe to be transparent. This means that the photon mean free path is smaller that the Hubble radius at the time. So, we can define the redshift of decoupling $z_{\text{dec}} \to \Gamma(z_{\text{dec}}) \simeq H(z_{\text{dec}})$, where $\Gamma$ is the electron-photon interaction rate and $H$ measures the expansion rate of the universe. This condition is satisfied at redshift $z_{\text{dec}} = 1089.90 \pm 0.23$ [8]. Fig. 1 shows the free electron fraction as function of the redshift. It is interesting to see that even though $z_{\text{rec}} \simeq z_{\text{dec}}$, the fraction of free electrons drops by roughly one order of magnitude before the universe becomes transparent.

If we assume that thermal equilibrium was maintained during recombination and decoupling (i.e. no process has injected energy into the photo-baryonic fluid before it could be thermalized), the spectral energy distribution of the CMB photons is described by Planck's law:

$$B_\nu(T) = \frac{2h\nu^3}{c^2} \frac{1}{e^{\frac{h\nu}{k_B T}} - 1}, \tag{II.16}$$

---

[2]We notice that the temperature of recombination $T_{\text{rec}} << 13.6 eV$. This phenomenon is due in part to the fact that we have roughly $10^9$ photons for each hydrogen atom, which means that the high-energy tail of the photon energy-distribution becomes important and needs to be taken into account when we estimate the temperature of recombination.
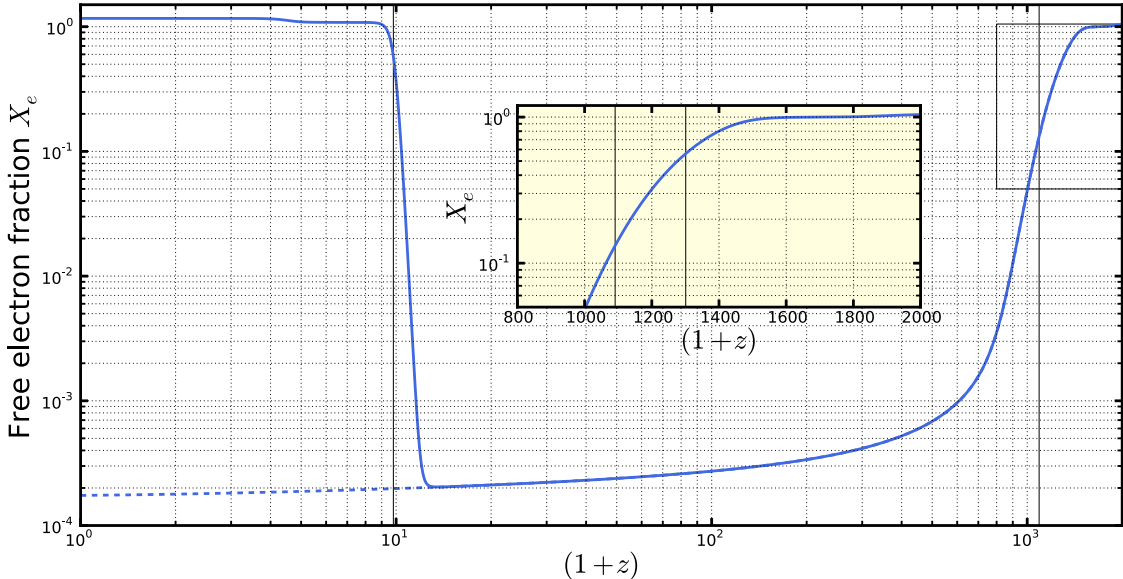
Figure 1: Fraction of free electrons in the universe $X_e$ as function of redshift. (Blue dashed line) standard recombination scenario and no reionization at later times. (Blue solid line) standard scenario with the effect of the cosmic reionization at redshift $z_{\mathrm{reio}} = 8.8$. (Inner panel) close up of the recombination and decoupling phases. Redshifts of reionization, decoupling, and recombination are indicated by black vertical solid lines. The fraction of free electrons is computed with the public cosmological Boltzmann code CLASS [7].

where $h$ is the Planck constant, $c$ is the speed of light, $k_B$ is the Boltzman constant, $T$ is the blackbody temperature, and $\nu$ is the frequency. The COsmic Background Explorer (COBE) made the first measurement of the CMB energy spectrum over the frequency range $\nu = 50 - 650$ GHz, showing that indeed thermal equilibrium was reached in the early universe [24, 25]. Fig. 2 shows the data overplotted on the best-fit blackbody curve with a temperature of $2.72548 \pm 0.00057$ K, where the residuals constrain possible departures from the blackbody spectrum to be $< 1\%$ [26].
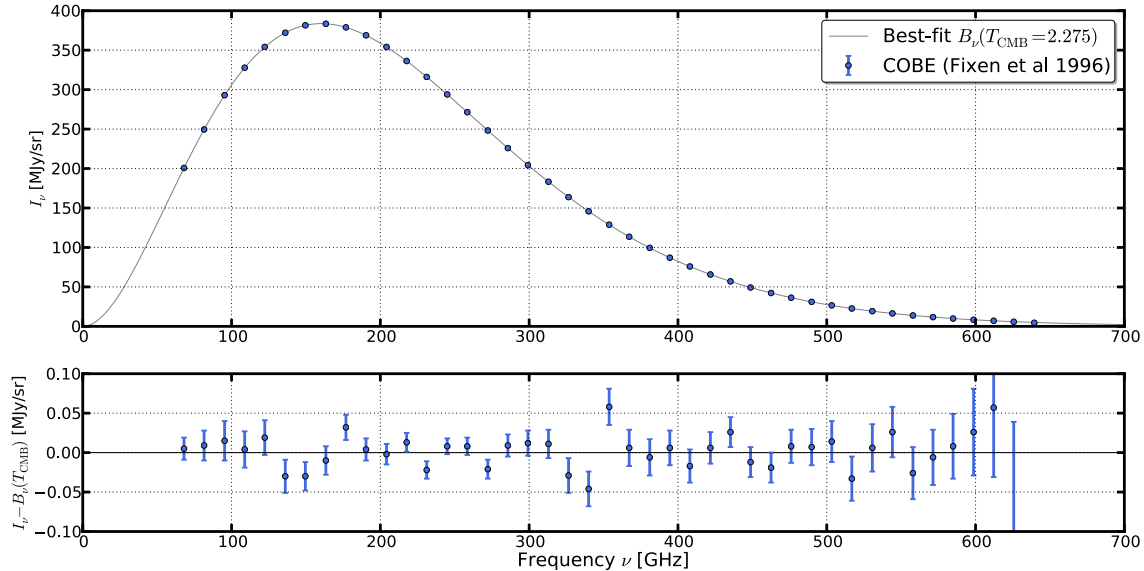
Figure 2: Spectral energy density of the CMB measured from the COBE satellite. (Top panel) the data is extremely well described by a black-body spectrum at a temperature of $T_0 = 2.72548 \pm 0.00057$ K. (Bottom panel) the residuals constrain spectral distortions to be less than 1%. Only in this case the experimental errorbars are visible showing a relative error $\Delta I_\nu / I_\nu \sim \mathcal{O}(10^{-4})$ for the peak of the spectrum. Data from [26] publicly available on the NASA/LAMBDA.

## 1. Temperature power spectrum

The CMB photons, tightly coupled with the baryonic matter before recombination, are expected to carry information on the density fluctuations generated at the end of inflation (see Section II.A.2). Indeed, the COBE satellite has also first observed tiny departures from the homogeneous blackbody temperature as function of the line-of-sight, generally called CMB temperature fluctuation[3] [27].

---

[3]Such temperature fluctuations are also called CMB temperature anisotropies. However, we will not adopt this terminology here to avoid confusion with the notion of statistical anisotropic Gaussian fields (see Section IV).

A complete picture of the CMB temperature sky can be summarized as:

$$T_{\text{obs}}(\hat{n}) = T_0 + (\vec{\beta} \cdot \hat{n})T_0 + T(\hat{n}), \tag{II.17}$$

where $T_0$ is the blackbody temperature of the smooth component, $\vec{\beta} = \vec{v}/c$ is our proper velocity vector with respect to the CMB rest frame (see Section 2.), and $T(\hat{n})$ is the CMB temperature fluctuation field. These fluctuations are of the order $\Delta T/T_0 = 10^{-5}$, which are roughly two orders of magnitude smaller than the kinetic dipole signal due to the Doppler boosting. Equation II.17 does not include the contribution from foreground emissions $F_\nu(\hat{n})$ that need to be taken into account when describing and analyzing actual data.

The stochastic nature of the quantum fluctuations during inflation does not allow us to develop a theory to exactly predict $T(\hat{n})$. Nevertheless, this problem can be suitably approached from a statistical point of view, as has been done for the description of the density fluctuation in Section II.A.2. A CMB temperature map, $T(\hat{n})$, can be uniquely decomposed in spherical harmonics $Y_{\ell m}(\hat{n})$, which define an orthonormal basis on a complete sphere, such that

$$T(\hat{n}) = \sum_{\ell=2}^{\infty} \sum_{m=-\ell}^{\ell} a_{\ell m}^T Y_{\ell m}(\hat{n}), \quad \text{where} \quad a_{\ell m}^T = \int d\Omega \, T(\hat{n}) Y_{\ell m}^\star(\hat{n}). \tag{II.18}$$

If $T(\hat{n})$ is a Gaussian real-valued random field, the harmonic coefficients are complex Gaussian random variables, which satisfy the following properties:

$$\langle a_{\ell m}^T \rangle = 0, \forall \ell, m, \tag{II.19}$$

$$\text{Isotropy} \Rightarrow \langle a_{\ell' m'}^{T\star}, \, a_{\ell m}^T \rangle = C_\ell^{TT} \, \delta_{\ell\ell'}\delta_{mm'}, \tag{II.20}$$

$$T(\hat{n}) \in \Re \Rightarrow a_{\ell-m}^T = (-1)^m \, a_{\ell m}^{T\star}. \tag{II.21}$$

where $\langle \cdots \rangle$ indicates an average over an ensemble of skies (i.e. different realizations of the $T(\hat{n})$ field), and $C_\ell^{TT}$ is the CMB temperature power spectrum. The cosmological principle constrains the covariance matrix of the harmonic coefficients to be diagonal. Off-diagonal correlations could cause different modes to align and introduce a preferred direction in the sky, hence breaking the statistical isotropy of the CMB field. Tests for statistical isotropy can be used to detect primordial mechanisms that violate isotropy and homogeneity (see Section IV.1).

The diagonal part of the covariance matrix, $C_\ell^{TT}$ summarizes all the statistical properties of CMB temperature field in $\Lambda$CDM. We thus need to estimate the power spectrum from a single realization of the sky. The commonly used power spectrum estimator can be written as

$$\widetilde{C_\ell^{TT}} = \frac{1}{2\ell+1} \sum_m |a_{\ell m}^T|^2, \tag{II.22}$$

which is unbiased (i.e. $\langle \widetilde{C_\ell^{TT}} \rangle \to C_\ell$) and described by a chi-square distribution with $2\ell+1$ degrees of freedom with diagonal covariance $\mathrm{diag}(\sigma_\ell^2) = C_\ell/(2\ell+1)$. This harmonic-space formalism can be nicely linked to the CMB temperature correlation function, $C(\hat{n}' \cdot \hat{n})$, that is the relevant summary statistics on the sphere. In real space (or pixel space), the covariance matrix between temperature values in different directions is

$$\langle T(\hat{n}'),\ T(\hat{n}) \rangle \overset{\text{Isotropy}}{\Longrightarrow} C(\hat{n}' \cdot \hat{n}) = \frac{2\ell+1}{4\pi} C_\ell^{TT} P_\ell(\hat{n}' \cdot \hat{n}). \tag{II.23}$$

In this case, a simple estimator for the correlation function is defined as $\tilde{C}(\hat{n}' \cdot \hat{n}) = \overline{T(\hat{n}')\ T(\hat{n})}$, with covariance matrix

$$\langle \tilde{C}(\theta_1)\tilde{C}(\theta_2) \rangle = \frac{1}{8\pi^2} \sum_\ell (2\ell+1)(C_\ell^{TT})^2\ P_\ell\big(cos(\theta_1)\big) P_\ell\big(cos(\theta_2)\big), \tag{II.24}$$

which is highly non-diagonal, and for this reason it is not commonly used in CMB parameter-estimation analyses.

We now need to construct a theoretical framework to compute the expected temperature power spectrum given a set of cosmological parameters (the derivation follows [28] and references therein). Consider the 3-dimensional temperature field observed at a given time, $T(\vec{x}, \eta)$ and its associated Fourier transform

$$T(\vec{x}, \eta) = \int \frac{d^3k}{(2\pi)^3} e^{i\vec{k}\cdot\vec{x}}\ T(\vec{k}, \eta). \tag{II.25}$$

where $\eta$ is the conformal time. The observed 2-dimensional temperature field generated at the last scattering surface can be written as the integrated effect of all the fluctuations along the line-of-sight as

$$T_{\mathrm{CMB}}(\hat{n}) = \int_{\eta_{\mathrm{in}}}^{\eta_0} d\eta\, T(\vec{x}, \eta) = \int_{\eta_{\mathrm{in}}}^{\eta_0} d\eta \int \frac{d^3k}{(2\pi)^3} e^{i\vec{k}\cdot(\eta-\eta_0)\hat{n}}\, T(\vec{k}, \eta) \tag{II.26}$$

14

where $\eta_0$ is the conformal time today and we wrote $\vec{x}$ in terms of the conformal distance $\eta - \eta_0$. Using Eq. II.18 and the plane wave expansion

$$e^{i\vec{k}\cdot x\hat{n}} = 4\pi \sum_{\ell m} i^\ell \; j_\ell(kx) \; Y_{\ell m}^\star(\hat{k}) Y_{\ell m}(\hat{n}), \tag{II.27}$$

we can write the harmonic coefficients as

$$a_{\ell m} = 4\pi \int_{\eta_{\rm in}}^{\eta_0} d\eta \int \frac{d^3 k}{(2\pi)^3} T(\vec{k}, \eta) \; i^\ell j_\ell(k(\eta - \eta_0)) Y_{\ell m}^\star(\hat{k}). \tag{II.28}$$

Under the assumption of linear perturbation theory and isotropy, we can write the photon perturbation power spectrum $\langle T^\star(\vec{k}, \eta), T(\vec{k}, \eta) \rangle = P_s(k)|S_T(k, \eta)|^2$, where $P_s(k)$ is simply the primordial scalar power spectrum from inflation in Eq. II.9 and all the evolution (which depends on the cosmological parameters) is described by the source function $S_T(k, \eta)$. Finally, the temperature power spectrum can be written as:

$$C_\ell^{TT} = 4\pi \int \frac{dk}{k} P_s(k)|\Theta_T(k, \eta_0)|^2, \tag{II.29}$$

where we defined the temperature transfer function for scalar perturbations as

$$\Theta_T(k, \eta_0) = \int_{\eta_{\rm in}}^{\eta_0} S_T(k, \eta) j_\ell(k(\eta - \eta_0)). \tag{II.30}$$

In the case of temperature fluctuations, the transfer function has four terms:

$$S(k, \eta) = g(\tau)\big(\Delta_\gamma + \Phi \; + \dot{v}_b^2\big) + 2e^{-\tau}(\dot{\Phi}) \tag{II.31}$$

where $\tau$ is the optical depth, $g(\tau)$ is the visibility function, and $e^{-\tau} \approx 1$ after decoupling. The $\Phi$ component is called the Sachs-Wolfe effect, which describes how photons trace the large-scale super-horizon modes of the gravitational potential. $\Delta_\gamma$ quantifies the intrinsic fluctuations of the photon field on sub-horizon scales. The $\dot{v}_b^2$ term represents the temperature fluctuations that are generated via the Doppler effect due to peculiar velocities of the photo-baryonic fluid. Finally, the $\dot{\Phi}$ term, called integrated Sachs-Wolfe effect, gives rise to fluctuations along the line-of-sight due to time-evolving gravitational potentials during radiation and dark energy domination [29]. Fig. 3 shows the four different temperature components independently plotted.

## 2. Polarization power spectrum

Cosmological information, which is complementary to the one extracted from CMB temperature statistics, can be obtained from the angular distribution of the linear polarization of the CMB photons (the derivation follows [30, 28] and references therein). For this reason, we need to introduce statistical quantities that describe the polarization of the CMB similarly to what we defined in section II.B.1. The polarization of light is commonly described by *Stokes parameters* I, Q, U, and V. If we consider a monochromatic wave that propagates in the direction $\hat{\mathbf{z}}$ with pulse $\omega_0$, the corresponding electric field can be written as

$$E_x(t) = a_x(t) \cos(\omega_0 t + \phi_x(t)) \tag{II.32}$$

$$E_y(t) = a_y(t) \cos(\omega_0 t + \phi_y(t)) \tag{II.33}$$

where $a_{x,y}(t)$ are the electric field amplitudes in the $\hat{\mathbf{x}}$ and $\hat{\mathbf{y}}$ directions, and $\phi_{x,y}(t)$ phases. The four Stokes parameters are functions of the electric field amplitudes, such that:

$$I = \langle a_x^2 \rangle + \langle a_y^2 \rangle \tag{II.34}$$

$$Q = \langle a_x^2 \rangle - \langle a_y^2 \rangle \tag{II.35}$$

$$U = \langle 2a_x a_y \cos(\theta_x - \theta_y) \rangle \tag{II.36}$$

$$V = \langle 2a_x a_y \sin(\theta_x - \theta_y)) \rangle \tag{II.37}$$

where $\langle ... \rangle$ indicates time average and we assumed that both the amplitudes and the phases are slowly varying functions of time. The parameter $I$ represents the intensity of the light, whereas the polarization is described by a non-zero value of the remaining 3 parameters. In particular, $Q$ and $U$ describe the linear polarization, while $V$ is a measure of the circular one that is not expected for the case of the CMB.

We now need to connect the measurable Stokes parameters to the physical mechanism that generates linear polarization of the CMB. Photons and electrons interact in the photo-baryonic plasma via Compton scattering, which does not induce polarization unless the intensity of the light scattering off of the electron is anisotropically distributed. The cross-section of the process can be written as

$$\frac{d\sigma}{d\Omega} = \frac{3\sigma_T}{8\pi} |\hat{\epsilon}' \cdot \hat{\epsilon}|^2 \tag{II.38}$$

16

where $\hat{\epsilon}' = (\hat{\epsilon}'_x, \hat{\epsilon}'_y)$ and $\hat{\epsilon} = (\hat{\epsilon}_x, \hat{\epsilon}_y)$ are the polarization vectors of the incident wave and the scattered one, respectively, defined in the plane perpendicular to the direction of propagation of the wave, $\hat{z}$. The $\hat{z}$-direction changes after the scattering by an angle $\theta$ defined in the plane that contains the propagation directions of the incoming and scattered waves. In this geometrical configuration, let us consider an initially unpolarized incident light, and let $I'$ and $I$ be the intensity of the incident and scattered light, respectively. For the scattered the intensity along the $\hat{x}$ and $\hat{y}$ directions can be written as $I_x = (I + Q)/2$ and $I_y = (I - Q)/2$, leading to:

$$I_x = \frac{3\sigma_T}{16\pi}\left[I'_x(\hat{\epsilon}'_x \cdot \hat{\epsilon}_x)^2 + I'_y(\hat{\epsilon}'_y \cdot \hat{\epsilon}_x)^2\right] = \frac{3\sigma_T}{16\pi}I' \tag{II.39}$$

$$I_y = \frac{3\sigma_T}{16\pi}\left[I'_x(\hat{\epsilon}'_x \cdot \hat{\epsilon}_y)^2 + I'_y(\hat{\epsilon}'_y \cdot \hat{\epsilon}_y)^2\right] = \frac{3\sigma_T}{16\pi}I' \cos^2\theta \tag{II.40}$$

which can be inverted to obtain the $I$ and $Q$ Stokes parameters of the scattered wave

$$I = I_x + I_y = \frac{3\sigma_T}{16\pi}I'\left(1 + \cos^2\theta\right), \tag{II.41}$$

$$Q = I_x - I_y = \frac{3\sigma_T}{16\pi}I' \sin^2\theta, \tag{II.42}$$

and $U$ can be calculated by rotating the reference frame by 45, therefore substituting $U$ with $Q$. The final expression for the three Stokes parameters of interest can be obtained by integrating over all possible incoming directions, thus obtaining

$$I = \frac{3\sigma_T}{16\pi}\int d\Omega(1 + \cos^2\theta)I'(\theta, \phi) \tag{II.43}$$

$$Q = \frac{3\sigma_T}{16\pi}\int d\Omega \sin^2\theta \cos(2\phi)I'(\theta, \phi) \tag{II.44}$$

$$U = \frac{3\sigma_T}{16\pi}\int d\Omega \sin^2\theta \sin(2\phi)I'(\theta, \phi) \tag{II.45}$$

Finally expanding $I'(\theta, \phi)$ in spherical harmonics, $I'(\theta, \phi) = \sum_{lm} a_{lm}Y^l_m(\theta, \phi)$, we obtain

$$I = \frac{3\sigma_T}{16\pi}\left(\frac{8}{3}\sqrt{\pi}a_{00} + \frac{4}{3}\sqrt{\frac{\pi}{5}}a_{20}\right), \tag{II.46}$$

$$Q - iU = \frac{3\sigma_T}{4\pi}\sqrt{\frac{2\pi}{15}}a_{22}. \tag{II.47}$$

17

These expressions show that the production of linear polarization is determined by the presence of a quadrupole term in the distribution of the intensity of the radiation around the electron.

Finally, we need to define statistical quantities that describe the distributions of Q and U Stokes parameters in the sky, which can compared with predictions based on the cosmological model. Using the transformation properties of the $Q$ and $U$ Stokes parameters under a rotation by an angle $\psi$ about the $\hat{z}$-axis, we can write the following combination

$$(Q \pm iU)'(\hat{\mathbf{n}}) = e^{\mp 2i\psi}(Q \pm iU)(\hat{\mathbf{n}}) \tag{II.48}$$

that can be decomposed in spin-2 spherical harmonics $_{\pm 2}Y^l_m(\hat{\mathbf{n}})$, giving

$$(Q + iU)(\hat{\mathbf{n}}) = \sum_{lm} a_{2,lm}\, _2Y_{lm}(\hat{\mathbf{n}}) \tag{II.49}$$

$$(Q - iU)(\hat{\mathbf{n}}) = \sum_{lm} a_{-2,lm}\, _{-2}Y_{lm}(\hat{\mathbf{n}}) \tag{II.50}$$

We can now define two independent quantities, called E-mode and B-mode such that

$$
\begin{aligned}
a^B_{lm} &= \tfrac{i}{2}\left[ _2a_{lm} - \, _{-2}a_{lm}\right] \\
a^E_{lm} &= -\tfrac{1}{2}\left[ _2a_{lm} + \, _{-2}a_{lm}\right],
\end{aligned}
\tag{II.51}
$$

with corresponding power spectra defined as

$$
\begin{aligned}
\langle a^E_{lm} a^{E*}_{l'm'}\rangle &= \delta_{ll'}\delta_{mm'}C^{EE}_l \\
\langle a^B_{lm} a^{B*}_{l'm'}\rangle &= \delta_{ll'}\delta_{mm'}C^{BB}_l \\
\langle a^T_{lm} a^{E*}_{l'm'}\rangle &= \delta_{ll'}\delta_{mm'}C^{TE}_l.
\end{aligned}
\tag{II.52}
$$

Fig. 4 shows the expected polarization power spectra from $\Lambda$CDM, where we have assumed no tensor modes. Even in the absence of a primordial tensor mode, CMB lensing induces a B-mode pattern from the initial E-mode pattern.
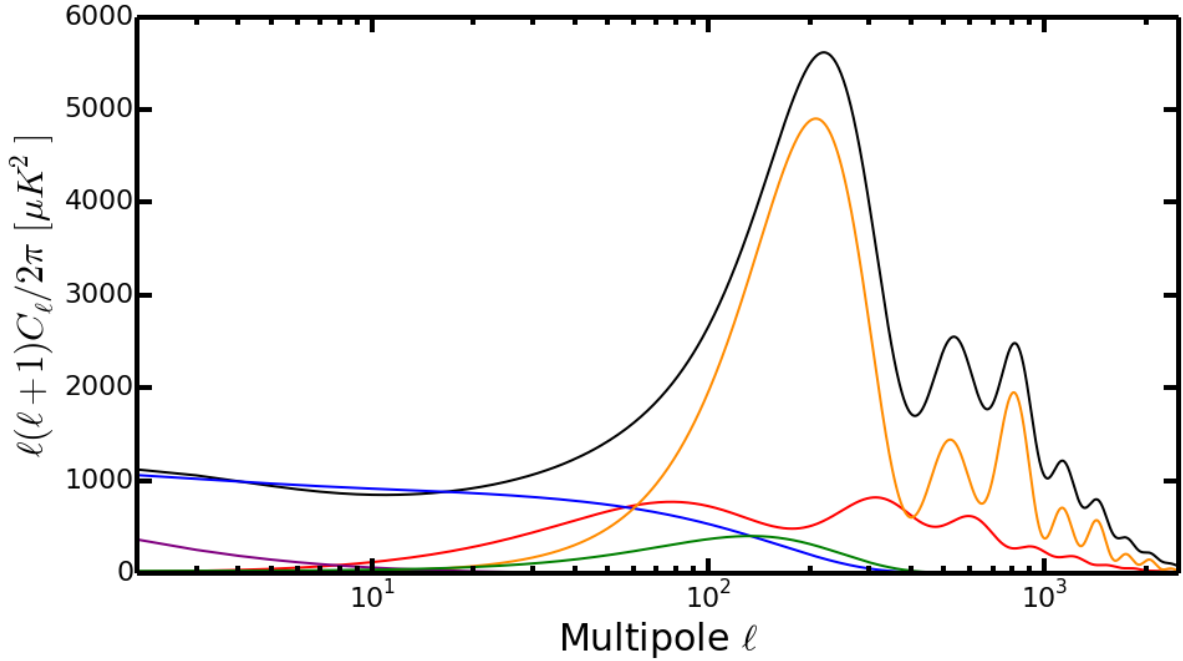
Figure 3: Total temperature power spectrum and each contributing component independently plotted. The black line describes the total, thus measurable, temperature power spectrum. The blue line describes the power generated via Sachs-Wolfe effect. The orange line describes the intrinsic component. The red line describes the power of the fluctuations generated via doppler effect due to peculiar velocities. Green and purple lines are the result of the integrated Sachs-Wolfe effect in the case of radiation domination and Dark Energy domination, respectively. The power spectra are computed with the public cosmological Boltzmann code CLASS [7].
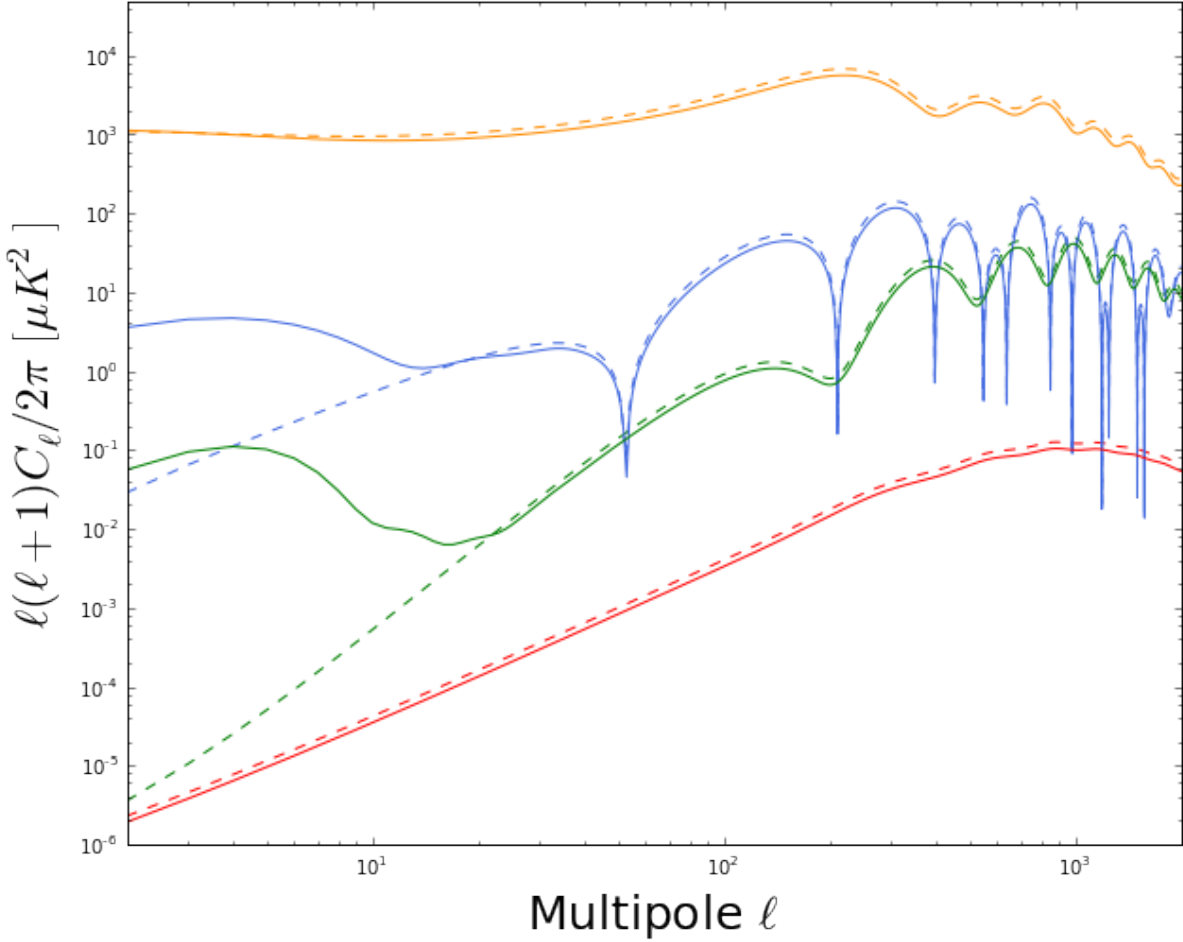
Figure 4: Temperature and polarization power spectra computed assuming Planck best-fit ΛCDM model. (Orange lines) temperature power spectrum. (Green lines) E-mode polarization power spectrum. (Red line) B-mode polarization power spectrum generated by lensing effect of the E-mode pattern. Tensor B-mode prediction from Inflation are neglected in this plot. (Blue lines) temperature and E-mode polarization correlation power spectrum. (Solid lines) power spectra include the effect of the cosmic reionization at redshift $z_{\mathrm{reio}} = 8.8$. This case correspond to what is measured in the sky. (Dashed lines) power spectra are computed neglecting the effect of the cosmic reionization, highlighting the dramatic large-scale loss of power for the E-mode polarizaion. The power spectra are computed with the public cosmological Boltzmann code CLASS [7].

# III.   MICROWAVE BACKGROUND POLARIZATION AS A PROBE OF LARGE-ANGLE CORRELATIONS

The content of this chapter was published in June 2015 in the Physics Review D journal and produced by the collaborative work of Amanda Yoho, Craig J. Copi, Arthur Kosowsky, Glenn Starkman, and myself [31]. ©2015 American Physical Society.

## A.   INTRODUCTION

Two seasons of observational data from the Planck satellite have given us the most precise measurement of temperature fluctuations in the Cosmic Microwave Background on the full sky to date [32, 33, 8]. These observations appear to fit well within the standard picture of our universe – Lambda Cold Dark Matter (ΛCDM). It did, however confirm several anomalous features in the temperature fluctuations [6], which had first been hinted at with the COBE-DMR satellite [34] and were later highlighted in the WMAP data releases [3]. These anomalies exist overwhelmingly at the largest scales of the temperature power spectrum, $C_\ell^{TT}$, with several interesting features appearing at multipoles $\ell \leq 30$. One feature, the lack of two-point correlation at angular separations of $60°$ and above, has garnered much attention recently [35, 36]. With decades of temperature measurements in hand, we know that this lack of correlation occurs only $0.03 - 0.1$ per cent of the time in ΛCDM realizations.

These large scales are also where cosmic variance, rather than statistical errors, is the limiting factor in our ability to compare the observed value of $C_\ell^{TT}$ to its theoretical value. This means that additional measurements of the temperature fluctuations will not help us make more definitive statements about the nature of the lack of correlation, and whether it

is a statistical fluke within our cosmological model or due to unknown physics. Work has been done recently to quantify the viability of using cross correlations of temperature with E-mode polarization [37] and the lensing potential $\varphi$ [38] to test this "fluke hypothesis."

Correlations of CMB polarization itself, outside of just cross correlations with the temperature observations, are a natural next step in determining the nature of the lack of temperature correlation seen at large angles. A feature that is required for a real-space correlation function is for the field to be calculated using only local operators on directly observed $Q$ and $U$ polarization maps. The very nature of a correlation function that has a clearly defined physical interpretation depends on points on the sky being determined independently of each other (i.e. locally).

To accomplish this, we calculate two sets of polarization correlation functions: $Q$ and $U$ auto-correlations along with $\hat{E}(\hat{\mathbf{n}})$ and $\hat{B}(\hat{\mathbf{n}})$ auto-correlations. These have a number of properties that make them unique tests of large-angle correlation suppression, such as contributions from the reionization bump that appear in polarization power spectra at $\ell \leq 10$ that dominate the large-angle $Q$ and $U$ functions. The local E- and B-mode correlations are instead dominated by large multipoles at large angles, and have small contributions from reionization which makes them a cleaner test of physics at the last scattering surface. In this work we present the local $C^{\hat{E}\hat{E}}(\theta)$ and $C^{\hat{B}\hat{B}}(\theta)$, along with $C^{QQ}(\theta)$ and $C^{UU}(\theta)$, and show distributions for the corresponding $S_{1/2}$ statistic for each. These results are drawn using constrained temperature realizations, meaning they are consistent with the observed power spectrum within instrumental errors and have a cut-sky $S_{1/2}$ at least as small as our cut-sky measurement.

This chapter is organized as follows: in Section III.B we present the theoretical background for $C(\theta)$ and a commonly discussed statistic $S_{1/2}$, in Section III.C we discuss our calculation of the error based on next-generation satellite specifications as well as the lowest possible expected instrument-limited value of $S_{1/2}$, in Section III.D we present the local E- and B-mode correlation functions, in Section III.E we show auto-correlation functions for Q and U Stokes parameters, and in Section III.F we present our conclusions and discuss possibilities for future work.

22

## B.   BACKGROUND

### 1.   Temperature Correlation Function and Statistics

The information contained in CMB temperature fluctuations is often represented in harmonic space by decomposing them in terms of spherical harmonics and their coefficients,

$$\frac{\Delta T(\hat{\mathbf{n}})}{T_o} \equiv \Theta(\hat{\mathbf{n}}) = \sum_{\ell,m} a_{\ell m}^T Y_{\ell m}(\hat{\mathbf{n}}), \tag{III.1}$$

with the temperature power spectrum being constructed from the $a_{\ell m}$ coefficients:

$$\langle a_{\ell m}^T a_{\ell' m'}^{T*} \rangle = \delta_{\ell \ell'} \delta_{mm'} C_\ell^{TT} \tag{III.2}$$

In real space, the CMB temperature fluctuations, $\Theta(\hat{\mathbf{n}})$, can be represented as a two-point correlation function averaged over the sky at different angular separations:

$$C^{TT}(\theta) = \overline{\Theta(\hat{\mathbf{n}}_1)\Theta(\hat{\mathbf{n}}_2)} \quad \text{with} \quad \hat{\mathbf{n}}_1 \cdot \hat{\mathbf{n}}_2 = \cos\theta. \tag{III.3}$$

This is an estimator of the quantity $C^{TT}(\theta) = \langle \Theta(\hat{\mathbf{n}}_1)\Theta(\hat{\mathbf{n}}_2) \rangle$, where the angle brackets represent an ensemble average. The sky average over the angular separation can be expanded in a Legendre series,

$$C^{TT}(\theta) = \sum_\ell \frac{2\ell+1}{4\pi} C_\ell^{TT} P_\ell(\cos\theta), \tag{III.4}$$

where the $C_\ell$ on the right-hand side of Eq. (III.4) are the pseudo-$C_\ell$ temperature power spectrum values.

The $S_{1/2}$ statistic was defined by the WMAP team to quantify the lack of angular correlation seen in temperature maps [3]:

$$S_{1/2}^{TT} \equiv \int_{-1}^{1/2} \mathrm{d}(\cos\theta)[C^{TT}(\theta)]^2. \tag{III.5}$$

The expression for $S_{1/2}$ can be written conveniently in terms of the temperature power spectrum and a coupling matrix $I_{\ell\ell'}$,

$$S_{1/2}^{TT} = \sum_{\ell=2}^{\ell_{max}} C_\ell^{TT} I_{\ell\ell'} C_{\ell'}^{TT}. \tag{III.6}$$

23

A full expression of the $I_{\ell\ell'}$ matrix can be found in Appendix B of [36]. The $C_\ell$ fall sharply and higher order modes have a negligable contribution to the statistic, so choice of an appropriately large value of $\ell_{\max}$ in Eq. (III.5) will ensure that the result is not affected by including additional higher-$\ell$ terms.

## 2. Stokes $Q$ and $U$ Correlation Functions and Statistics

Linear polarization is typically described by two quantities: the $Q$ and $U$ Stokes parameters in real space, and E-modes and B-modes in harmonic space. In real space, $C^{QQ}(\theta) = \langle Q_r(\hat{\mathbf{n}}_1)Q_r(\hat{\mathbf{n}}_2)\rangle$ and $C^{UU}(\theta) = \langle U_r(\hat{\mathbf{n}}_1)U_r(\hat{\mathbf{n}}_2)\rangle$ are the $Q$ and $U$ correlation functions, where $Q_r(\hat{\mathbf{n}})$ and $U_r(\hat{\mathbf{n}})$ are the Stokes parameters defined with respect to the great arc connecting $\hat{\mathbf{n}}_1$ and $\hat{\mathbf{n}}_2$ [30]. $Q(\hat{\mathbf{n}})$ and $U(\hat{\mathbf{n}})$ fields on the sphere are defined such that they are connected by a great arc of constant $\phi$. In practice, the correlation functions are calculated as an average over pixels separated by an angle $\theta$:

$$
\begin{aligned}
C^{QQ}(\theta) &= \overline{Q_r(\hat{\mathbf{n}}_1)Q_r(\hat{\mathbf{n}}_2)}, \\
C^{UU}(\theta) &= \overline{U_r(\hat{\mathbf{n}}_1)U_r(\hat{\mathbf{n}}_2)}.
\end{aligned}
\tag{III.7}
$$

The decomposition of polarization into spin-2 spherical harmonics is done with a linear combination of the Stokes parameters,

$$
(Q(\hat{\mathbf{n}}) \pm iU(\hat{\mathbf{n}})) = \sum_{\ell m} {}_{\pm 2}a_{\ell m}^P \, {}_{\pm 2}Y_{\ell m}(\hat{\mathbf{n}}).
\tag{III.8}
$$

The standard E- and B-mode coefficients are combinations of the spin-2 harmonic coefficients,

$$
\begin{aligned}
a_{\ell m}^B &= \tfrac{i}{2}\left[{}_2 a_{\ell m}^P - {}_{-2} a_{\ell m}^P\right] \\
a_{\ell m}^E &= -\tfrac{1}{2}\left[{}_2 a_{\ell m}^P + {}_{-2} a_{\ell m}^P\right],
\end{aligned}
\tag{III.9}
$$

and the E- and B-mode power spectra are defined as

$$
\begin{aligned}
\langle a_{\ell m}^E a^{E*}_{\ell' m'}\rangle &= \delta_{\ell\ell'}\delta_{mm'}C_\ell^{EE} \\
\langle a_{\ell m}^B a^{B*}_{\ell' m'}\rangle &= \delta_{\ell\ell'}\delta_{mm'}C_\ell^{BB}.
\end{aligned}
\tag{III.10}
$$

Using these equations, we can construct $C^{QQ}(\theta)$ and $C^{UU}(\theta)$ from $C_\ell^{BB}$ and $C_\ell^{EE}$ [30]:

$$C^{QQ}(\theta) = -\sum_\ell \frac{2\ell+1}{4\pi}\left(\frac{2(\ell-2)!}{(\ell+2)!}\right)\left[C_\ell^{EE}G_{\ell2}^+(\cos\theta) + C_\ell^{BB}G_{\ell2}^-(\cos\theta)\right] \qquad \text{(III.11)}$$

$$C^{UU}(\theta) = -\sum_\ell \frac{2\ell+1}{4\pi}\left(\frac{2(\ell-2)!}{(\ell+2)!}\right)\left[C_\ell^{EE}G_{\ell2}^-(\cos\theta) + C_\ell^{BB}G_{\ell2}^+(\cos\theta)\right], \qquad \text{(III.12)}$$

where

$$G_{\ell m}^+(\cos\theta) = -\left(\frac{\ell-m^2}{\sin^2\theta} + \frac{\ell(\ell-1)}{2}P_\ell^m(\cos\theta)\right) + (\ell+m)\frac{\cos\theta}{\sin^2\theta}P_{\ell-1}^m(\cos\theta), \qquad \text{(III.13)}$$

$$G_{\ell m}^-(\cos\theta) = \frac{m}{\sin^2\theta}\left((\ell-1)\cos\theta P_\ell^m(\cos\theta) - (\ell+m)P_{\ell-1}^m(\cos\theta)\right). \qquad \text{(III.14)}$$

The $G_{\ell m}^\pm(\cos\theta)$ are complicated functions of Legendre polynomials, so the calculation of $S_{1/2}^{QQ}$ and $S_{1/2}^{UU}$ is not a straightforward analog to Eq. (III.6). Instead, there will be three terms:

$$S_{1/2}^{QQ} = \sum_{\ell=2}^{\ell_{max}} C_\ell^{EE}I_{\ell\ell'}^{(1)}C_{\ell'}^{EE} + C_\ell^{BB}I_{\ell\ell'}^{(3)}C_{\ell'}^{BB} + 2C_\ell^{EE}I_{\ell\ell'}^{(2)}C_{\ell'}^{BB}, \qquad \text{(III.15)}$$

where for $S_{1/2}^{UU}$ the $I_{\ell\ell'}^{(1)}$ and $I_{\ell\ell'}^{(3)}$ are swapped. Full details of calculating the $I_{\ell\ell'}^{(i)}$ matrices is outlined in the appendix of [31].

### 3. E- and B-mode Correlation Functions and Statistics

The local correlation functions on the sky of the E- and B-modes are defined as

$$C^{\hat{B}\hat{B}}(\theta) = \langle\hat{B}(\hat{\mathbf{n}}_1)\hat{B}(\hat{\mathbf{n}}_2)\rangle$$
$$C^{\hat{E}\hat{E}}(\theta) = \langle\hat{E}(\hat{\mathbf{n}}_1)\hat{E}(\hat{\mathbf{n}}_2)\rangle. \qquad \text{(III.16)}$$

The $\hat{E}(\hat{\mathbf{n}})$ and $\hat{B}(\hat{\mathbf{n}})$ functions can be calculated from the observable Q and U fields using *local* spin raising and lowering operators $\bar{\partial}$ and $\partial$ [39]:

$$\hat{B}(\hat{\mathbf{n}}) = \frac{-\mathrm{i}}{2}\left[\bar{\partial}^2(Q(\hat{\mathbf{n}})+\mathrm{i}U(\hat{\mathbf{n}})) - \partial^2(Q(\hat{\mathbf{n}})-\mathrm{i}U(\hat{\mathbf{n}}))\right]$$
$$\hat{E}(\hat{\mathbf{n}}) = \frac{1}{2}\left[\bar{\partial}^2(Q(\hat{\mathbf{n}})+\mathrm{i}U(\hat{\mathbf{n}})) + \partial^2(Q(\hat{\mathbf{n}})-\mathrm{i}U(\hat{\mathbf{n}}))\right], \qquad \text{(III.17)}$$

where

$$\partial = -(\sin\theta)\left[\frac{\partial}{\partial\theta} + \left(\frac{i}{\sin\theta}\right)\frac{\partial}{\partial\phi}\right](\sin\theta)^{-1},$$

$$\bar{\partial} = -(\sin\theta)^{-1}\left[\frac{\partial}{\partial\theta} - \left(\frac{i}{\sin\theta}\right)\frac{\partial}{\partial\phi}\right](\sin\theta) \tag{III.18}$$

in real space, and in harmonic space,

$$\partial\ _sY_{\ell m} = \sqrt{(\ell-s)(\ell+s+1)}\ _{s+1}Y_{\ell m},$$

$$\bar{\partial}\ _sY_{\ell m} = -\sqrt{(\ell+s)(\ell-s+1)}\ _{s-1}Y_{\ell m}. \tag{III.19}$$

In terms of spherical harmonics and coefficients, $\hat{E}(\hat{\mathbf{n}})$ and $\hat{B}(\hat{\mathbf{n}})$ are [30, 39]:

$$\hat{B}(\hat{\mathbf{n}}) = \sum_{\ell m}\sqrt{\frac{(\ell+2)!}{(\ell-2)!}}\ a^B_{\ell m}Y_{\ell m}(\hat{\mathbf{n}})$$

$$\hat{E}(\hat{\mathbf{n}}) = \sum_{\ell m}\sqrt{\frac{(\ell+2)!}{(\ell-2)!}}\ a^E_{\ell m}Y_{\ell m}(\hat{\mathbf{n}}). \tag{III.20}$$

The prefactor under the square root is proportional to $\ell^4$, and is a direct consequence of using the local operators on the $Q$ and $U$ maps.

Real-space fields of E- and B-modes are occasionally presented as spin-zero quantities [40],

$$E(\hat{\mathbf{n}}) \equiv \sum_{\ell m}a^E_{\ell m}Y_{\ell m}(\hat{\mathbf{n}}),$$

$$B(\hat{\mathbf{n}}) \equiv \sum_{\ell m}a^B_{\ell m}Y_{\ell m}(\hat{\mathbf{n}}). \tag{III.21}$$

The fields in Eq. (III.21) *cannot* be constructed from real-space maps only, unlike Eq. (III.21), and require map filtering in harmonic space to separate the E- and B-modes. Because polarization is inherently a spin-2 quantity and an integral over the full sky is required to extract the $a^E_{\ell m}$ and $a^B_{\ell m}$ coefficients from Eqs. III.8 and III.9, the $E(\hat{\mathbf{n}})$ and $B(\hat{\mathbf{n}})$ are *non-local*. The non-local definitions of $E(\hat{\mathbf{n}})$ and $B(\hat{\mathbf{n}})$ require information from the full sky to separate the E- and B- modes from observed Q and U polarization maps in any given pixel. For this reason, non-local definitions cannot be used when talking about real-space

correlation functions, since the physical interpretation of a correlation at one particular point on the sky $\hat{\mathbf{n}}_1$ with another particular point on the sky $\hat{\mathbf{n}}_2$ becomes ambiguous.

The expression for the two point function in terms of the local fields is

$$C^{\hat{E}\hat{E}}(\theta) = \sum_\ell \frac{2\ell+1}{4\pi} \left( \frac{(\ell+2)!}{(\ell-2)!} \right) C_\ell^{EE} P_\ell(\cos\theta), \tag{III.22}$$

and the same for the local $\hat{B}$ correlation when substuting in $C_\ell^{BB}$. This form of the correlation function leads to some interesting conclusions, namely that the traditional mode of thinking that $\theta \sim \frac{1}{\ell}$ is not applicable. This intuition was due directly to the fact that $C_\ell^{TT}$ falls off as $1/\ell^2$ and the prefactor in the sum for the $TT$ correlation function in Eq. (III.4) only scales like $\ell$, leaving the sum dominated by terms less than an $\ell_{\max} = 30$. This does not hold for correlation functions of the $\hat{E}(\hat{\mathbf{n}})$ and $\hat{B}(\hat{\mathbf{n}})$ functions defined in Eq. (III.20), and it should be clear that higher $\ell$ modes will contribute to the large-angle piece of the correlation functions. This feature was also discussed in [40], where they were focused on small-angle correlation functions of local E- and B-modes.

The expressions for $S_{1/2}^{\hat{E}\hat{E}}$ and $S_{1/2}^{\hat{B}\hat{B}}$ are similar to Eq. (III.6):

$$S_{1/2}^{XX} = \sum_{\ell,\ell'=2}^{\ell_{max},\ell'_{max}} \left( \frac{(\ell+2)!}{(\ell-2)!} \right) C_\ell^{XX} I_{\ell\ell'} \left( \frac{(\ell'+2)!}{(\ell'-2)!} \right) C_{\ell'}^{XX}. \tag{III.23}$$

We have chosen to calculate the $S_{1/2}$ statistic, rather than generalizing to a statistic at another angle, because effects that contribute to polarization inside the surface of last scattering (namely reionization) are at a sufficiently high redshift that they do not significantly change the relevant angle where suppression is expected to appear.

Table 1: Polarization sensitivities that reflect the actual Planck sensitivity in CMB channels, and the design sensitivity for two satellite proposals.

| Experiment | $\sigma_P$ [$\mu$K arcmin] | $\theta_{\mathrm{FWHM}}$ [arcmin] |
|------------|---------------------------|-----------------------------------|
| Planck     | 120                       | 5                                 |
| PIXIE      | 3.78                      | 54                                |
| PRISM      | 3.4                       | 2                                 |

## C.  ERROR LIMITS ON MEASURING A SUPPRESSED $C(\theta)$ FOR FUTURE CMB POLARIZATION EXPERIMENTS

The error in $C_\ell$ for a next-generation full-sky CMB satellite can be determined using the relation

$$\Delta C_\ell = \sqrt{\frac{2}{2\ell+1}} \left( C_\ell + \frac{e^{\ell^2 \sigma_b^2} \sigma^2}{4\pi} \right), \tag{III.24}$$

where $\sigma$ is the pixel error estimate in $\mu$K $-$ arcmin [41]. Values for the pixel error estimates for future surveys are shown in Table 1 [42, 43, 44].

To find the corresponding error band in $C(\theta)$, we create $10^5$ realizations of the $C_\ell^{BB}$ spectrum assuming chi-squared distribution with variance including instrumental error based on the values in Table 1. Constrained realizations of $C_\ell^{EE}$ are generated by drawing $a_{\ell m}^E$ coefficients using instrument noise and assuming they are coupled to constrained realizations of $a_{\ell m}^T$.

The constrained temperature harmonic coefficients are drawn such that they produce $S_{1/2}$ values that are consistent with calculations from data and have a spectrum which matches observations (the full procedure for making constrained realizations is outlined in [37]). The errors to the mean correlation function values are determined based on the 68% confidence levels (C.L) for the realizations. Cosmic variance dominates the error bars on the E- and B-mode power spectra through the reionization bump ($\ell \leq 10$) and instrumental error from

beam size dominates around $\ell \sim 45$ for $r = 0.1$.

The instrumental error enforces a limit on the smallest possible value for the expectation $\langle S_{1/2} \rangle$, even if the correlation function is completely suppressed. If we assume that the correlation functions defined in Eqs. III.11 and III.22 are noise-free and identically zero above 60 degrees, then the corresponding sums over the power spectra and their coefficients must be zero for all $P_\ell(\cos\theta < 1/2)$. For both sets of correlation functions, this makes $S_{1/2}$ for $Q$, $U$, $\hat{E}$ or $\hat{B}$

$$S_{1/2} = \int_{-1}^{1/2} [\delta C^{XX}(\theta)]^2 \ \mathrm{d}\cos\theta. \tag{III.25}$$

In real-space, for $Q$

$$\delta C^{QQ}(\theta) = \frac{\sigma_P}{\sqrt{2 \, N_{\mathrm{pairs}}}} Q_{\mathrm{rms}}, \tag{III.26}$$

where $N_{\mathrm{pairs}}$ is the number of pixel pairs separated by $\theta$ and $Q_{\mathrm{rms}}$ is the root mean square value of the field. The integral is trivial since the only $\theta$ dependence appears in the expression for $N_{\mathrm{pairs}}$:

$$N_{\mathrm{pairs}} = \frac{1}{2} N_{\mathrm{pix}}^{3/2} \pi^{1/2} \sin\theta. \tag{III.27}$$

The zero true-sky value of $S_{1/2}$ is

$$S_{1/2}^{QQ} = \frac{3 \, \sigma_P^2 \, Q_{\mathrm{rms}}^2}{2 N_{\mathrm{pix}}^{3/2} \pi^{1/2}}. \tag{III.28}$$

This result is the same for the $U$ field, with $U_{\mathrm{rms}}$ substituted for $Q_{\mathrm{rms}}$.

For the E-mode statistics, it is easier to calculate $\delta C(\theta)$ in $\ell$-space:

$$\delta C^{\hat{E}\hat{E}}(\theta) = \frac{1}{\sqrt{8\pi N_{\mathrm{pairs}}}} \sqrt{\sum_{\ell\ell'} \left(\frac{(\ell+2)!}{(\ell-2)!}\right)^2 (2\ell+1)(2\ell'+1) C_\ell^{EE} N_{\ell'}^{EE}}. \tag{III.29}$$

This leads to

$$S_{1/2}^{\hat{E}\hat{E}} = \frac{3}{8(N_{\mathrm{pix}}\pi)^{3/2}} \sum_{\ell\ell'} C_\ell^{EE}(2\ell+1) \left(\frac{(\ell+2)!}{(\ell-2)!}\right)^2 N_{\ell'}^{EE}(2\ell'+1), \tag{III.30}$$

with the same result for $\hat{B}$ when $C_\ell^{BB}$ is substituted for $C_\ell^{EE}$, and using $N_{\ell'}^{BB} = N_{\ell'}^{EE}$.

In the near term, Planck will weigh in with its upcoming release of polarization data. We do not yet know the exact noise spectra for their $EE$ and $BB$ observations, but we can make an estimate of the expected $S_{1/2}$ values assuming $\sigma_{\mathrm{pol}} = \sqrt{2} \, \sigma_T$ and using $\sigma_T =$

Table 2: Expected values of $S_{1/2}$ statistic from a toy-model map with pixel noise using sensitivites from Table 1 and assuming complete suppression of the true correlation function for $Q$, $U$, $\hat{E}$, $\hat{B}$. These estimates account for sensitivities for future CMB polarization satellites.

| Experiment | $QQ/UU[\mu\mathrm{K}^4]$ | $\hat{E}\hat{E}[\mu\mathrm{K}^4]$ | $\hat{B}\hat{B}[\mu\mathrm{K}^4]$ |
|------------|------------------------|-----------------------------------|-----------------------------------|
| Planck | $1.75 \times 10^{-6}$ | $0.314$ | $0.013$ |
| PIXIE | $1.73 \times 10^{-9}$ | $3.10 \times 10^{-4}$ | $1.31 \times 10^{-5}$ |
| PRISM | $1.40 \times 10^{-9}$ | $2.51 \times 10^{-4}$ | $1.06 \times 10^{-5}$ |

$85\mu\mathrm{K} - \mathrm{arcmin}$ from [42]. Table 1 outlines error estimates used for Planck in addition to PIXIE [43] and PRISM [44], and Table 2 presents all values of the $S_{1/2}$ statistic that results from assuming there is zero true correlation at the last scattering surface for each experiment. These values show that, when compared to the $\Lambda$CDM prediction of $S_{1/2}$, pixel noise is not a significant source of error to quantifying suppression to the correlation functions in polarization. Systematic errors may bias measurements of $S_{1/2}$, but we will not consider these here as any unresolved systematic would only serve to *increase* the value of $S_{1/2}$. Currently, no full-sky polarization maps are reliable enough to measure the large-angle polarization functions computed here.

## D.   LOCAL $\hat{B}(\hat{\mathbf{N}})$ AND $\hat{E}(\hat{\mathbf{N}})$ CORRELATION FUNCTIONS

In order to present a meaningful correlation function and related statistics, we smooth the E- and B-mode power spectrum with a $\sigma = 2.7°$ Gaussian beam (which corresponds to a 0.02 radian beam). There are two benefits to this approach: it suppresses the $C_\ell^{BB}$ and $C_\ell^{EE}$ for $\ell \geq 50$ which ensures that the sum in Eq. (III.22) converges, and it suppresses all pieces of the power spectrum that have contributions from lensing. The former is necessary, since even for E- and B-mode power spectra with perfect de-lensing, the sum in Eq. (III.22)
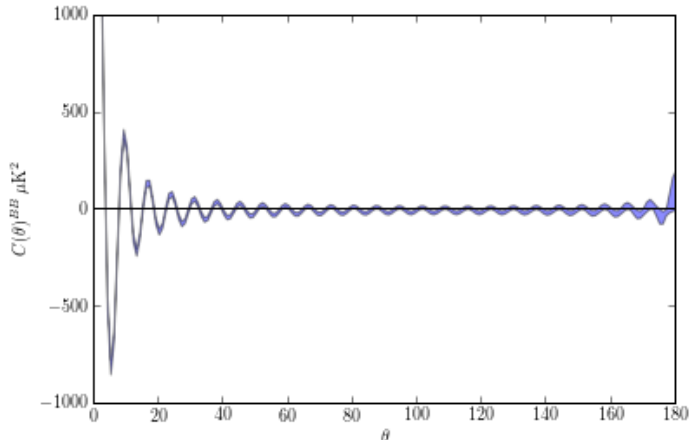
Figure 5: Angular correlation function of local B-modes $r = 0.1$ with $\sigma_{\text{beam}} = 2.7°$ smoothing. The blue shaded region corresponds to 68% C.L. errors, which includes instrumental noise for a future generation PIXIE-like experiment and cosmic variance using Eq. (III.24).

doesn't converge through $\ell_{\max} = 1500$. The latter is especially important since we wish to make statements about correlations of primordial E- and B-modes. Without smoothing we would need to de-lens all maps before calculating statistics. At the smoothing level used for analysis here, lensing does not contribute to the calculated $S_{1/2}$ distribution. Therefore all results used here have been produced from power spectra that do not include lensing effects. Figs. 5 and 6 show the resulting angular correlation function produced from the smoothed maps, and Figs. 7 and 8 show the distributions of $S_{1/2}$ statistics from simulations with $r = 0.1$ (smaller values of $r$ will lead to an appropriate rescaling of the $\hat{B}\hat{B}$ distribution, but will leave other results unchanged). For a $\Lambda$CDM cosmology, the best-fit value of $S_{1/2}^{\hat{E}\hat{E}}$ is $1.86 \times 10^5$ $\mu\text{K}^4$ and for $S_{1/2}^{\hat{B}\hat{B}}$ is 218.3 $\mu\text{K}^4$.

A feature of the correlation functions of $\hat{E}(\hat{\mathbf{n}})$ and $\hat{B}(\hat{\mathbf{n}})$ being dominated by large multipoles, even for large angular scales. These functions are also not sensitive to the physics of reionization, which make them a complimentary probe of correlation function suppression to the $Q$ and $U$ correlations presented in the following section.

## E.   $Q$ AND $U$ CORRELATIONS

The functions described in the section above may be undesirable in some cases, as they require taking derivatives of observations. The $Q$ and $U$ correlation functions do not require derivaties, and have the added benefit that they are entirely dominated by the reionization bump terms with $\ell \leq 10$, avoiding the need for map smoothing or concerns about contributions to the signal from lensing.

Fig. 9 shows the $QQ$ and $UU$ correlation functions for $r = 0.1$ for $\Lambda$CDM. The shaded regions show the 68% C.L. error regions for a PIXIE-like experiment plus cosmic variance calculated using Eq. (III.24). There are distinct characteristics of the $QQ$ and $UU$ functions, namely that the $UU$ correlation is positive for a large range of angles while the $QQ$ function is negative for a large range of angles. Physical suppression should drive both of these functions to zero. It could allow one to define additional measures of suppression of the correlation
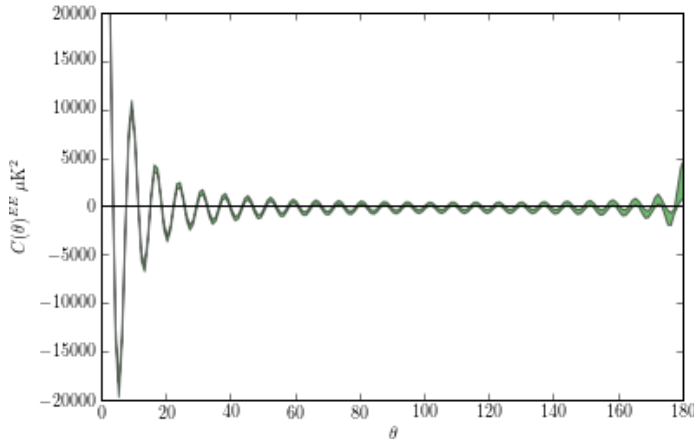


Figure 6: Angular correlation function of constrained local E-modes $r = 0.1$ with $\sigma_{\text{beam}} = 2.7°$ smoothing. The green shaded region corresponds to 68% C.L. errors, which includes instrumental noise for a future generation PIXIE-like experiment and cosmic variance using Eq. (III.24).
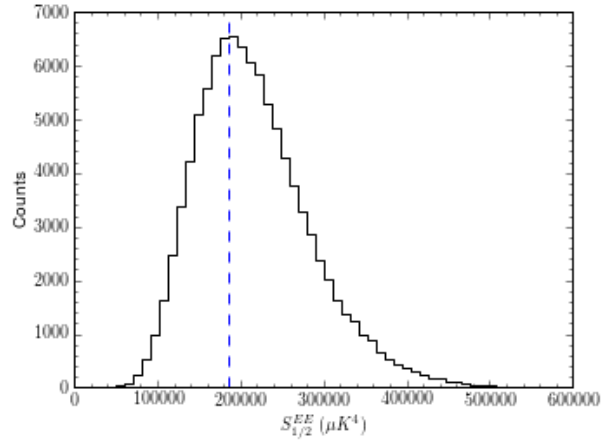
Figure 7: $S_{1/2}$ statistic distribution for the angular correlation function of E-modes $r = 0.1$ with $\sigma_{\mathrm{beam}} = 2.7°$ radian smoothing. The blue dashed line marks the $\Lambda$CDM prediction for the ensemble average.
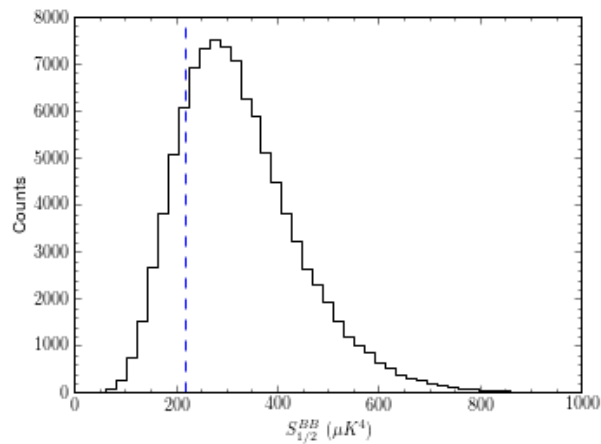


Figure 8: $S_{1/2}$ statistic distribution for the angular correlation function of B-modes $r = 0.1$ with $\sigma_{\mathrm{beam}} = 2.7°$ radian smoothing. The blue dashed line marks the $\Lambda$CDM prediction for the ensemble average.

function beyond the standard $S_{1/2}$ statistic.

Figs. 10 and 11 show the $S_{1/2}$ distributions for both the QQ and UU correlation functions. The $\Lambda$CDM value is shown with the blue dashed line. The expected $\Lambda$CDM value for $S_{1/2}^{QQ}$ is 0.0116 $\mu$K$^4$ and for $S_{1/2}^{UU}$ is 0.0129 $\mu$K$^4$.

In order to calculate $S_{1/2}$, the standard efficient methods defined in [37] cannot be used. Typically, Eq. (III.5) is expanded to instead be a function of the $C_\ell$s and a coupling matrix using Eq. (III.22) rather than calculating the integral of the square of $C(\theta)$ directly. Now, since Eq. (III.11) is in terms of $G_\ell^\pm(\cos\theta)$ rather than $P_\ell(\cos\theta)$ as in Eq. (III.22), the expressions for $S_{1/2}^{QQ}$ and $S_{1/2}^{UU}$ become more complicated. Appendix [31] describes a method that can be used to make the calculation more efficient by writing $G_\ell^\pm(\cos\theta)$ as functions of Wigner $d$-matrices.

The large-angle $Q$ and $U$ correlation functions being dominated by the reionization era, which is entirely inside the last scattering surface, give us a window into the nature of temperature suppression. The large-angle temperature correlation function has contributions from the last scattering surface via the Sachs-Wolfe effect, and along the line of sight via the integrated Sachs-Wolfe effect. The suppression of $C^{TT}(\theta)$, if caused by physics rather than a statistical fluke, could be due to features localized on the last scattering surface alone or could include contributions from its interior. If features inside the last scattering surface are suppressed, meaning suppression is a three-dimensional effect, this will manifest as suppression in the $Q$ and $U$ correlation functions.

We have chosen to calculate the standard $S_{1/2}$ statistic, rather than generalizing to statistics at another angle, $S(x)$, as defined in [37], since the reionization contribution is predominantly at $z = 10$, which is near enough to the surface of last scattering that the angular scale that features subtend are nearly that of those at $z = 1100$. Contributions from late-time reionization, which would skew the relevant angular scale, are subdominant since the amplitude of the polarization signal after $z_{\text{reion}}$ falls off like $a^{-2}$. This leads to an overall drop-off in the correlation function of $a^{-4}$, meaning nearby effects are 100 times smaller than those at $z = 10$.
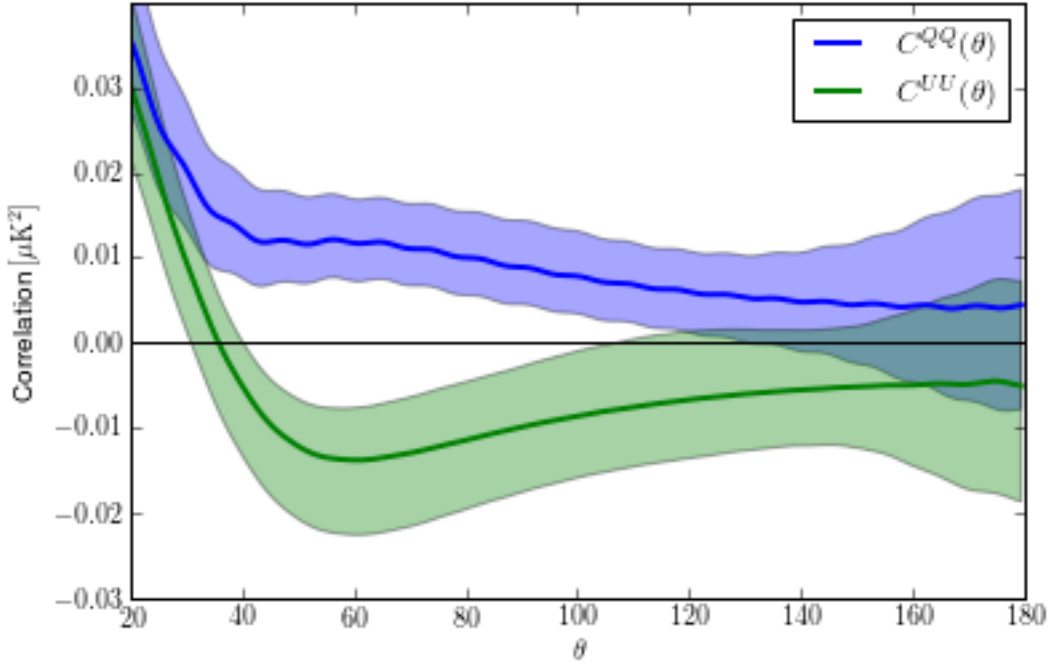
Figure 9: Angular correlation function of $Q$ and $U$ polarizations with $r = 0.1$. The shaded regions correspond to the 68% C.L. errors. The ranges include instrumental noise for a future generation PIXIE-like experiment and cosmic variance using Eq. (III.24).
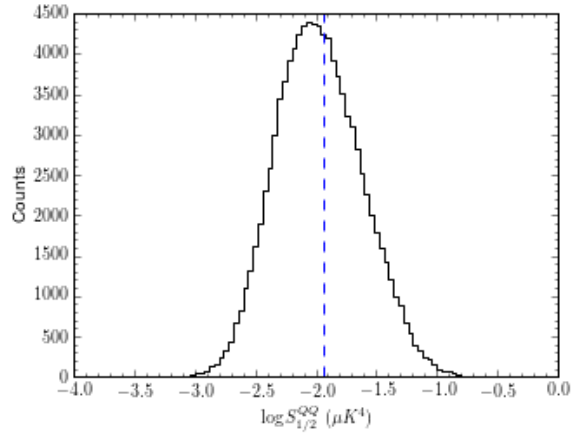
Figure 10: $S_{1/2}$ distribution for $C^{QQ}(\theta)$ with $r = 0.1$. The blue dashed line shows the $\Lambda$CDM prediction for the ensemble average.
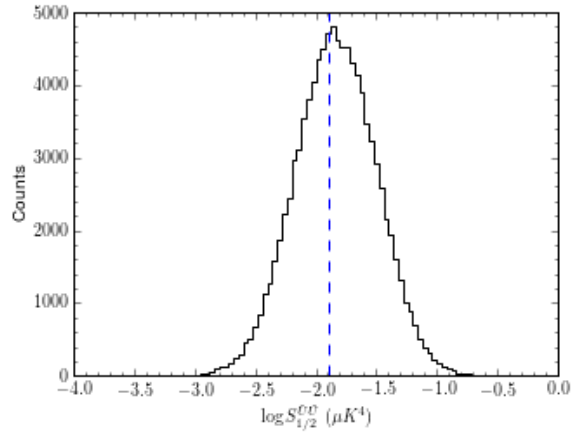


Figure 11: $S_{1/2}$ distribution for $C^{UU}(\theta)$ with $r = 0.1$. The blue dashed line shows the $\Lambda$CDM prediction for the ensemble average.

## F.   DISCUSSION

To address the lack of correlation in the temperature power spectrum at large angles in particular, we need to move beyond temperature data alone. We show two viable methods for calculating correlation functions on the sky that arise from polarization and presented the distributions for the corresponding statistics using constrained realizations for the E-mode contributions and the best-fit $\Lambda$CDM framework for B-mode realizations. A suppression in the primordial tensor or scalar fluctuations will affect the features of the two-point correlation function, meaning , local $C^{\hat{E}\hat{E}}(\theta)$ and $C^{\hat{B}\hat{B}}(\theta)$ as well as $C^{QQ}(\theta)$ and $C^{UU}(\theta)$, and their related statistical measures. This would lend considerable weight to the argument that the lack of correlation seen in $C^{TT}(\theta)$ is due to primordial physics, and is not just an anomalous statistical fluctuation of $\Lambda$CDM.

We presented the distribution for an $S_{1/2}$ statistic for a $C^{\hat{B}\hat{B}}(\theta)$ from $\Lambda$CDM cosmology with $r = 0.1$. If future limits on the value of $r$ are found to be significantly below this value, the results for $C^{\hat{B}\hat{B}}(\theta)$ will scale appropriately, wheras results for all other correlation functions will remain unchanged. For $C^{\hat{E}\hat{E}}(\theta)$, $C^{QQ}(\theta)$, and $C^{UU}(\theta)$, we considered constrained realizations, where $a_{\ell m}^E$ coefficients were related to $a_{\ell m}^T$ coefficients that match our power spectrum measurements and give values of $S_{1/2}^{TT}$ at least as small as we observe on the full- and cut-sky. We showed that for a $\Lambda$CDM cosmology, the expected values of the statistics for Stokes parameter correlation functions are $S_{1/2}^{QQ} = 0.0116\ \mu\mathrm{K}^4$ and $S_{1/2}^{UU} = 0.0129\ \mu\mathrm{K}^4$, and the local E- and B-mode expected values are $S_{1/2}^{\hat{E}\hat{E}} = 1.85 \times 10^5\ \mu\mathrm{K}^4$ and $S_{1/2}^{\hat{B}\hat{B}} = 218.3\ \mu\mathrm{K}^4$. We chose to keep the previously defined $S_{1/2}$ for analysis here, rather than generalizing to other angles than $\cos 60° = 1/2$, as the dominant secondary effect on polarization signals from epoch of reionzation is sufficiently close to the surface of last scattering to not change the relevant angle of suppression significantly. Late-time reionization contributes to the signal at a level 100 times smaller than the effect of reionization at $z = 10$, so while those would skew the relevant angular scales, they are subdominant.

Using a polarization error estimates for Planck, PIXIE and PRISM outlined in Table 1, we calculated the resulting $S_{1/2}$ statistics from a sky with exact suppression above 60°. These values are presented in Table 2. We note that these levels are well below the $\Lambda$CDM

predictions for all of the polarization correlation functions presented here, and pixel noise for future experiments will not be a significant source of error in identifying suppression. Measurement of large-angle polarization correlation functions will have errors dominated by systematics rather than map pixel noise for the foreseeable future.

Beyond being able to confirm that the suppression of temperature fluctuations is unlikely to be a statistical fluke, polarization correlation functions will add important new information. Because the local $\hat{E}$ and $\hat{B}$ correlation functions are dominated by large $\ell$ values, a suppression in all four correlation functions would strongly indicate that the suppression manifests itself physically in real-space at large angles. The $\hat{E}$ and $\hat{B}$ correlations give insight about suppression that is independent of any effects of reionization which dominate the $Q$ and $U$ correlations. Also, foreground emission will contribute differently to the various correlation functions.

Further, since the local $\hat{B}$ correlation is determined entirely by tensor fluctuations, a strong suppression in that correlation function and not in others would show that the primordial suppression is predominantly in the tensor perturbations, while suppressions in local $\hat{E}$, $Q$ and $U$ but not in local $\hat{B}$ would suggest that the scalar perturbations are suppressed.

The distribution for $S_{1/2}$ statistics for each constrained correlation function was compared to the distribution from $\Lambda$CDM alone. We found no significant difference between the two distributions and have presented only the constrained in this work. This means that polarization correlation functions provide a largely independent probe of correlations compared to the anomalous temperature correlation function. Future high-sensitivity measurements of polarization over large fractions of the sky from envisioned experiments like PIXIE [43] will differentiate primordial physics from a statistical fluke as the origin of this anomaly.

# IV.   MICROWAVE BACKGROUND CORRELATIONS FROM DIPOLE ANISOTROPY MODULATION

The content of this chapter was published in September 2015 in the Physics Review D journal and produced by the collaborative work of Bingjie Wang, Arthur Kosowsky, Tina Kahniashvili, Hassan Firouzjahi, and myself [45]. ©2015 American Physical Society.

## A.   INTRODUCTION

The statistical isotropy of the cosmic microwave background (CMB) at large angular scales has been questioned since the first data release of the WMAP satellite [46]. Independent studies performed on different WMAP data releases [47, 48, 49] show that the microwave temperature sky possesses a hemispherical power asymmetry, exhibiting more large-scale power in one half of the sky than the other. Recently, this finding has been confirmed with a significance greater than $3\sigma$ with CMB temperature maps from the first data release of the Planck experiment [42]. The power asymmetry has been detected using multiple techniques, including spatial variation of the temperature power spectrum for multipoles up to $l = 600$ [5] and measurements of the local variance of the CMB temperature map [50, 51]. For $l > 600$, the amplitude of the power asymmetry drops quickly with $l$ [52, 51].

A phenomenological model for the hemispherical power asymmetry is a statistically isotropic sky $\Theta(\hat{\mathbf{n}})$ times a dipole modulation of the temperature anisotropy amplitude,

$$\tilde{\Theta}(\hat{\mathbf{n}}) = (1 + \hat{\mathbf{n}} \cdot \mathbf{A}) \, \Theta(\hat{\mathbf{n}}), \tag{IV.1}$$

where the vector $\mathbf{A}$ gives the dipole amplitude and sky direction of the asymmetry [53]. This phenomenological model has been tested on large scales ($l < 100$) with both WMAP [54, 55] and Planck ([5], hereafter PLK13) data, showing a dipole modulation with the amplitude $|\mathbf{A}| \simeq 0.07$ along the direction $(\ell, b) \simeq (220°, -20°)$ in galactic coordinates, with a significance at a level $\geq 3\sigma$. Further analysis at intermediate scales $100 < l < 600$ shows that the amplitude of the dipole modulation is also scale dependent [56].

If a dipole modulation in the form of Eq. (IV.1) is present, it induces off-diagonal correlations between multipole components with differing $l$ values. Similar techniques have been employed to study both the dipole modulation [57, 56, 58, 59] and the local peculiar velocity [60, 61, 62, 63]. In this work, we exploit these correlations to construct estimators for the Cartesian components of the vector $\mathbf{A}$ as function of the multipole. These estimators are then applied to publicly available, foreground-cleaned Planck CMB temperature maps. We constrain the scale dependence over a multipole range of $2 \leq l \leq 600$, as well as determine the statistical significance of the observed geometrical configuration as a function of the multipole. Throughout this analysis, we adopt realistic masking of the galactic contamination. We test our findings against possible instrumental systematics and residual foregrounds.

This chapter is organized as follows: in Section IV.B, we derive estimators for the dipole modulation components and their variances for a cosmic-variance limited CMB temperature map. Section IV.C presents and tests a pipeline for deriving these estimators from observed maps, showing how to correct for partial sky coverage. Using simulated CMB maps, we estimate the covariance matrix of the components of the dipole vector, as well as test for possible systematic effects. Section IV.D describes the Planck temperature data we use to obtain the results in Sec. IV.E. We estimate the components of the dipole modulation vector and assess their statistical significance, finding departures from zero at the $2 - 3\sigma$ level. The best-fit dipole modulation signal is an unexpectedly good fit to the data, suggesting that we have neglected additional correlations in modeling the temperature sky. We also perform a Monte Carlo analysis to estimate how the dipole modulation depends on angular scale, confirming previous work showing the power modulation becoming undetectable for angular scales less than $0.4°$. Finally, Sec. IV.F gives a discussion of the significance of the results and possible implications for models of primordial perturbations.

## B. DIPOLE-MODULATION-INDUCED CORRELATIONS AND ESTIMATORS

Assuming the phenomenological model described by Eq. (IV.1), the dipole dependence on direction can be expressed in terms of the $l = 1$ spherical harmonics as

$$\hat{\mathbf{n}} \cdot \mathbf{A} = 2\sqrt{\frac{\pi}{3}} \left( A_+ Y_{1-1}(\hat{\mathbf{n}}) - A_- Y_{1+1}(\hat{\mathbf{n}}) + A_z Y_{10}(\hat{\mathbf{n}}) \right) \tag{IV.2}$$

with the abbreviation $A_\pm \equiv (A_x \pm iA_y)/\sqrt{2}$. Expanding the temperature distributions in the usual spherical harmonics,

$$\Theta(\hat{\mathbf{n}}) = \sum_{lm} a_{lm} Y_{lm}(\hat{\mathbf{n}}), \qquad \tilde{\Theta}(\hat{\mathbf{n}}) = \sum_{lm} \tilde{a}_{lm} Y_{lm}(\hat{\mathbf{n}}), \tag{IV.3}$$

with the usual isotropic expectation values

$$\langle a_{lm}^* a_{l'm'} \rangle = C_l \delta_{ll'} \delta_{mm'}. \tag{IV.4}$$

The coefficients must satisfy $a_{lm}^* = (-1)^m a_{l-m}$ and $\tilde{a}_{lm}^* = (-1)^m \tilde{a}_{l-m}$ because the temperature field is real. The asymmetric multipoles can be expressed in terms of the symmetric multipoles as

$$\tilde{a}_{lm} = a_{lm} + 2\sqrt{\frac{\pi}{3}} \sum_{l'm'} a_{l'm'} (-1)^m \times$$

$$\int d\hat{\mathbf{n}} \, Y_{l-m}(\hat{\mathbf{n}}) Y_{l'm'}(\hat{\mathbf{n}}) \left[ A_+ Y_{1-1}(\hat{\mathbf{n}}) - A_- Y_{1+1}(\hat{\mathbf{n}}) + A_z Y_{10}(\hat{\mathbf{n}}) \right]. \tag{IV.5}$$

The integrals can be performed in terms of the Wigner 3j symbols using the usual Gaunt formula,

$$\int d\hat{\mathbf{n}} Y_{l_1 m_1}(\hat{\mathbf{n}}) Y_{l_2 m_2}(\hat{\mathbf{n}}) Y_{l_3 m_3}(\hat{\mathbf{n}}) =$$

$$\sqrt{\frac{(2l_1+1)(2l_2+1)(2l_3+1)}{4\pi}} \begin{pmatrix} l_1 & l_2 & l_3 \\ m_1 & m_2 & m_3 \end{pmatrix} \begin{pmatrix} l_1 & l_2 & l_3 \\ 0 & 0 & 0 \end{pmatrix}. \tag{IV.6}$$

Because $l_3 = 1$ for each term in Eq. (IV.5), the triangle inequalities obeyed by the 3j symbols show that the only nonzero terms in Eq. (IV.5) are $l' = l$ or $l' = l \pm 1$. For these simple cases, the 3j symbols can be evaluated explicitly. Then it is straightforward to derive

$$\left\langle \tilde{a}^*_{l+1\,m\pm1} \tilde{a}_{lm} \right\rangle \;\; = \;\; \mp \frac{1}{\sqrt{2}} A_\pm \left( C_l + C_{l+1} \right) \sqrt{ \frac{(l \pm m + 2)(l \pm m + 1)}{(2l+3)(2l+1)} }, \qquad \text{(IV.7)}$$

$$\left\langle \tilde{a}^*_{l+1\,m} \tilde{a}_{lm} \right\rangle \;\; = \;\; A_z \left( C_l + C_{l+1} \right) \sqrt{ \frac{(l - m + 1)(l + m + 1)}{(2l+3)(2l+1)} }. \qquad \text{(IV.8)}$$

These off-diagonal correlations between multipole coefficients with different $l$ values are zero for an isotropic sky. This result was previously found by Ref. [57], and represents a special case of the bipolar spherical harmonic formalism [64].

It is now simple to construct estimators for the components of $\mathbf{A}$ from products of multipole coefficients in a map. Using $A_x = \sqrt{2}\mathrm{Re}A_+$ and $A_y = \sqrt{2}\mathrm{Im}A_+$, we obtain the following estimators:

$$[A_x]_{lm} \simeq \frac{-2}{C_l + C_{l+1}} \sqrt{ \frac{(2l+3)(2l+1)}{(l+m+2)(l+m+1)} }$$
$$\times \left( \mathrm{Re}\,\tilde{a}_{l+1\,m+1} \mathrm{Re}\,\tilde{a}_{lm} + \mathrm{Im}\,\tilde{a}_{l+1\,m+1} \mathrm{Im}\,\tilde{a}_{lm} \right), \qquad \text{(IV.9)}$$

$$[A_y]_{lm} \simeq \frac{-2}{C_l + C_{l+1}} \sqrt{ \frac{(2l+3)(2l+1)}{(l+m+2)(l+m+1)} }$$
$$\times \left( \mathrm{Re}\,\tilde{a}_{l+1\,m+1} \mathrm{Im}\,\tilde{a}_{lm} - \mathrm{Im}\,\tilde{a}_{l+1\,m+1} \mathrm{Re}\,\tilde{a}_{lm} \right), \qquad \text{(IV.10)}$$

$$[A_z]_{lm} \simeq \frac{1}{C_l + C_{l+1}} \sqrt{ \frac{(2l+3)(2l+1)}{(l+m+1)(l-m+1)} }$$
$$\times \left( \mathrm{Re}\,\tilde{a}_{l+1\,m} \mathrm{Re}\,\tilde{a}_{lm} + \mathrm{Im}\,\tilde{a}_{l+1\,m} \mathrm{Im}\,\tilde{a}_{lm} \right). \qquad \text{(IV.11)}$$

where the values for $\tilde{a}_{lm}$ are calculated from a given (real or simulated) map and the values for $C_l$ are estimated from the harmonic coefficients of the isotropic map $C_l = (2l+1)^{-1} \sum |a_{lm}|^2$. We argue that for small values of the dipole vector $\mathbf{A}$ and (more importantly) for a nearly full-sky map $\sum |\tilde{a}_{lm}|^2 \to \sum |a_{lm}|^2$. This assumption has been tested for the kinematic dipole

modulation induced in the CMB due to our proper motion, showing that the bias on the estimated power spectrum is much smaller than the cosmic variance error for nearly full-sky surveys [63]. Such estimators, derived under the constraint of constant dipole modulation, can be safely used for the general case of a scale-dependent dipole vector $\mathbf{A}$ by assuming that $\mathbf{A}(l) \simeq \mathbf{A}(l+1)$. This requirement is trivially satisfied by a small and monotonically decreasing function $\mathbf{A}(l)$.

To compute the variance of these estimators, assume a full-sky microwave background map which is dominated by cosmic variance; the Planck maps are a good approximation to this ideal. Then $a_{lm}$ is a Gaussian random variable with variance $\sigma_l^2 = C_l$. The real and imaginary parts are also each Gaussian distributed, with a variance half as large. The product $x = \mathrm{Re}\, \tilde{a}_{l+1\,m+1} \mathrm{Re}\, \tilde{a}_{lm}$, for example, will then have a product normal distribution with probability density

$$P(x) = \frac{2}{\pi \sigma_l \sigma_{l+1}} K_0 \left( \frac{2|x|}{\sigma_l \sigma_{l+1}} \right) \tag{IV.12}$$

with variance $\sigma_x^2 = \sigma_l^2 \sigma_{l+1}^2 / 4$, where $K_0(x)$ is a modified Bessel function. By the central limit theorem, a sum of random variables with different variances will tend to a normal distribution with variance equal to the sum of the variances of the random variables; in practice, the sum of two random variables, each with a product normal distribution, will be very close to normally distributed, as can be verified numerically from Eq. (IV.12). Therefore, we can treat the sums of pairs of $\tilde{a}_{lm}$ values in Eqs. (IV.9)-(IV.11) as normal variables with variance $\sigma_l^2 \sigma_{l+1}^2 / 2$, and obtain the standard errors for the estimators as

$$[\sigma_x]_{lm} = [\sigma_y]_{lm} \simeq \sqrt{\frac{(2l+3)(2l+1)}{2(l+m+2)(l+m+1)}}, \tag{IV.13}$$

$$[\sigma_z]_{lm} \simeq \frac{1}{2} \sqrt{\frac{(2l+3)(2l+1)}{2(l+m+1)(l-m+1)}}, \tag{IV.14}$$

with the approximation $C_{l+1} \simeq C_l$.

For a sky map with cosmic variance, each estimator of the components of $\mathbf{A}$ for a given value of $l$ and $m$ will have a low signal-to-noise ratio. Averaging the estimators with inverse

variance weighting will give the highest signal-to-noise ratio. Consider such an estimator for a component of $\mathbf{A}$, which averages all of the multipole moments between $l = a$ and $l = b$:

$$[A_x] \equiv \sigma_x^2 \sum_{l=a}^{b} \sum_{m=-l}^{l} \frac{[A_x]_{lm}}{[\sigma_x]_{lm}^2}, \tag{IV.15}$$

$$[A_y] \equiv \sigma_y^2 \sum_{l=a}^{b} \sum_{m=-l}^{l} \frac{[A_y]_{lm}}{[\sigma_y]_{lm}^2}, \tag{IV.16}$$

$$[A_z] \equiv \sigma_z^2 \sum_{l=a}^{b} \sum_{m=0}^{l} \frac{[A_z]_{lm}}{[\sigma_z]_{lm}^2}, \tag{IV.17}$$

which have standard errors of

$$\sigma_x = \sigma_y \equiv \left[ \sum_{l=a}^{b} \sum_{m=-l}^{l} [\sigma_x]_{lm}^{-2} \right]^{-1/2} = \left[ \frac{2}{3}(b+a+2)(b-a+1) \right]^{-1/2}, \tag{IV.18}$$

$$\sigma_z \equiv \left[ \sum_{l=a}^{b} \sum_{m=0}^{l} [\sigma_z]_{lm}^{-2} \right]^{-1/2}$$

$$= \left[ \frac{4(b-a+1)\left[a(2b+3)(a+b+4) + (b+2)(b+3)\right]}{3(2a+1)(2b+3)} \right]^{-1/2}. \tag{IV.19}$$

The sum over $m$ for the $z$ estimator and error runs from 0 instead of $-l$ because $[A_z]_{l-m} = [A_z]_{lm}$, but the values are distinct for the $x$ and $y$ estimators.

While the Cartesian components are real Gaussian random variables, such that for isotropic models $\langle [A_x] \rangle = \langle [A_y] \rangle = \langle [A_z] \rangle = 0$, the amplitude of $\mathbf{A}$ is not Gaussian distributed. Instead, it is described by a chi-square distribution with 3 degrees of freedom, which implies $\langle |\mathbf{A}|^2 \rangle \neq 0$ and $p(|\mathbf{A}|^2 = 0) = 0$, even for an isotropic sky. For this reason, we consider the properties of the dipole vector $\mathbf{A}$ as a function of the multipole, considering each Cartesian component separately.

44

## C. SIMULATIONS AND ANALYSIS PIPELINE

The estimators in Eqs. (IV.9)-(IV.11) are clearly unbiased for the case of a full-sky CMB map. However, residual foreground contaminations along the galactic plane as well as point sources may cause a spurious dipole modulation signal, which can be interpreted as cosmological. Such highly contaminated regions can be masked out, at the cost of breaking the statistical isotropy of the CMB field and inducing off-diagonal correlations between different modes. The effect of the mask, which has a known structure, can be characterized and removed.

### 1. Characterization of the Mask

For a masked sky, the original $a_{lm}$ are replaced with their masked counterparts:

$$\overline{a}_{lm} = \int \mathbf{d}\Omega \Theta(\hat{\mathbf{n}}) W(\hat{\mathbf{n}}) Y_{lm}^* \tag{IV.20}$$

where $W(\hat{\mathbf{n}})$ is the mask, with $0 \leq W(\hat{\mathbf{n}}) \leq 1$. In this case, Eq. (IV.4) does not hold, meaning that even for a statistical isotropic but masked sky the estimators in Eqs. (IV.9)-(IV.11) will have an expectation value different from zero. This constitutes a bias factor in our estimation of the dipole modulation.

If we expand Eqs. (IV.9)–(IV.11) using the definition of the harmonic coefficients in Eq. (IV.5), it is clear that if a primordial dipole modulation is present, the mask transfers power between different Cartesian components. Under the previous assumption $\mathbf{A}(l) \simeq \mathbf{A}(l+1)$, the Cartesian components $i, j = x, y, z$ of the dipole vector can be written as

$$[\overline{A}_j]_{lm} = \mathbf{\Lambda}_{ji,lm} A_{i,l} + M_{j,lm} \tag{IV.21}$$

where $[\overline{A}_j]_{lm}$ is the estimated dipole vector for the masked map, and $\mathbf{\Lambda}_{ji,lm}$ and $M_{j,lm}$ are Gaussian random numbers determined by the $\overline{a}_{lm}$, so they are dependent only on the geometry of the mask. For unmasked skies, these two quantities satisfy $\langle \mathbf{\Lambda}_{ji,lm} \rangle = \delta_{ij}$ and $\langle M_{j,lm} \rangle = 0$, ensuring that the expectation value of our estimator converges to the true value.

Using Eq. (IV.21), we can define a transformation to recover the true binned dipole vector from a masked map,

$$[A_i] = \mathbf{\Lambda}_{ji}^{-1}([\overline{A}_j] - M_j) \tag{IV.22}$$

where $[\overline{A}_j]$ is the binned dipole vector estimated from a map, and $\mathbf{\Lambda}_{ji}$ and $M_j$ are the expectation values of $\mathbf{\Lambda}_{ji,lm}$ and $M_{j,lm}$, binned using the prescription in Eqs. (IV.15)–(IV.17). For each Cartesian component we divide the multipole range in 19 bins with uneven spacing, $\Delta l = 10$ for $2 \leq l \leq 100$, $\Delta l = 100$ for $101 \leq l \leq 1000$. For a given mask, the matrix $\mathbf{\Lambda}_{ji}$ and the vector $M_j$ can be computed by using simulations of isotropic masked skies. We use an ensemble of 2000 simulations, and we adopt the apodized `Planck U73` mask, following the procedure adopted by PLK13 for the hemispherical power asymmetry analysis. For the rest of this work, all estimates of the dipole vector are corrected for the effect of the mask using Eq. (IV.22).

## 2. Simulated Skies

We generate 2000 random masked skies for both isotropic and dipole modulated cases. For the latter, we assume an scale-independent model with amplitude $|\mathbf{A}| = 0.07$, along the direction in galactic coordinates $(l, b) = (220°, -20°)$. We adopt a resolution corresponding to the `HEALPix`[1] [65] parameter `NSIDE` $= 2048$, and we include a Gaussian smoothing of `FWHM` $= 5'$ to match the resolution of the available maps. The harmonic coefficients $\tilde{a}_{lm}$ are then rescaled by $\sqrt{\tilde{C}_l}$, where the power spectrum is calculated directly from the masked map. These normalized coefficients (for both isotropic and dipole modulated cases) are then used to estimate the components of the dipole vector.

These simulations also serve the purpose of estimating the covariance matrix $\mathbf{C}$. From Eqs. (IV.9)-(IV.11), we expect different Cartesian components to be nearly uncorrelated, even for models with a nonzero dipole modulation, for full-sky maps. We confirm this numerically with simulations of unmasked skies. For masked skies, Fig. 12 shows the covariance matrices. The left panel shows the case for isotropic skies with no dipole modulation. The presence of the mask induces correlations between multipole bins at scales $100 \leq l \leq 500$,

---

[1] http://healpix.sourceforge.net/
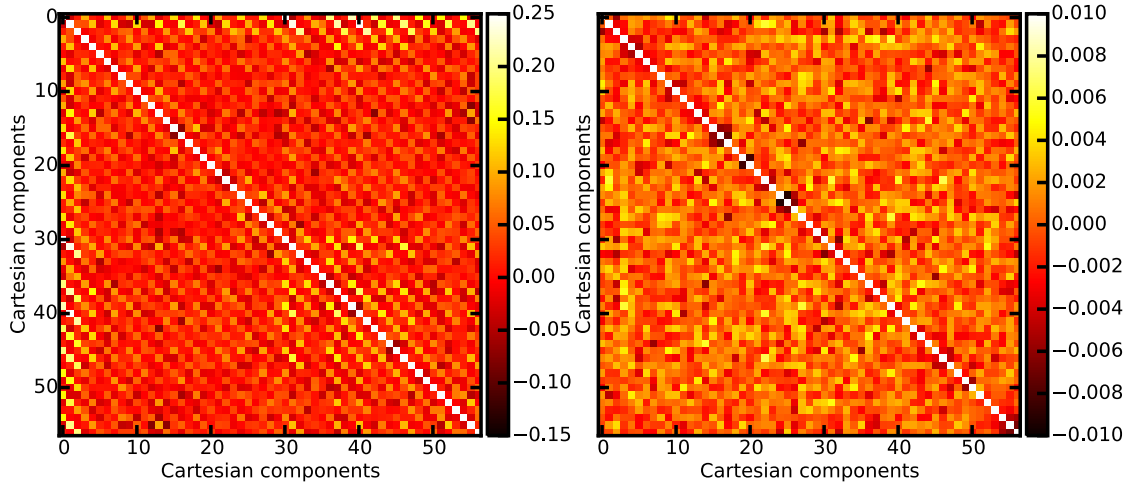
Figure 12: Correlation matrices for the Cartesian components of the dipole vector. These matrices are estimated using 2000 random simulated skies masked with the apodized Planck U73 mask. The ordering of the components follows the convention defined for the dipole vector. (Left panel) Isotropic skies ($\mathbf{A}$=0). (Right panel) Difference between the correlation matrices for modulated skies, generated using a constant dipole vector across multipoles of magnitude $|\mathbf{A}| = 0.07$ and direction $(\ell, b) = (220°, -20°)$, and isotropic skies.

and also between the largest scales $l \leq 40$ with all the other multipole bins. However, because of the apodization applied to the mask, the correlation between bins never exceeds 25%. For comparison, we also show the difference between the correlation matrices for the case of dipole modulated and isotropic skies (right panel). This is consistent with random noise, which demonstrates that the covariance matrix does not depend significantly on the amplitude of the dipole modulation.

## 3. Bias Estimates

We determine the mean bias in reconstructing the dipole modulation vector $\mathbf{A}$ from a masked sky by computing the mean value of all three Cartesian components reconstructed from 2000 simulations, for both isotropic and dipole-modulated skies. In both cases, the residual bias

47

vector has components $A_i > 0$, with an amplitude of the first bin of each Cartesian component below $6 \times 10^{-3}$. For the isotropic case, the amplitude of the bias is strongly decreasing with multipole ($|A(l = 60)| = 3.8 \times 10^{-4}$), corresponding to 0.5% to 2% of the cosmic variance error for the entire multipole range considered. Therefore, the analysis procedure on masked skies does not introduce a statistically any significant signal which could be mistaken for dipole modulation.

In the case of dipole-modulated simulations with dipole amplitude $A = 0.07$ consistent with PLK13 (see Sec. IV.C.3), the amplitude of the bias for each Cartesian component is a constant for all multipoles. This indicates that the bias follows the underlying model, and the determination of the scale dependence of the true dipole vector will not be affected by such a bias. For this specific case, the amplitude is always $\leq 0.8\sigma$ when compared to the cosmic variance, specifically $\leq 0.1\sigma$ for $l \leq 100$. However, this simulated case is unrealistic. We do not expect such a big amplitude for the dipole vector at small scales, so the simulated case overestimates the actual bias.

## D.   MICROWAVE SKY DATA

We consider a suite of six different foreground-cleaned microwave background temperature maps[2]: SMICA, NILC, COMMANDER-Ruler H, and SEVEM from the first Planck data release [66], and two others processed with the LGMCA[3] component separation technique from Ref. [67]. The LGMCA-PR1 and LGMCA-WPR1 are based on Planck data only and Planck+WMAP9 data, respectively, allowing a nontrivial consistency test between these two experiments. Each of these maps uses a somewhat different method for separating the microwave background component from foreground emission, allowing us to quantify any dependence on the component separation procedure.

Asymmetric beams and inhomogeneous noise may create a systematic dipolar modulation in the sky. In order to test this possibility, we analyze the 100 publicly available FFP6

---

[2]http://wiki.cosmos.esa.int/planckpla/index.php/Main_Page
[3]http://www.cosmostat.org/product/lgmca_cmb/

single-frequency simulated maps released by the Planck team. Specifically, we process the simulations for the 100, 143, and 217 GHz channels with our analysis code. The maximum likelihood analysis shows a bias on small scales, although the values are always less than 0.6 times the cosmic variance for each multipole bin. Considering only the first 15 bins ($l_{\mathrm{max}} = 600$) gives a result consistent with the isotropic case, with a p-value larger than 0.1. The source of the small-scale bias is not yet known, but we simply ignore multipoles $l > 600$ in the present analysis of Planck data.

## E. RESULTS

Fig. 13 shows the measured values of the Cartesian components of the dipole vector, using the SMICA map. Similar results are found for the other foreground-cleaned maps, and a direct comparison is shown in Section IV.E.1. Fig. 14 displays the amplitude of the dipole vector compared with the mean value (black dashed line) obtained from isotropic simulations; as pointed out in Section IV.B, the expectation value of the amplitude of the dipole vector is different from zero even for the isotropic case.

The data clearly show two important features:

- The amplitudes of the components of the estimated dipole vector are decreasing functions of the multipole $l$.
- The $x$ and $y$ components have a negative sign, which persists over a wide range of multipoles; the $z$ component is consistent with zero. This indicates that the vector is pointing in a sky region ($180° < \ell < 270°, b \simeq 0$), in agreement with previous analyses.

We further characterize these basic results in the remainder of this section.

### 1. Geometrical Test

First, we test how likely the observed geometrical configuration of the dipole vector is in an isotropic universe. To achieve this goal, we need to define a quantity which preserves the information on the direction of the dipole vector (i.e. statistics linear in the variables $A_i$).

In addition, the Cartesian components have to be weighted by the cosmic variance, ensuring that our statistics is not dominated by the first bins. Therefore, we define the following quantity

$$\alpha = \sum_{i=1}^{3N} (\mathbf{C}^{-1})_{ij} [A]_{j=1,\ldots,3N} \tag{IV.23}$$

where $(\mathbf{C}^{-1})_{ij}$ are the components of the inverse of the covariance matrix calculated in Sec. IV.C.2, and $[A]_{j=1,\ldots,3N}$ are the three Cartesian components of the binned dipole vector (up to the $N^{\text{th}}$ bin) estimated either from a simulated map of measured data. For an isotropic universe, we expect the three Cartesian components to sum up to zero, such that $\langle \alpha \rangle = 0$ for any choice of $l_{\max}$. This will not be the case if the underlying model is not isotropic (i.e. the expectation values of the Cartesian components are different from zero).

In Fig. 15, we plot the values of the $\alpha$ parameter as a function of the maximum multipole considered in the analysis $l_{max}$, rescaled by the standard deviation $\sigma(\alpha)$ determined from the simulations of isotropic skies. The left panel shows the comparison between the CMB data for all six foreground-cleaned maps, and the simulations for the isotropic case. The measured rescaled $\alpha$ parameter has a value that is discrepant from $\alpha = 0$ at a level of $2\sigma \leq \alpha < 3\sigma$. This discrepancy is maximized for $l \leq 70 - 80$, which corresponds to what has been previously probed by PLK13.

The right panel of Fig. 15 compares the measured signal with simulations of dipole modulated skies, using the covariance matrix $\mathbf{C}$ calculated from the anisotropic simulations. This test confirms that the signal averaged over multipoles $\leq 70$ is consistent with the model proposed by PLK13 (assumed in our anisotropic simulations). However, the results are not consistent with a scale-independent dipole modulation, and the amplitude of the dipole modulation vector must be strongly suppressed at higher multipoles.

## 2. Model Fitting

Consider a simple power-law model for the dipole modulation defined by four parameters:

$$A_x^{\mathrm{th}} = A\left(\frac{l}{60}\right)^n \cos b \cos \ell, \tag{IV.24}$$

$$A_y^{\mathrm{th}} = A\left(\frac{l}{60}\right)^n \cos b \sin \ell, \tag{IV.25}$$

$$A_z^{\mathrm{th}} = -A\left(\frac{l}{60}\right)^n \sin b, \tag{IV.26}$$

where $A$ is the amplitude of the dipole vector at the pivot scale of $l = 60$, $n$ is the spectral index of the power law, $b$ is the galactic latitude, and $\ell$ is the galactic longitude. We use a Gaussian likelihood $\mathcal{L}$, such that

$$\ln\mathcal{L} = -\frac{1}{2}\chi^2 = -\frac{1}{2}([A_i] - [A_i]^{\mathrm{th}})^{\mathrm{T}}(\mathbf{C}^{-1})_{ij}([A_j] - [A_j]^{\mathrm{th}}) \tag{IV.27}$$

where $[A_i]$ are the estimated components from the Planck SMICA map, $[A_i]^{\mathrm{th}}$ are the components of the assumed model properly binned using Eqs. (IV.15)-(IV.17), and $C$ is the covariance matrix for a dipole-modulated sky displayed in Fig. 12. The parameter space is explored using the Markov chain Monte Carlo sampler emcee[4] [68], assuming flat priors over the ranges $\{A, n\} = \{[0, 1], [-2, 2]\}$. Table 3 displays the results for different thresholds of $l_{\mathrm{max}}$. In the restricted case considering only low multipoles $l < 60$ and a flat spectrum $n = 0$, our best-fit model agrees at the $1\sigma$ level with previous analysis by PLK13, for both amplitude and direction.

If $n$ is allowed to vary, the amplitude $A$ of the dipole vector at the pivot scale of 60, as well as the spectral index $n$, is perfectly consistent for three different $l_{\mathrm{max}}$ thresholds. The amplitude is different from the isotropic case $A = 0$ at a level of $2\sigma$, and the scale-invariant case $n = 0$ with $l_{\mathrm{max}} = 400$ is excluded at greater than $3\sigma$ significance. The value of the galactic longitude $\ell$ is stable to a very high degree, whereas the value of the galactic latitude $b$ indicates (although not statistically significant) a migration of the pointing from the southern hemisphere to the northern one. This is expected because of the effect of the kinematic dipole modulation induced by the proper motion of the solar system with respect to the microwave background rest frame [69, 60]. This effect has been detected by Planck

---

[4]http://dan.iel.fm/emcee/current/

[62], and results in a dipole modulation in the direction $(\ell, b) = (264°, 48°)$ detectable at high $l$.

The dipole model is a better fit to the data than isotropic models. Both the Aikake information criterion (AIC) and the Bayes information criteron (BIC) [70] show sufficient improvement in the fit to justify the addition of four extra parameters in the model. In the specific case of the AIC, the dipole model is always favored. The improvement is calculated by the relative likelihood of the isotropic model with respect to the dipole modulated case. This is defined as $\exp((\text{AIC}_{\min} - \text{AIC}_{A=0})/2)$, where the AIC factor is corrected for the finite sample size, and it corresponds to $0.48, 0.083, 0.13, 0.18, 0.013$ and $0.011$ for the models considered in Table 3. In the case of the BIC, the corresponding values of $\text{BIC}_{\min} - \text{BIC}_{A=0} = -0.5, -0.4, 1.0, 2.1, -2.8$ and $-2.8$. The BIC indicates that the dipole modulation is favored only for the cases with $\ell_{\max} > 400$, where the parameters are better constrained. According to Ref. [71], the improvement even though positive is not strong because $-6 < \text{BIC}_{\min} - \text{BIC}_{A=0} < -2$.

For the dipole-modulated model, the value of $\chi^2$ is substantially lower than the degrees of freedom. This suggests that either the error bars are overestimated, or the data points have correlations which have not been accounted for in the simple dipole model. Since the errors are mostly due to cosmic variance on the scales of interest, the error bars cannot have been significantly overestimated. Therefore, our results may point to additional correlations in the microwave temperature pattern beyond those induced by a simple dipole modulation of Gaussian random anisotropies. The correlations are unlikely to be due to foregrounds, since the results show little dependence on different foreground removal techniques.

## F. DISCUSSION

The microwave sky seems to exhibit a departure from statistical isotropy, due to half the sky having slightly more temperature fluctuation power than the other half. This work shows that the temperature anisotropies are consistent with a dipolar amplitude modulation, which induces correlations with multipole coefficients with $l$ values differing by one. At angular

scales of a few degrees and above, the correlations define a dipole direction which corresponds to the orientation of the previously known hemispherical power asymmetry, while at smaller scales the direction migrates to that of the kinematic dipole. Our results show that a dipole modulation is phenomenologically a good description of the power asymmetry, but that the modulation must be scale dependent, becoming negligible compared to the kinematic dipole correlations [60, 62] on angular scales well below a degree.

The statistical significance of these multipole correlations is between $2 - 3\sigma$ compared to an isotropic sky, with the error dominated by cosmic variance. The maximum signal appears at scales $l \leq 70$, as seen previously by PLK13. We also find an unusually low scatter in the dipole component estimates as a function of scale, given the cosmic variance of an unmodulated Gaussian random field, suggesting that the microwave temperature sky may have additional correlations not captured by this simple model.

On the largest scales of the universe, simple models of inflation predict that the amplitude of any dipole modulation due to random perturbations in a statistically isotropic universe should be substantially smaller than that observed. This departure from statistical isotropy may require new physics in the early universe. One possible mechanism is a long-wavelength mode of an additional field that couples to the field generating perturbations [72, 73, 74, 75, 76, 77, 78, 79, 80, 81, 82, 83, 84, 85, 86, 87, 88, 89, 90, 91, 92, 93, 94, 95, 96, 97, 98, 99, 100]. If the mode has a wavelength longer than the current Hubble length, an observer sees its effect as a gradient. The field gradient modulates background physical quantities such as the effective inflaton potential or its slow-roll velocity. The required coupling between long- and short-wavelength modes can be accomplished in the context of squeezed-state non-Gaussianity [92, 93, 94, 95]. This mechanism requires a nontrivial scale-dependent non-Gaussianity.

Apart from the hypothesis of new physics, foreground contamination and instrumental systematics can break the statistical isotropy of the microwave background temperature map. However, these possibilities can be tested with the available data. Our estimates of the Cartesian components of the dipole vector, as functions of angular scale, are consistent for different foreground-cleaned temperature maps. The masking adopted in this analysis removes most contaminations from diffuse galactic emission and point sources, and our

analysis procedure controls possible biases introduced by this procedure. In addition, realistic instrument simulations provided by the Planck collaboration exclude instrumental effects as the source of the observed isotropy breaking at the angular scales of interest. While this work was in preparation, the Planck team has made available the results of a similar analysis using the 2015 temperature maps [6] (PLK15). Our estimates of the amplitude and direction of the dipole modulation vector on large scales ($l_{max} = 60$) are consistent with PLK15 analysis based on Bipolar Spherical Harmonics. The PLK15 analysis does not provide a constraint on the scale dependency, although it shows (as for the PLK13 analysis) that the amplitude must decrease at higher multipoles. PLK15 shows that the amplitude of the dipole vector differs from the isotropic case at a level of $2 - 3\sigma$ when calculated in cumulative multipole bins $[2, l_{max}]$ for $l_{max}$ up to 320. This result can be compared with our geometrical test in Fig. 15, for which similar results are found.

Additional tests of the dipole modulation will be possible with high-sensitivity polarization maps covering significant portions of the sky (see, e.g., Refs. [101, 43]). In the standard inflationary cosmology, microwave polarization and temperature are expected to be only partially correlated, giving an additional independent probe of a dipole modulation; a cosmic-variance limited polarization map will likely double the statistical significance of the signal studied here. Gravitational lensing of the microwave background over large sky regions provides another nearly independent probe which will be realized in the near future. We will consider these possibilities elsewhere. If these probes substantially increase the statistical significance of the dipolar modulation signal, we will be forced into some significant modification to the inferred physics of the early universe.
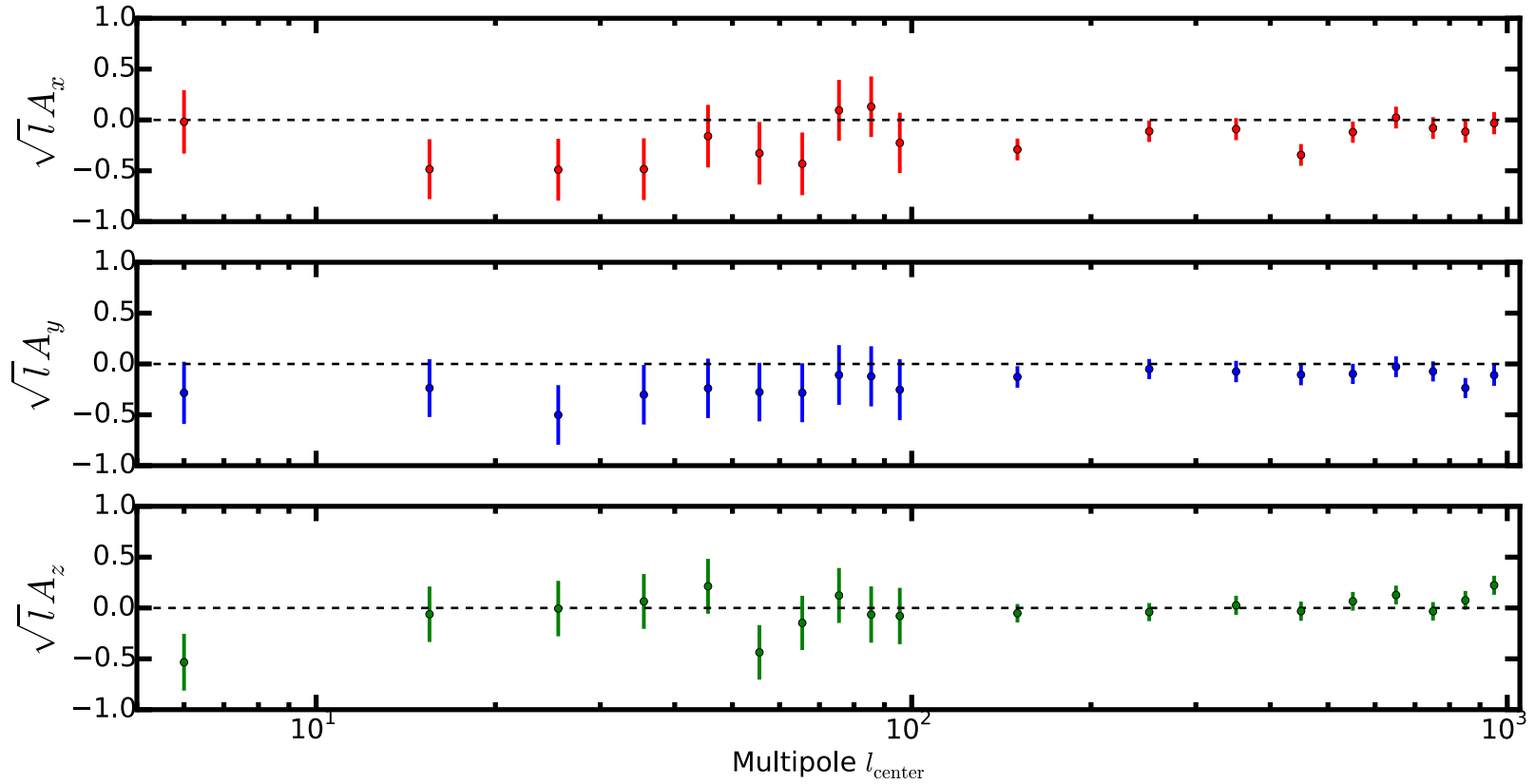
Figure 13: Measured Cartesian components of the dipole vector from the SMICA Planck map as a function of the central bin multipole $l_{\text{center}}$. The amplitudes are multiplied by $\sqrt{l}$ to enhance visibility of the signal at higher multipoles. The $1\sigma$ errors are the square roots of the covariance matrix diagonal elements. Data at $l > 600$ are not used in our statistical analyses.
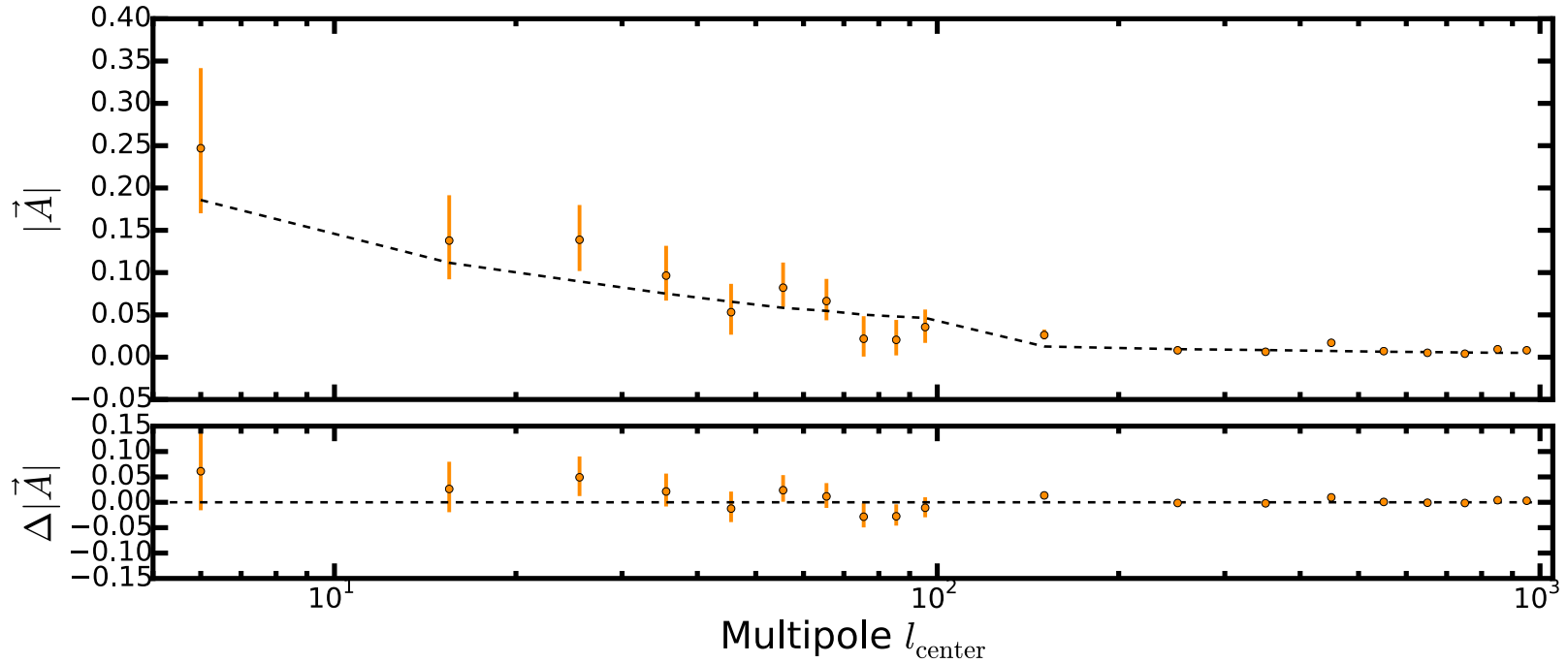
Figure 14: Measured amplitude of the dipole vector from the SMICA Planck map. The black dashed line shows the model for the statistical isotropic case **A**=0. The $1\sigma$ errors are estimated from the $16^{th}$ and $84^{th}$ percentiles of the distribution of the dipole vector amplitudes, calculated from sky simulations processed the same way as the data.
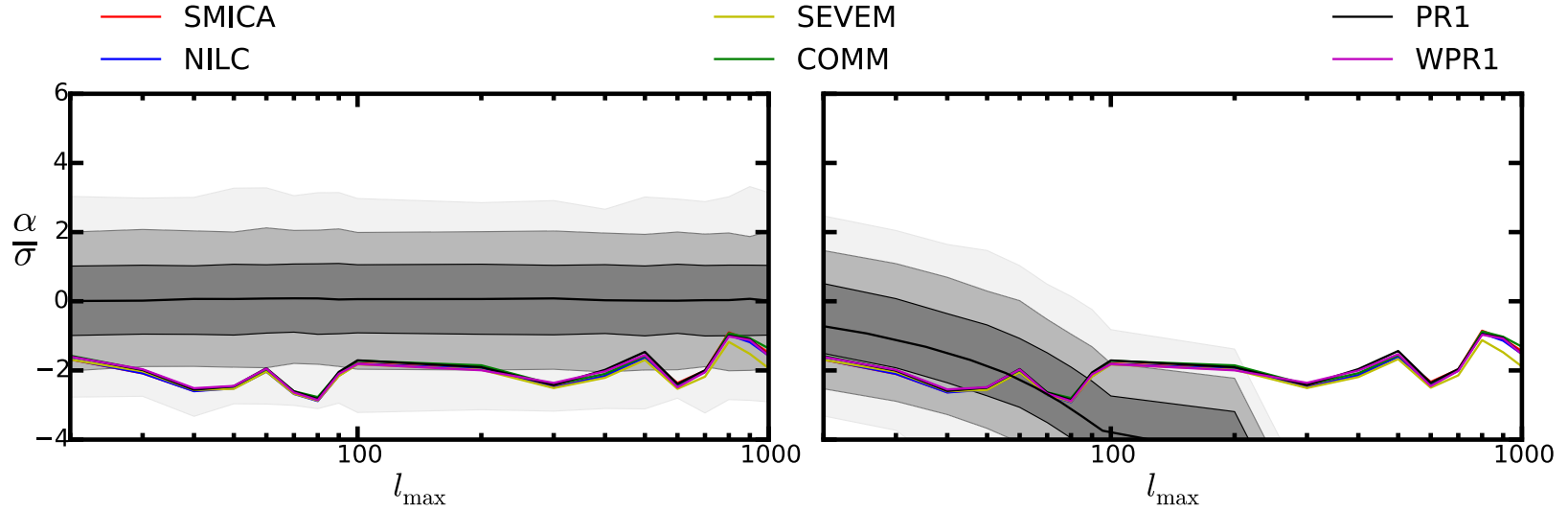
Figure 15: The $\alpha$−parameter from Eq. (IV.23), scaled by the standard deviation $\sigma(\alpha)$, as a function of the maximum multipole considered $l_{\max}$. The colored solid lines are the results from CMB data, showing remarkable consistency between different foreground cleaning methods. (Left panel) The shaded bands are estimated using simulations of isotropic masked skies. The distribution $\alpha$−parameter is Gaussian with $\langle\alpha\rangle = 0$. (Right panel) The shaded bands are estimated using simulations of dipole modulated masked skies. The dipole modulation model is $A = 0.07$, $(\ell, b) = (220°, -20°)$. The confidence regions (colored band) are estimated using percentiles, such that $\pm 1\sigma = [15.87^{th}, 84.13^{th}]$, $\pm 2\sigma = [2.28^{nd}, 97.72^{th}]$ and $\pm 3\sigma = [0.13^{st}, 99.87^{th}]$.

Table 3: Best-fit values of the amplitude $A$, spectral index $n$ and direction angles $(\ell, b)$ for the dipole vector, as a function of the maximum multipole $l_{\max}$. The best-fit values correspond to the $50^{th}$ percentile of the posterior distribution marginalized over the other parameters. The errors correspond to the $16^{th}$ and $84^{th}$ percentiles. For the first case, we consider a model with spectral index $n = 0$ and $l_{\max} = 60$, which can be compared with PLK13 findings. Values of the $\chi^2$ corresponding to the best-fit model, as well as to the isotropic case, are also displayed with a corresponding number of degrees of freedom $\nu$.

| $l_{\max}$ | $A$ | $n$ | $b[°]$ | $\ell[°]$ | $\chi^2_{\min}(\nu)$ | $\chi^2_{A=0}(\nu)$ |
|---|---|---|---|---|---|---|
| 60 | $0.063^{+0.028}_{-0.030}$ | $-$ | $-10^{+21}_{-21}$ | $+218^{+24}_{-24}$ | 10.3 (15) | 19.5 (18) |
| 200 | $0.034^{+0.014}_{-0.016}$ | $-0.54^{+0.38}_{-0.22}$ | $-7^{+16}_{-16}$ | $+211^{+19}_{-19}$ | 16.4 (29) | 30.8 (33) |
| 300 | $0.029^{+0.012}_{-0.014}$ | $-0.68^{+0.26}_{-0.19}$ | $-11^{+18}_{-16}$ | $+211^{+20}_{-20}$ | 18.1 (32) | 31.4 (36) |
| 400 | $0.027^{+0.012}_{-0.014}$ | $-0.74^{+0.22}_{-0.18}$ | $-9^{+19}_{-18}$ | $+212^{+22}_{-21}$ | 19.3 (35) | 31.9 (39) |
| 500 | $0.031^{+0.012}_{-0.013}$ | $-0.61^{+0.23}_{-0.15}$ | $-4^{+13}_{-13}$ | $+207^{+16}_{-16}$ | 22.5 (38) | 40.2 (42) |
| 600 | $0.031^{+0.011}_{-0.012}$ | $-0.64^{+0.19}_{-0.14}$ | $-1^{+13}_{-14}$ | $+209^{+16}_{-15}$ | 23.9 (41) | 41.9 (45) |

# V. GAUSSIAN APPROXIMATION OF PEAK VALUES IN THE INTEGRATED SACHS-WOLFE EFFECT

The content of this chapter was published in February 2015 in the Physics Review D journal and produced by the collaborative work of Bingjie Wang, Arthur Kosowsky, and myself [102]. ©2015 American Physical Society.

## A. INTRODUCTION

The current state of accelerated expansion of the universe has been well established through a combination of the type-Ia supernova Hubble diagram [2, 1], primary and lensing-induced anisotropies in the cosmic microwave background (CMB) [16, 103, 32], and measurements of baryon acoustic oscillations [104]. Such an expansion, believed to be driven by dark energy, leaves an imprint in the large-scale cosmic structure (at redshifts in a range of $z \leq 2$), as well as on the CMB temperature fluctuations. Gravitational potentials evolve in time due to the accelerating expansion, giving a net change in energy to photons traversing an underdense or overdense region. This effect, known as the *late-time Integrated Sachs-Wolfe effect* (late-ISW) [105], is described by the following integral along the line-of-sight:

$$\Theta(\hat{\mathbf{n}}) \equiv \frac{\Delta T}{T_0} = -2 \int_0^{\chi^\star} d\chi g(\tau) \dot{\Phi}(\chi \hat{\mathbf{n}}, \eta_0 - \chi) \tag{V.1}$$

where $g(\tau) = e^{-\tau(\eta_0 - \chi)}$ is the visibility function as a function of the optical depth $\tau$, the derivative of the Newtonian gravitational potential $\Phi$ is with respect to the conformal time, $\eta_0$ is the present value of the conformal time, $\chi^\star$ is the comoving distance to the surface of last scattering, and $T_0$ is the isotropic CMB blackbody temperature, corresponding to the

multipole $\ell = 0$. The late-ISW effect creates temperature anisotropies mostly on relatively large angular scales ($\theta > 3°$). A detection of this signal in a spatially flat universe represents an independent test for dark energy [106], and in principle a useful tool to characterize its properties and dynamics [107].

In ΛCDM cosmological models, this secondary CMB anisotropy contributes only around 3% of the total variance of the temperature sky, while having a Gaussian random distribution to a very good approximation, and hence it cannot be detected from temperature data alone. Nevertheless, it is strongly correlated with the large-scale galaxy distribution [108], and recently the angular cross-power spectrum $C_\ell^{Tg}$ between CMB temperature and galaxies has been exploited to detect the late-ISW signal [109, 110, 111, 112, 113, 114, 115, 116, 117, 118, 119, 120, 121, 122, 123] (see Table 1 of [124] for a detailed list of related works). A similar correlation was detected in pixel space, corresponding to the presence of hot and cold spots in the CMB sky preferentially centered on superstructures ([125], GNS08 hereafter). This strong detection exploited a novel technique involving photometric analysis of stacked CMB patches from the WMAP 5-year sky maps [126] centered on 100 superstructures (50 biggest superclusters and 50 biggest supervoids) detected in the Sloan Digital Sky Survey (SDSS) Data Release 6 [127], covering a sky area of 7500 square degrees in a redshift range $0.4 < z < 0.75$. In this redshift range, the expected cross-correlation spectrum peaks at $\ell \simeq 20$ ($\theta \simeq 4°$) ([128], HMS13 hereafter), which motivated the use of a compensated top-hat filter of 4° radius to enhance the signal [129]. The mean temperature fluctuation reported by GNS08 of $\overline{T} = 9.6$ $\mu$K shows a departure from the null signal at a significance of $4.4\sigma$. Recently, the Planck satellite collaboration has confirmed the detection of the late-ISW effect with a statistical significance ranging from $2.5\sigma$ to $4.0\sigma$ (depending on the method involved) ([120], PLK13 hereafter). The strongest Planck detection is associated with the stacking analysis, using the GNS08 catalog, giving an average peak amplitude of $\overline{T} = 8.7\mu K$, which is consistent with the value found by GNS08 using the WMAP temperature map.

As pointed out by [123], the temperature-galaxy cross correlation requires prior knowledge of the galaxy bias, which may dominate the detection significance and consistency tests of the underlying cosmological model. In contrast, the technique of stacking on the largest superstructures in a large-scale structure survey does not rely on any knowledge regarding

the galaxy bias, apart from the fact that visible matter traces dark matter. In addition, the GNS08 technique is based on an extreme-value statistic: in principle, it is sensitive to small departures from the $\Lambda$CDM model which may not significantly affect the cross-correlation $C_\ell^{Tg}$. On the other hand, substantial control over systematic errors is required to carry out such an analysis.

It has been argued that the strong signal detected by GNS08 is in tension with the underlying $\Lambda$CDM model [130, 131]. Analytical estimates of the stacked late-ISW signal in a comoving volume that corresponds to that probed by GNS08 predict an average signal of $\overline{T} = 2.27 \pm 0.14 \mu K$ ([131], FHN13 hereafter), where the reported error is due to cosmic variance. The same work confirms this estimate using late-ISW maps constructed from N-body simulations which include the second-order Rees-Sciama contribution [132]. The discrepancy with the GNS08 measurement has a significance greater than $3\sigma$. Other cosmological models have been considered to explain the discrepancy, including primordial non-Gaussianities [128] and $f(R)$ gravity theories [133], but neither seems adequate to explain the strong detected signal.

A less interesting but more plausible possibility is that the strong detected signal is the result of correlations of the late ISW signal with other sources of temperature anisotropy, which may boost the mean temperature of the identified top-ranked peaks. The current theoretical predictions of the stacked late-ISW signal do not include correlations between ISW temperature fluctuations formed at different redshifts. In HMS13, the primary temperature fluctuations, formed at redshift $z \simeq 1100$, were considered uncorrelated with the secondary anisotropies and simply added to Gaussian random generated late-ISW maps. These high-redshift fluctuations are partially correlated with the secondary temperature anisotropies, at a level that depends on the underlying cosmological model. More importantly, we expect a non-negligible correlation between the late-ISW signal, traced by superstructures in GNS08 in the redshift range $0.4 < z < 0.75$, and the late-ISW effect due to structures at either higher or lower redshift.

In this work, we provide a complete description of these correlations through simulated skies based on simple linear perturbation theory. Temperature fluctuations on large scales result from gravitational potential perturbations in the linear regime (see [134] for alterna-

tive proposal). If the primordial perturbations are a Gaussian random field, which appears to be an excellent approximation to the observed large-scale structure [135], the statistical properties of the CMB sky on large angular scales are completely specified by the temperature power spectrum $C_\ell^{TT}$. We generate Gaussian random realizations of the CMB sky using the linear power spectra for its various physical components, including correlations between them. This is an easy computational process, in contrast to extracting large-angle late-ISW maps from large-box N-body cosmological simulations [136, 137]. The approach we adopt in this work allows full characterization of the cosmic variance with a random sample of simulated skies, and it automatically accounts for the effects of the largest-scale perturbation modes beyond the reach of N-body simulations. We then reanalyze foreground-cleaned CMB temperature maps, processed to match the procedure adopted in our sky simulations. This last step guarantees that the discrepancy between theoretical estimates and the measured signal is not due to different analysis procedures. Our simulated late-ISW mean peak temperature signal is consistent with previous estimates, but with a wider spread of values. Correlations between temperature signals increase the expected mean value as well as the spread slightly. The main reason for this larger spread, however, is the noise associated to the uncorrelated fluctuations at scales of our interest, and thus reduces the statistical significance of the discrepancy between theory and experiment to around $2.5\sigma$ when compared with our measured values from CMB maps.

This chapter is organized as follows: in Section V.B, we describe an algorithm to generate realistic temperature maps, including spatial filtering and all correlations between temperature components. We then present the pipeline of our simulations in Section V.C, and the resulting distribution of late-ISW mean peak temperatures. In Section V.D, we apply the same procedure to the Planck CMB temperature maps. Finally, Section V.E concludes with a discussion of possible sources of systematic errors, a comparison with other late-ISW detection techniques, and future prospects for resolving the discrepancy between theory and measurements with wider and deeper large-scale structure surveys.

## B.   CORRELATED COMPONENTS OF THE TEMPERATURE SKY

The $\Lambda$CDM model is a compelling theory to describe the statistical properties of the CMB fluctuations, making precise predictions for the temperature power spectrum $C_\ell^{TT}$ [138, 139]. Different physical processes contribute to the temperature fluctuations over a wide range of angular scales; the CMB temperature sky is well approximated by the sum of correlated Gaussian random fields, one for each physical component, such that

$$
\begin{aligned}
\langle a_{\ell m}^i, a_{\ell' m'}^{i\star} \rangle &= \delta_{\ell\ell'} \delta_{mm'} C_\ell^{ii} \\
\langle a_{\ell m}^i, a_{\ell' m'}^{j\star} \rangle &= \delta_{\ell\ell'} \delta_{mm'} C_\ell^{ij}
\end{aligned}
\tag{V.2}
$$

where $i$ and $j$ are the components making up the observed temperature field $\Theta(\hat{\mathbf{n}}) = \sum_i \sum_{\ell m} a_{\ell m}^i Y_{\ell m}$ and the power spectra satisfy the condition $C_\ell^{ii} C_\ell^{jj} \geq \left( C_\ell^{ij} \right)^2$ [30]. This set of power spectra specify the covariance matrix of the temperature given a cosmological model. For the purposes of this work, we consider a 2-component sky described by a symmetric 2x2 covariance matrix. The first component, $C_\ell^{1,1}$, is always the late-ISW component of the temperature field, corresponding to the GNS08 redshift range (ISW–in, hereafter). For the second component, $C_\ell^{2,2}$, we consider two distinct cases:

- **Case A**: *only* late-ISW generated outside the probed redshift range, corresponding to $0 < z < 0.4$ and $0.75 < z < 10$ (ISW–out, hereafter);
- **Case B**: primary and secondary anisotropies generated outside the probed redshift range. Specifically, we consider the sum of ISW–out, early ISW after recombination, and Sachs-Wolfe, intrinsic and Doppler contributions at last scattering.

The off-diagonal terms $C_\ell^{1,2}$ are calculated according to the specific case we consider. For a spatially flat, $\Lambda$CDM cosmological model with the best-fit Planck+WP+HighL parameters [32] we compute the covariance matrix in Eq. (V.2) with the numerical Boltzmann code `CLASS v2.2`[1] [7], including the nonlinear effects calculated with `Halofit` [140]. The

---

[1]http://class-code.net/
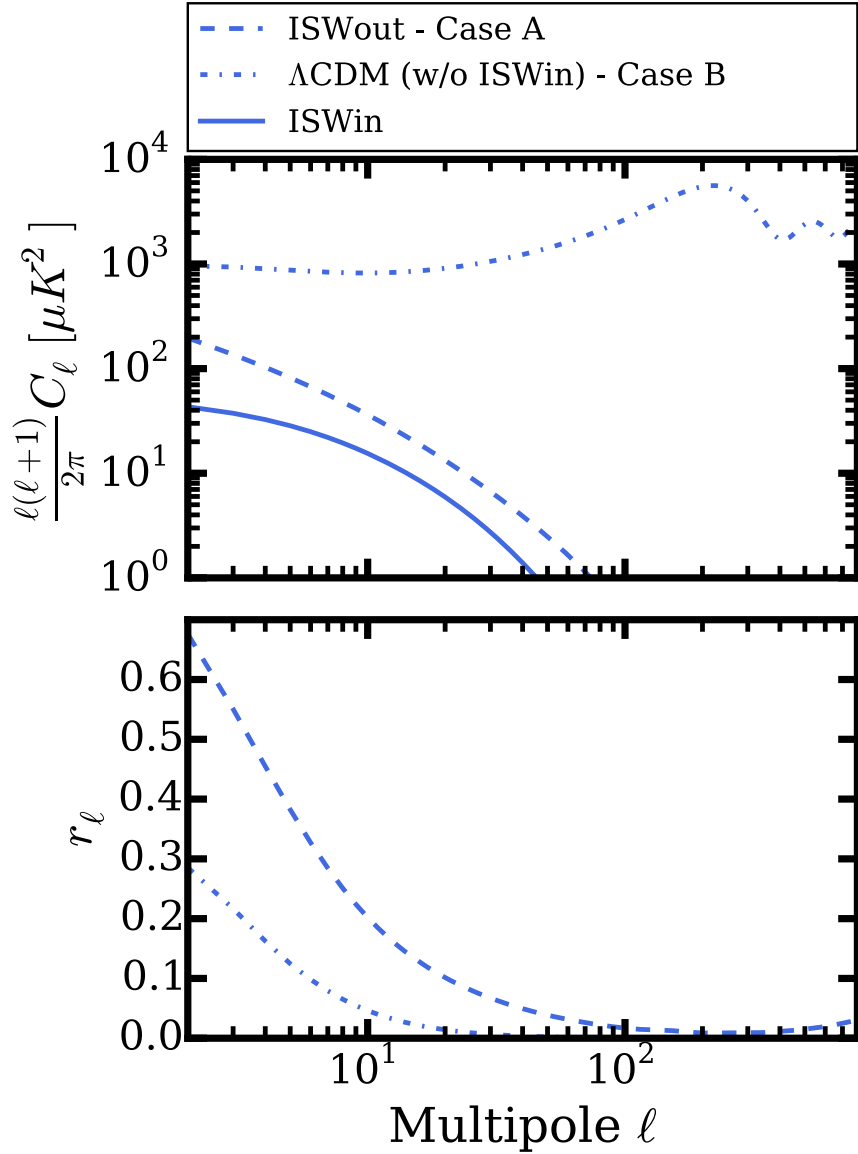
Figure 16: Top: Angular power spectra in ΛCDM, for the ISW effect due to structure in the redshift range $0.4 < z < 0.75$ ("ISW–in", green), ISW effect outside of this redshift range ("ISW–out", blue), and all temperature perturbation components except for ISW–in (yellow). Bottom: Correlation coefficients between ISW–in and ISW–out (blue), and between ISW–in and all other temperature perturbation components (yellow).

correlated harmonic coefficients are generated via Cholesky decomposition as

$$a_{\ell m}^i = \sum_{k=1}^{2} A_{\ell,ik}\zeta_k$$

$$a_{\ell m}^T = a_{\ell m}^1 + a_{\ell m}^2$$

(V.3)

where $\zeta_k$ is a column vector composed of 2 complex Gaussian random numbers with zero mean and unit variance, and $A_\ell$ is a lower-diagonal real matrix which satisfies $C_\ell = A_\ell^T A_\ell$. The $a_{\ell m}^1$ are the harmonic coefficients corresponding to the ISW–in component alone.

In Fig. 16, we plot the unfiltered covariance matrix components as function of the multipole $\ell$. The top panel shows the diagonal terms. Note that the signal of interest, ISW–in, has a lower amplitude compared than the other components at all multipoles. Thus, the statistics of temperature peaks for an unfiltered map are completely dominated by the anisotropies generated at last scattering. A wise choice for an $\ell$-space filter is required (see below, Sec. V.C). The bottom panel shows the off-diagonal terms; we plot the normalized correlation coefficient

$$r_\ell \equiv \frac{C_\ell^{ij}}{\sqrt{C_\ell^{ii}C_\ell^{jj}}}$$

(V.4)

which satisfies the condition $|r_\ell| \leq 1$. The correlation matrix cannot be considered diagonal, especially at low $\ell$ values. In principle we expect a negative cross-correlation on large scales (i.e. $r_\ell < 0$) due to the Sachs-Wolfe component: if we consider the entire late-ISW contribution (i.e., $0 < z < 10$), the cross-spectrum is dominated by the ISW-SW term, which gives an overall anticorrelation. In the case of interest (where we consider shells of late-ISW signal), the dominant part is the correlation between ISW–in and ISW–out. Notice that $r_\ell^{\text{CaseA}}/r_\ell^{\text{CaseB}} \simeq \sqrt{C_\ell^{2,2(\text{CaseB})}/C_\ell^{2,2(\text{CaseA})}}$, which implies that the mean value of the stacked signal is mainly enhanced by the ISW–out component. This peculiar effect is attributed to the wide range of $k-$modes, which couples the fluctuations of neighboring redshift regions. On the other hand, the mildly correlated primary fluctuations dominate the statistical error in averaged peak values. Analytical signal and error estimates are possible but not simple [141], so we compute both numerically in the following Section.

## C. METHODOLOGY AND ANALYSIS

The multipole region of our interest is dominated by cosmic variance. This problem is difficult to characterize using N-body simulations, so we generate random temperature maps from the power spectra and correlations to construct the statistical distribution of ISW mean peak amplitudes. The procedure described in this section is based on the FHN13 analysis, adapted to multicomponent correlated sky maps.

### 1. Harmonic-Space Filtering

To isolate the late-ISW peak signal in $\ell$-space, we apply the $4°$ compensated top-hat filter adopted by GNS08:

$$F(\theta) = \begin{cases} (2\pi(1 - \cos\theta_F))^{-1}, & 0 < \theta < \theta_F, \\ -(2\pi(\cos\theta_F - \cos\sqrt{2}\theta_F))^{-1}, & \theta_F < \theta < \sqrt{2}\theta_F, \end{cases} \tag{V.5}$$

where $\theta_F = 4°$ is the characteristic filter radius. By performing a Legendre transform of the real-space filter $F(\theta) \to F_\ell = \int F(\theta)\mathcal{P}_\ell(\cos\theta)d\cos\theta$, we can compute a full-sky filtered map simply by rescaling the covariance matrix, $C_\ell \to C_\ell F_\ell^2 B_\ell^2$, which also uses an additional Gaussian beam smoothing $B_\ell$ with `FWHM`$= 30'$ adopted by PLK13 to match the WMAP resolution. The compensated top-hat filter does not give a sharp cutoff in multipole space. However, it drops off faster than $\ell^{-2}$, which ensures the suppression of the small-scale fluctuations. At the scales enhanced by the filter $\ell \simeq 10 - 30$, the portion of the temperature fluctuations uncorrelated with the ISW–in signal for Case B is approximately one order of magnitude larger than that for Case A, with a resulting increase in the scatter of the mean peak statistic.

### 2. Simulation Pipeline

To identify the peaks of the late-ISW temperature fluctuations in the CMB sky map, GNS08 used the distribution of luminous red galaxies in `SDSS DR6` and looked for overdense and underdense regions. The top-ranked 100 superstructures identified in the sample have a

median radial length calculated at $z = 0.5$ of $R_v \simeq 85 Mpc$ and $R_c \simeq 25 Mpc$ for voids and clusters respectively. The corresponding normalized fluctuations of the gravitational potential are of the order $\Phi \simeq 10^{-4}$ [129]. These gravitational potential fluctuations are still in the linear regime for standard structure growth.

Assuming perfect efficiency in detecting and ranking superstructures from large-scale structure distribution data, the observed GNS08 signal should match the theoretical expectation from averaging the CMB temperature fluctuations traced by the 100 biggest fluctuations in the filtered late-ISW map over the redshift range of the survey [131]. We generate correlated pairs of filtered random Gaussian maps, one for the ISW–in component and one for the other linear components of the temperature sky, using multipoles in both power spectrum $\ell \leq 800$; we use HEALPix[2] [65] with NSIDE=256. From the filtered ISW–in map, we identify the 50 hottest maxima and 50 coldest minima in a sky region of area $f_{\mathrm{sky}} = 0.2$, corresponding to the sky fraction of the SDSS DR6 survey. Maxima and minima are identified pixel-by-pixel, testing whether or not the temperature of the central pixels is the greatest or the smallest of the 8 surrounding pixels. Finally, we take the pixels corresponding to these extrema and average their values in the full sky map consisting of the sum of the two correlated random maps. We find the average of the 50 hottest ISW–in maxima $\overline{T_h}$ and 50 coldest ISW–in minima $\overline{T_c}$ separately, and we also compute the combined mean value as $\overline{T_m} = (\overline{T_h} - \overline{T_c})/2$. For comparison, we also calculate the same quantities for the ISW–in map only, which we call **Case 0**. This procedure is performed on an ensemble of 5000 random generated skies.

The procedure adopted here gives an upper bound on the theoretical signal from clusters and voids identified in any specific tracer of large-scale structure: we simply assume that the 50 largest voids and 50 largest clusters in a sky region are correctly identified. Any error in identifying these features will lead to a smaller mean signal. Since the measured signal is larger than the expected theoretical maximum signal, errors in cluster identification will increase the difference between theory and measurement quantified in the next section.

---

[2] http://healpix.sf.net

Figure 17: The mean value of the filtered CMB temperature at the locations of the top 50 cold spots $\overline{T_{\mathrm{cold}}}$ and top 50 hot spots $\overline{T_{\mathrm{hot}}}$ of the ISW–in map component, corresponding to the late-ISW signal from structures in the redshift range $0.4 < z < 0.75$, for a sky fraction $f_{sky} = 0.2$. Plotted are $(\overline{T_{\mathrm{hot}}}, \overline{T_{\mathrm{cold}}})$ for 5000 randomly generated skies with all contributions to the CMB signal (green points). The red cross is at the location of the mean values of $\overline{T_{\mathrm{cold}}}$ and $\overline{T_{\mathrm{hot}}}$ for the 5000 model skies. For comparison, we plot 5000 model skies generated using only the ISW–in signal (gray points), and 5000 skies generated using the full late late-ISW signal but no other temperature components (blue points). Also displayed are the measured values from GNS08 (purple diamond) and from the analysis in Sec. IV using Planck data (black square).

Table 4: Results from Gaussian random skies, stacked on peaks of the ISW–in signal (the ISW generated for structure in the redshift range $0.4 < z < 0.75$). The simulated skies are constructed from the angular power spectra in the standard $\Lambda$CDM cosmology, smoothed with a Gaussian beam of FWHM 30' and a compensated top hat filter of radius $4°$, Eq. (V.5). We report the mean and the standard deviation of the stacks on the locations of the 50 hottest ISW–in spots $\overline{T_h}$, 50 coldest ISW–in spots $\overline{T_c}$, and the mean magnitude for all 100 spots $\overline{T_m}$, calculated from 5000 random realizations of the microwave sky, including correlations between the ISW–in signal and other sky components. These values are presented for ISW–in skies only (Case 0), ISW–in plus ISW–out skies (Case A), and realistic skies including early ISW, intrinsic, and Doppler contributions to the sky temperature (Case B). The theoretical prediction from FHN13 and the measured value from GNS08 are reported for comparison.

| Case | $\overline{T_h}\ [\mu K]$ | $\overline{T_c}\ [\mu K]$ | $\overline{T_m}\ [\mu K]$ |
|---|---|---|---|
| **Case 0** | $1.97 \pm 0.09$ | $-1.97 \pm 0.09$ | $1.97 \pm 0.07$ |
| **Case A** | $2.23 \pm 0.25$ | $-2.23 \pm 0.25$ | $2.23 \pm 0.20$ |
| **Case B** | $2.30 \pm 3.1$ | $-2.30 \pm 3.1$ | $2.30 \pm 2.32$ |
| **FHN13** | - | - | $2.27 \pm 0.14$ |
| **GNS08** | $7.9 \pm 3.1$ | $-11.3 \pm 3.1$ | $9.6 \pm 2.22$ |

## 3. Results and Comparison with Previous Work

The results of our simulations are presented in Table 4 and visually summarized in Fig. 17 and Fig. 18. As expected for random realizations of a Gaussian field, $|\overline{T_h}| = |\overline{T_c}|$. The mean peak signal for the full simulated sky maps (Case B) is $2.30 \pm 2.32\ \mu$K, compared to the GNS08 measurement of 9.6 $\mu$K, a discrepancy at a significance of $3.1\sigma$. Our discrepancy is about the same size as previous analyses, but the significance is somewhat lower. This is due to our inclusion of all components in the microwave temperature map and their correlations, which increases the uncertainty in our predicted values. The central value of our ISW–in peak signal, 1.97 $\mu$K (Case 0), is lower by 0.30 $\mu$K than the signal predicted in FHN13, which
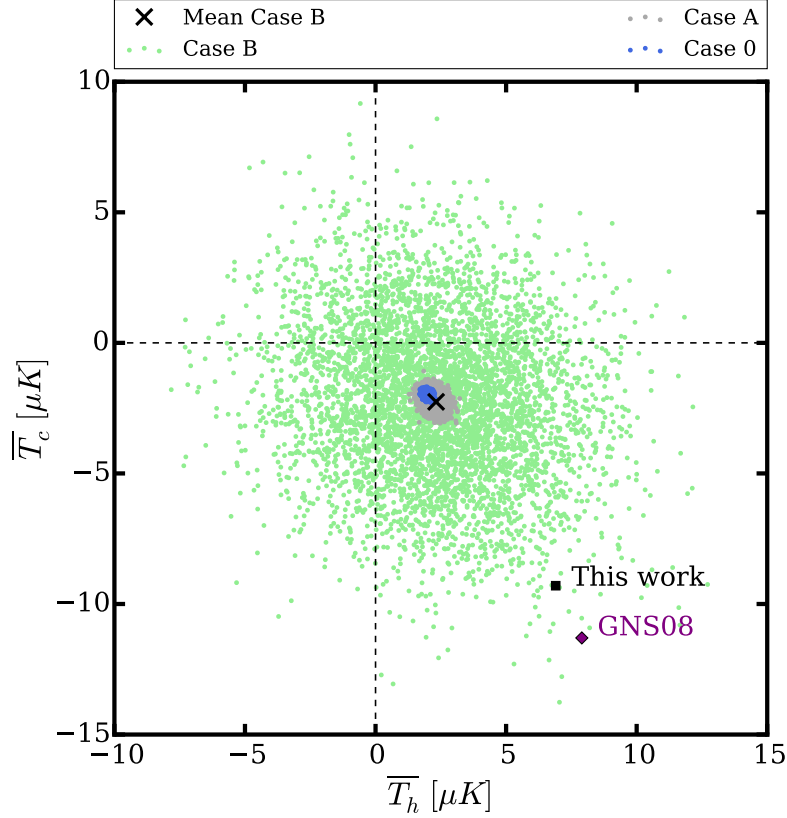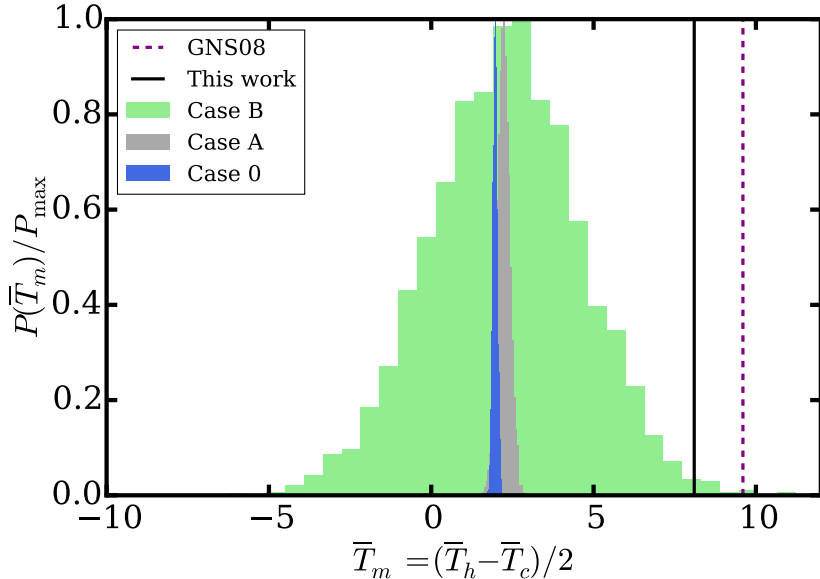
Figure 18: The combined mean value of the filtered CMB temperature at the locations of the top 50 cold spots and top 50 hot spots of the ISW–in map component, corresponding to the late-ISW signal from structures in the redshift range $0.4 < z < 0.75$, for a sky fraction $f_{sky} = 0.2$. Plotted are the distributions (normalized to the maximum value) of the combined mean temperature $(\overline{T}_{\mathrm{hot}} - \overline{T}_{\mathrm{cold}})/2$ obtained from 5000 simulated skies, for the three difference cases considered in this work. Also displayed are the measured values from GNS08 (purple vertical line) and from the analysis in Sec. IV using Planck data (black vertical line).

is expected due to a difference in the underlying cosmological models used. However, the difference is small compared to the statistical uncertainty for the full sky signal (Case B). The central value of our full-sky peak signal is also higher than the ISW–in peak signal by 0.33 $\mu$K; this difference is due to the correlations between the ISW–in signal and the other components which are included in the Case B peak signal.

70

## D.  THE STACKED ISW SIGNAL USING PLANCK SKY MAPS

The original late-ISW peak analysis in GNS08 used WMAP sky maps, and PLK13 confirmed the measured value using Planck data. Here we obtain the measured late-ISW signal from publicly available foreground-cleaned maps based on Planck and Planck+WMAP data, using the same sky locations as GNS08. The purpose of this re-analysis is testing the significance of the discrepancy by using the same analysis pipeline as the simulations in Sec. V.C, to ensure that the difference between the model and the measured value is not due to any inconsistency in how the data and simulations are treated.

We use four different foreground-cleaned CMB temperature maps, based on different component separation approaches. Two are public CMB temperature maps from the `Planck` collaboration[3], namely `SMICA` and `NILC`[66]. The other two maps are based on the `LGMCA` method[4] from the recent work in Ref. [67]. The `PR1` map uses only `Planck DR1` data [42], and the `WPR1` map uses both `Planck DR1` and `WMAP9` data [138].

We process these four maps in the same fashion:

- we apply a Gaussian beam smoothing in harmonic space to the map defined as $B_\ell = B_\ell(30')/B_\ell(\mathrm{map})$ where $B_\ell(\mathrm{map})$ is the effective beam of the released map; this allows us to take into account for the finite resolution of the instrument, and hence matching the overall smoothing applied to the simulated maps. We also filter out the small-scale fluctuations by setting the harmonic coefficients of the map $a_{\ell m} = 0$ for $\ell > 800$;

- the preprocessed map is then masked using the released `Planck` mask `U73`, avoiding contaminations from bright point sources;

- the masked map is filtered in harmonic space using the compensated top-hat filter $F_\ell$ and repixelized to `NSIDE=256`;

- we read the temperature values of the pixels corresponding to the cluster/void positions used in GNS08 [5].

Fig. 20 shows the filtered `SMICA` map in a Mollweide projection in ecliptic coordinates;

---
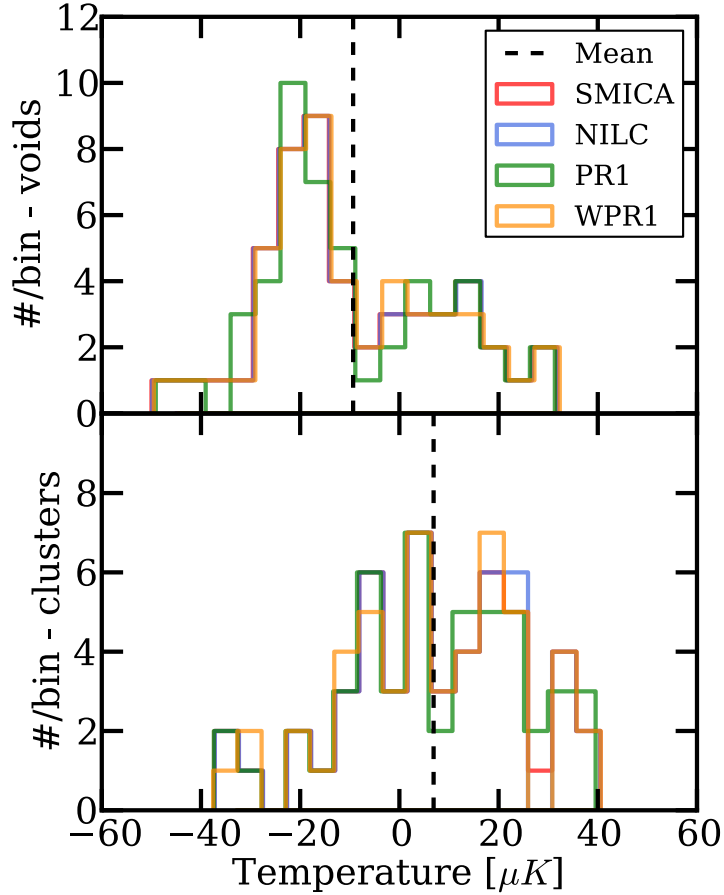
Figure 19: Histograms of pixel temperatures centered on superstructures identified by GNS08, measured using 4 different foreground-cleaned filtered CMB maps. Top panel: measured temperatures at locations of voids in the GNS08 catalog; the dashed vertical line indicates the mean temperature. Bottom panel: the same for locations of clusters.

superstructure locations from GNS08 are marked. In Fig. 19, we plot the histogram of the temperature values for voids and clusters separately for the four analyzed maps. The measured values are used to calculate the quantities $\overline{T_c}$, $\overline{T_h}$ and $\overline{T_m}$ given in Table 5. Different component separation methods quantify the effects of residual foreground contamination. We measure the fluctuations of the average temperature signal for different maps and use the variance of these fluctuations $\sigma_{\mathrm{FG}}$ as an estimate of the error due to foregrounds. The

temperature values are extremely stable and fluctuations are always within 1% (see also Fig. 19), suggesting that the temperature variations are predominantly cosmological. Our mean peak temperature values are smaller than those reported by GNS08 and PLK13 by around 1.5 $\mu$K, which is within the $1\sigma$ uncertainty. Such a difference is driven mainly by details of the filtering procedure. The results of our simulations and our measured signals, shown in Fig. 17 and Fig. 18, can be summarized as

- The departure of the measurements from a null signal has decreased somewhat compared to previous analyses. It corresponds to a detection significance of $2.2\sigma$, $3.0\sigma$ and $3.5\sigma$ for clusters, voids and combined, respectively;
- The measurements are higher than the expected maximum signal in $\Lambda$CDM cosmology at a level of $1.5\sigma$, $2.3\sigma$ and $2.5\sigma$ for clusters, voids and combined, respectively;
- The asymmetry between the measured signal for voids and clusters is not statistically significant, being smaller than $1\sigma$.

For these estimates, we consider foregrounds contamination and cosmic variance from simulations to be uncorrelated; hence we take $\sigma_{\text{tot}} = \sqrt{\sigma_{\text{FG}}^2 + \sigma_{\text{sim}}^2}$, but the residual foreground error is small compared to the cosmic variance uncertainty.


## E.   DISCUSSION


Our analysis confirms both the size of the stacked late-ISW signal seen by GNS08 and PLK13, and theoretical predictions for $\Lambda$CDM models by FHN13 and HMS13. By using several maps with different foreground subtraction methods, we demonstrate that foreground residuals contribute negligible uncertainty to the measured signal. The theoretical modeling, using correlated Gaussian random fields, is far simpler than previous analyses using N-body simulations, showing that the predicted signal has no significant systematic error arising from insufficient box size or other subtleties of the simulations. Our calculations also include the correlations between the late-ISW signal and other sources of microwave temperature

Table 5: Mean temperature deviations for GNS08 cluster and void locations, for four temperature maps with different foreground cleaning procedures. We estimate the mean and standard deviation $\sigma_{FG}$ from the four different maps.

| Map | $\overline{T_h}$ $[\mu K]$ | $\overline{T_c}$ $[\mu K]$ | $\overline{T_m}$ $[\mu K]$ |
|---|---|---|---|
| NILC | 6.9 | −9.4 | 8.1 |
| SMICA | 7.0 | −9.4 | 8.2 |
| PR1 | 6.9 | −9.3 | 8.1 |
| WPR1 | 6.9 | −9.2 | 8.0 |
| MEAN | 6.89 | −9.33 | 8.11 |
| $\sigma_{FG}$ | 0.01 | 0.09 | 0.04 |

anisotropies, which mildly increases the theoretical mean signal while also increasing the statistical uncertainty. We find a stacked late-ISW signal which is different from null at $3.5\sigma$ significance, and a discrepancy between the predicted and observed signal of $2.5\sigma$ in Planck sky maps at the peak and void locations determined by GNS08 from SDSS data in the redshift range $0.4 < z < 0.75$.

The statistic used in this work is the mean value at the sky locations of the 50 highest positive and lowest negative peaks in the late-ISW signal, assumed to be traced by structures and voids in a large-scale structure survey. In simulations, the late-ISW peaks can be identified directly, and the 50 highest peaks in a given sky region are known precisely. When analyzing large-scale structure data, peak identification will not be perfectly efficient: some of the actual 50 largest extrema in the late-ISW signal may be missed in favor of others which have lower amplitude. Thus the observed signal will necessarily be biased low. The observed discrepancy between observation and theory has the observed signal high compared to the prediction, so any systematic error in cluster identification has reduced this discrepancy. In other words, our observed discrepancy is a lower limit to the actual discrepancy, which may be larger than $2.5\sigma$ due to the identified clusters and voids being imperfect tracers of the

late-ISW temperature distribution. In reality, the total late-ISW signal is the superposition of signals from very large numbers of voids and clusters, and it is not clear the extent to which the largest voids and clusters individually produce local peaks in the filtered late-ISW map. Since our predicted maximum signal is consistent with that from N-body simulations, it seems likely that large structures do actually produce local peaks in the filtered late-ISW map. In the limit that the void and cluster locations from GNS08 do not correlate at all with peaks in the late-ISW distribution, the model signal will be zero; but then the mean signal at the GNS08 locations is $3.5\sigma$ away from the expected null signal.

The uncertainty in the difference between the observed signal and the theoretical maximum signal is dominated by the primary temperature anisotropies which are uncorrelated with the late-ISW signal. When stacking at late-ISW peak locations, these primary fluctuations average to zero, with a Poisson error. This uncertainty can be reduced only by including more peak locations in the average. The current analysis uses late-ISW tracers from around 20% of the sky, in a specific redshift range. Using the same analysis with a half-sky survey at the same cluster and void threshold level will increase the number of voids and cluster locations by a factor of 2, reducing the Poisson error by a factor of $\sqrt{2}$ and potentially increasing the detection significance of an underlying signal discrepancy from $2.5\sigma$ to $3.5\sigma$. Extending the redshift range to lower $z$, where the late-ISW effect is stronger for a given structure in standard $\Lambda$CDM models, can further increase the census of clusters and voids, potentially pushing the discrepancy to greater than $4\sigma$. However, complications at lower redshifts arise due to differing angular sizes of voids on the sky. A stacking analysis at locations of lower-redshift SDSS voids has seen no signal clearly different from null [142], suggesting that the discrepancy here and in GNS08 may be due to noise. Upcoming optical surveys like Skymapper [143] and LSST [144] promise a substantial expansion in the census of voids and clusters suitable for late-ISW peak analysis.

If the discrepancy is confirmed with increased statistical significance by future data, this would suggest that the late-ISW peak signal is larger than in the standard $\Lambda$CDM model. Since the clusters and voids considered are on very large scales, they are in the linear perturbation regime, and the physics determining their late-ISW signal is simple, so it is unlikely that the theoretical signal in $\Lambda$CDM is being computed incorrectly. While the association

of voids or clusters with peaks in the late-ISW distribution is challenging, any inefficiency in this process will only increase the discrepancy between theory and measurement. The remaining possibility would be that the assumed expansion history in $\Lambda$CDM is incorrect, and that the discrepancy indicates expansion dynamics different from that in models with a cosmological constant. Any such modification must change the peak statistics of the late-ISW temperature component while remaining within the bounds on the total temperature power spectrum at large scales, and must be consistent with measurements of the cross correlation between galaxies and microwave temperature. Given the limited number of observational handles on the dark energy phenomenon, further work to understand the mean peak late-ISW signal in current data, and its measurement with future larger galaxy surveys, is of pressing interest.
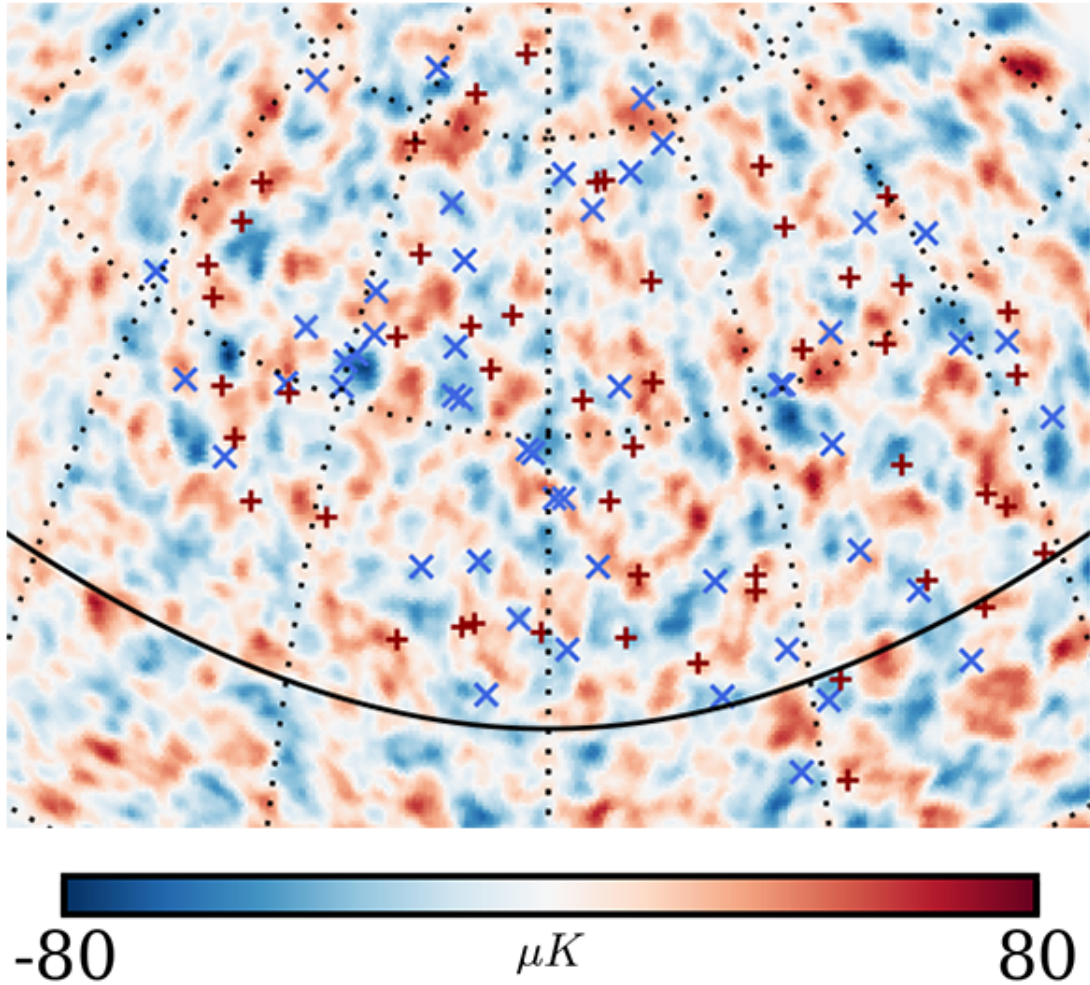
Figure 20: The filtered SMICA-Planck CMB temperature map, in a Mollweide projection in ecliptic coordinates. The galactic region and point sources have been masked with the U73-Planck mask. The resolution of the HEALPIX maps is NSIDE= 256. The locations of superclusters (red "+") and supervoids (blue "x") from the GNS08 catalog are also shown.

# VI. MAXIMUM LIKELIHOOD MAP MAKING FOR THE ATACAMA COSMOLOGY TELESCOPE

In this chapter I describe the current status of the maximum-likelihood map-making pipeline of the Atacama Cosmology Telescope (ACTpol) team. I am currently responsible for the characterization and improvement of the pipeline, which was initially developed by Jonathan Sievers for the ACT/MBAC experiment [145] and upgraded for the analysis of the ACTpol polarization data [146]. My short-term goal is to deliver CMB temperature and polarization maps based on the 2013 and 2014 seasons of data. Such maps will constitute the starting point for several scientific analyses, such as CMB lensing, cluster cosmology, and cosmological parameter estimation. The current priority is understanding the tensions between Planck, WMAP, and SPT temperature data [147]. In addition, I study the ability of the current pipeline to recover the long-wavelength modes (i.e. large angular scale fluctuations) possibly limited by filtering procedures, aiming to develop a framework that would be optimized for the measurement of the large-scale B-mode signal. As the pipeline is not yet finalized, I present only preliminary results based on the current status of the analysis.

## A. CURRENT PICTURE IN EXPERIMENTAL CMB COSMOLOGY

Different millimeter telescopes have observed or are observing the CMB sky both in temperature and polarization. Space-based observatories, such as the WMAP and the Planck satellites, are capable of mapping the full-sky over a wide range of frequencies. However, strict engineering specifications on space-mission payloads limit the telescope resolution ($\theta_{\mathrm{high-res}} < 5'$ at 150 GHz), thus restricting the target to large-scale and mid-scale modes. As

far as constraining the vanilla $\Lambda$CDM model with temperature data is concerned, the 2015 data release of the Planck satellite shows that cosmic-variance limited measurements up to $\ell \approx 2500$ provide the tightest constraints, and no extra information is added when including higher multipoles measured by high-resolution ground-based experiments [8]. However, high resolution is required to measure interesting phenomena, such as the thermal and kinetic Sunyaev-Zel'dovich effects, which probe gravity and baryonic physics at a low redshift.

In polarization, Planck sensitivity does not provide a sample-limited measurement of the E- and B-mode power spectra. Ground-based experiments are now taking the next step toward mapping of the polarized sky at high signal-to-noise. CMB polarization provides an (almost) independent measurement of the physics at recombination, with a constraining power on cosmological parameters (in the cosmic-variance limited regime) higher by roughly a factor of three than temperature-only data [148].

The increasing sensitivity of CMB experiments makes the control of systematics an important, as well as, complicated task. A combined study of Planck, WMAP and South Pole Telescope temperature data reveals inconsistencies between the different datasets [147]. Planck temperature data in the multipole range between $1000 < \ell < 2500$ shows $2.5\sigma$ to $3\sigma$ tensions with low redshift probes and with the Planck temperature data for $\ell < 1000$. On large and intermediate scales (i.e. $\ell < 1000$), WMAP and Planck provide consistent results. To probe the small-scale regime that is not measured by WMAP, the authors of [147] use SPT temperature data, finding agreement with both WMAP and Planck on $\ell < 1000$. This reinforces the tension between the small-scale fluctuations mapped by Planck and the other datasets. The authors suggest that the discrepancy could indicate that residual systematic effects are still present in the Planck data. However, a statistical fluke and new physics cannot be excluded based on the current available data. The upcoming two-season ACTpol analysis will contribute to this comparison by giving parameter constraints based on a 700 deg$^2$ patch of the sky centered on the equator. Such constraints will be complementary to the ones released by the SPT collaboration, which are based on the analysis of a CMB patch located in the southern hemisphere.

## B.   THE ATACAMA COSMOLOGY TELESCOPE

The Atacama Cosmology Telescope (ACTpol) is a millimeter polarimeter located in the Atacama Desert at 5190 m above sea level, where the atmosphere is highly transparent to microwave radiation. The reflective optics of the telescope follows a Gregorian off-diagonal design with a 6-meter primary mirror and a 2-meter secondary, which focuses the incoming radiation onto a cryogenic microwave camera. The camera features, after full deployment in 2015, three arrays of 3068 superconductive Transition Edge Sensors sensitive to polarization. The first two arrays, installed in 2013 and 2014, are sensitive to radiation at 148 GHz. The third array consists of dichroic detectors simultaneously sensitive to 97 and 148 GHz radiation, constituting the first attempt of using such a new technology on a CMB experiment. The three arrays are kept at the superconductive transition temperature of about 100 mK by a dilution refrigerator that continuously runs to ensure 24-hour long observations of the sky [149].

The telescope superstructure can move in azimuth and elevation, and it is surrounded by a 13-meter tall ground screen to reduce the pickup of thermal emission from the ground and surrounding structures. The scan strategy consists of periodic scans along the azimuthal direction at constant elevation. Different elevations allow us to target different regions of the sky, whereas the width of the azimuth scan and the drift of the sky above the telescope define the area of the observed region. In equatorial coordinates, this corresponds to slightly tilted periodic scans in declination (DEC), which drift along the Right Ascension (RA). The same patch is observed both in rising and setting to guarantee cross-linking between different scanning patterns. Observations are conducted by remote observers within the collaboration, who supervise the status of the observations, manage failures, and coordinate maintenance with the local team.

### 1.   Observations

During the 2013 observational season, ACTpol targeted four deep 70 deg$^2$-wide regions along the equator. This strategy enabled the first signal-dominated measurement of the CMB E-

mode polarization over the range between $\ell = 200 - 9000$, based on only three months of nighttime observations. The measured E-mode power is consistent with the expectations from the best-fit $\Lambda$CDM cosmology, derived from previous CMB temperature data [146]. In 2014, ACTpol pursued the nighttime and daytime observations of two of the previously observed fields, called D5 and D6, and three wide fields. For the current analysis of 2013+2014 data, we restrict the dataset to only nighttime observations. Indeed, more investigation is required to characterize the time-variability of the beams due to mirror deformations during the day. Specifically, the dataset of interest corresponds to the D5 and D6 deep patches and the wider D56 region, which covers 700 deg$^2$ along the equator overlapping D5 and D6 [150].

## C.   NINKASI: A MAXIMUM-LIKELIHOOD MAP-MAKING PIPELINE

The data is divided into 10-minute long (considered to be) independent unities, called time-ordered data (TOD), which contain the signal from each detector, the pointing of the telescope, and housekeeping information, as function of time. The sampling rate from the detectors is 400Hz, implying that each TODs has order of $n_{\mathrm{samp}} = 10^8$ data samples for roughly $n_{\mathrm{det}} = 10^3$ detectors. Such raw data needs to be processed and projected onto high-fidelity CMB sky maps for science analyses.

   Consider a pixelated sky map $\vec{m}$, where each entry of the vector represents a 0.5 arcmin$^2$ pixel[1]. At a given time $t$, the telescope points to a pixel $p(\hat{n})$ in the sky, therefore we can create a binary pointing matrix $\mathbf{A} = A_{p,t}$ with value 1 indicating which pixel (or pixels for a multi-detector instrument) is observed at time $t$. In order to develop a mathematical formalism for the map-making pipeline, we need to assume a model for our data, which can be written as:

$$\vec{d_t} = \mathbf{A}\vec{m_p} + \vec{n_t}, \tag{VI.1}$$

where $\vec{d_t}$ ($n_{\mathrm{det}} \times n_{\mathrm{samp}}$) represents the TOD containing all the detectors and $\vec{n_t}$ ($n_{\mathrm{det}} \times n_{\mathrm{samp}}$) is a realization of Gaussian noise in time domain, described by the $(n_{\mathrm{det}} \times n_{\mathrm{samp}}) \times (n_{\mathrm{det}} \times n_{\mathrm{samp}})$

---

[1]The map resolution (i.e. pixel's size) is chosen to have roughly 4 samples within the beam solid angle. For ACTpol the beam is 1.4$'$-wide at 150 GHz.

covariance matrix $\mathbf{N} = \langle n^T n \rangle$ [151]. For a CMB polarimeter, we aim to reconstruct not only the temperature map, $\vec{I}$, but also the polarization maps, $\vec{Q}$, and $\vec{U}$. For this reason the components of the vector $\vec{m}_p$ ($n_{\mathrm{pix}} \times 3$) can be simply written as $m_p = [I_p, Q_p, U_p]$ (see Section II.B.2 for a discussion on Stokes parameters). The projection in time domain of the three Stokes parameters, for a single detector, can be written as

$$\vec{d} = \mathbf{A}[\vec{I} + \vec{Q}\cos(2\gamma) + \vec{U}\sin(2\gamma)] + \vec{n} \qquad (\text{VI.2})$$

where $\gamma$ is the detector polarization angle expressed in a given sky coordinate system, and we dropped the subscripts $_t$ and $_p$. For the case of ACTpol, CMB maps are made in Equatorial coordinates, such that an orthonormal basis with axes $x$, $y$, and $z$ can be defined by: $\hat{x}$ being tangent to the great circle passing through the poles and the pixel of interest (i.e tangent to the Declination (DEC) meridian), $\hat{y}$ being tangent to the circle parallel to the equator passing through the pixel of interest (i.e. tangent to the Right Ascension (RA) parallel), and $\hat{z}$ being along the line-of-sight direction. In this geometry, a $Q$ map has structures aligned vertically and horizontally with the respect to the RA (or DEC) coordinates (see Fig. 22); whereas, a $U$ map has structures tilted by $\pm 45°$ (see Fig. 23).

In order to invert Eq. VI.2 and recover the Stokes parameters in each pixel, we can assume a simple Gaussian likelihood for the data, such that

$$\mathcal{L} = \exp -\frac{1}{2}\left((\vec{d} - \mathbf{A}\vec{m})^T \mathbf{N}^{-1}((\vec{d} - \mathbf{A}\vec{m})\right), \qquad (\text{VI.3})$$

where we have absorbed the $\cos(2\gamma)$ and $\sin(2\gamma)$ factors into the pointing matrix $\mathbf{A}$. The maximum-likelihood solution for the estimated map $\vec{\tilde{m}}$ leads to the following linear system

$$(\mathbf{A}\mathbf{N}^{-1}\mathbf{A}^T)\vec{\tilde{m}} = \mathbf{A}\mathbf{N}^{-1}\vec{d}, \qquad (\text{VI.4})$$

where $\vec{\tilde{m}}$ is unbiased (i.e. $\langle \vec{\tilde{m}} \rangle = \vec{m}$), and Gaussian distributed with covariance $\mathrm{Cov}(\vec{\tilde{m}}) = (\mathbf{A}\mathbf{N}^{-1}\mathbf{A}^T)^{-1}$. A formal solution to the linear system in Eq. VI.4 requires a brute force inversion of the covariance matrix on the left-hand side of the equation. This is not feasible even on a per-TOD basis, for which the pointing matrix has dimensions $(n_{\mathrm{pix}} \times 3) \times (n_{\mathrm{det}} \times n_{\mathrm{samp}})$ with $n_{\mathrm{pix}} = 10^6$, and the noise matrix $(n_{\mathrm{det}} \times n_{\mathrm{samp}}) \times (n_{\mathrm{det}} \times n_{\mathrm{samp}})$.

The linear system can be solved iteratively by means of Conjugate Gradient (CG) method [152]. If we consider the generic system $\mathbf{M}\vec{x} = \vec{b}$ to be solved via CG, the solution $\vec{x}$ needs to be decomposed onto a basis of conjugated vectors $\vec{p}_k$, such that $\vec{x} = \sum_k \alpha_k \vec{p}_k$. If such a basis is a-priori known, the solution consists only of estimating the coefficients $\alpha_k$, which are defined as $\alpha_k = \frac{\langle \vec{p}_k, \vec{b} \rangle}{\langle \vec{p}_k, \mathbf{M}\vec{p}_k \rangle}$. However, this is not the case for the sky map $\vec{m}$. From a more algebraic point of view, finding the solution $\vec{x}$ corresponds to minimizing the quadratic form $f(\vec{x}) = \frac{1}{2} x^T M x - b^T x$. The residual $\vec{r} = \vec{b} - \mathbf{M}\vec{x}$ gives $-\nabla f(\vec{x})$, which defines the direction we can move along to find the minimum of the quadratic form and used to suitably construct the basis for the PG method. If we define $\vec{x}_0$ to be some initial guess for the solution, we can construct the conjugated vectors and the residuals as

$$\vec{r_0} = \vec{b} - \mathbf{M}\vec{x}_0, \tag{VI.5}$$

$$\vec{p}_0 = \vec{r}_0. \tag{VI.6}$$

Now, we can compute the first coefficient $\alpha_0$, thus specifying the initial conditions of the CG solution. The general $k$-th conjugate vector $\vec{p}_k$ and associated coefficient $\alpha_k$, which are constructed at the $k$-th CG iteration, can be determined by Gram-Schmidt orthonormalization as

$$\vec{p}_k = \vec{r}_k - \sum_{i<k} \frac{\langle \vec{p}_i, \mathbf{M}\vec{r}_k \rangle}{\langle \vec{p}_i, \mathbf{M}\vec{p}_i \rangle} \vec{p}_i, \quad \alpha_k = \frac{\langle \vec{p}_k, \vec{b} \rangle}{\langle \vec{p}_k, \mathbf{M}\vec{p}_k \rangle} \tag{VI.7}$$

where $\vec{r}_k = \vec{b} - \sum_{i<k} a_i \vec{p}_i$. It is worth mentioning that the matrix $\mathbf{M} = (\mathbf{A}^T \mathbf{N}^{-1} \mathbf{A})$ can be seen as an operator and thus never constructed explicitly, where $\mathbf{A}$ projects the pixels values into time-ordered samples, $\mathbf{N}^{-1}$ performs inverse-variance weighting of the data, and $\mathbf{A}^T$ projects the data back onto a map. The number of required CG iterations strongly depends on the noise model (see Section VI.C.1) and on which maximum scale we aim to recover in the map. Fig. 21, 22, and 23 show I, Q, and U maps, respectively, of the D6 patch produced by following the procedure described above. Specifically, the top panel map of each figure is made by stopping the mapping process at 5 CG iterations, whereas the bottom panels reach 500 CG iterations. It is clear, even from a qualitative visual comparison, that large-scale modes require more CG iterations to be fully recovered in the map (i.e. to converge to the optimal solution).

### 1. Noise Model

One important element in Eq. VI.4 is the noise matrix $\mathbf{N}$, used to weight the data before projecting onto a map. In principle, the noise matrix can be substituted with a generic weight matrix $\mathbf{W}$, which must preserve the condition $\langle \vec{d} \rangle = \mathbf{A}\vec{m}$ to ensure an unbiased result [153]. However, only $\mathbf{W} = \mathbf{N}$ leads to the optimal maximum-likelihood solution. For the ideal case of perfectly uncorrelated detectors at the focal plane of a space-based telescope (i.e. considering only the detector white noise), the noise matrix can be modeled as diagonal, such that the noise realization $\vec{n}$ is independently drawn for each detector from a Gaussian distribution with zero mean and variance $\sigma_{\mathrm{det_i}}^2$.

Time-dependent thermal variations across the focal plane and, for the case of ground-based experiments, atmospheric emission correlate detectors leading to a non-diagonal noise matrix. Different sources of noise are described by characteristic spectral distributions and dominate the noise budget in specific frequency ranges, thus making the Fourier domain the ideal space to compute and apply the noise model. However, the lack of good atmospheric models and the imperfect knowledge of the instrument make a-priori modeling of the noise matrix a complicated task. For this reason, the noise model for the ACTpol experiment is computed in frequency space directly from the data $\vec{d}$ (as described below) [145]. The $(n_{\mathrm{det}} \times n_{\mathrm{det}})$ noise matrix is computed for each frequency bin, $\Delta f$ and consists of two distinct terms:

$$\mathbf{N_{\Delta f}} = \mathbf{V}\mathbf{\Lambda_{\Delta f}}\mathbf{V}^T + \mathbf{N}_{\mathrm{det},\Delta \mathrm{f}}. \tag{VI.8}$$

The first term, $(\mathbf{V}\mathbf{\Lambda_{\Delta f}}\mathbf{V}^T)$, describes the correlated noise modes across the array, whereas the second term, $\mathbf{N}_{\mathrm{det},\Delta \mathrm{f}}$, quantifies the uncorrelated detector noise thus constituting the diagonal part. The factorization of the noise matrix presented in Eq. VI.8 requires to (i) estimate the correlated noise modes and (ii) separate them from the uncorrelated component. This is achieved by constructing the high- and low-frequency $(n_{\mathrm{det}} \times n_{\mathrm{det}})$ detector-detector covariance matrices, $\Sigma$, from the band-limited Fourier transform of the time streams, such that $\Sigma_1 = \mathrm{FFT}(\vec{d}) \cdot \mathrm{FFT}(\vec{d})^T|_{0.25-4\mathrm{Hz}}$, $\Sigma_2 = \mathrm{FFT}(\vec{d}) \cdot \mathrm{FFT}(\vec{d})^T|_{4-1000\mathrm{Hz}}$. The choice of 4Hz as a transition frequency between high- and low-frequency regimes is dictated by the $1/f$-noise knee, which represents the boundary between the domination of atmospheric noise at

low frequency and domination of detector noise at high frequency. The estimated detector-detector correlations give us a way to model the first term on the noise matrix. Specifically, the columns of the matrix $\mathbf{V}$ are eigenvectors (or eigenmodes) of the covariance matrices $\Sigma_1$ and $\Sigma_2$, corresponding to the first few biggest eigenvalues. Geometrically, each eigenvector can be seen as a pattern across the array that correlates different detectors. In addition, the process of diagonalization defines an orthogonal basis that simplifies the estimation of the amplitudes of the correlated modes in each frequency bin. Such amplitudes are the elements of the $(n_{\text{det}} \times n_{\text{det}})$ diagonal matrix $\mathbf{\Lambda_{\Delta f}}$, and they are estimated as

$$\mathbf{\Lambda_{\Delta f}} = \frac{\langle|\text{FFT}(\vec{d})_{\Delta f} \cdot \mathbf{V}|^2\rangle}{N_{\text{samp}}}, \tag{VI.9}$$

where $\text{FFT}(\vec{d})_{\Delta f}$ is the Fourier transform of the data vector limited to the frequency samples in the bin $\Delta f$ and $\langle...\rangle$ represents an average over the frequency samples in the bin.

The second term of Eq. VI.8 is computed after removing the strong correlated modes from the data, thus leaving only a small correlation between detectors and allowing us to consider the $\mathbf{N}_{\text{det},\Delta f}$ to be diagonal. In detail, we compute the detector contribution to the noise matrix as:

$$\mathbf{N}_{\text{det},\Delta f} = \frac{\langle|\text{FFT}(\vec{d})_{\Delta f} - (\text{FFT}(\vec{d})_{\Delta f} \cdot \mathbf{V}^T)|^2\rangle}{N_{\text{samp}}}. \tag{VI.10}$$

The operation $\mathbf{N}^{-1}\vec{d}$ in Eq. VI.4 weights the data by inverse-noise weighting: large-scale modes are initially highly down-weighted because of the conspicuous amount of correlated noise. Visually this effect can be seen in the the top panels of Fig. 21, 22, and 23, which show maps that are high-pass filtered by the initial weighting. Therefore, large-scale modes converge slower than small-scale ones, requiring roughly 500 CG iterations to recover multipole scales up to $\ell \approx 200$.

Although the detector time streams in a TOD are noise dominated, the estimation of the noise model from signal+noise data can in principle bias our sky map. A possible solution to this problem consists of recomputing the noise model after subtracting the best estimate of the CMB signal from the data. To formalize this concept, let us consider the formal solution

$$\vec{m} = (\mathbf{A}\mathbf{N_d}^{-1}\mathbf{A}^T)^{-1}\mathbf{A}\mathbf{N_d}^{-1}\vec{d} \tag{VI.11}$$

where $\mathbf{N_d}$ indicates that the noise model has been computed from the vector $\vec{d}$. If we consider Eq. VI.11 to be the first, although biased, estimation of the CMB sky, we can iteratively converge to the true solution by

$$\vec{\tilde{m}}_{k+1} = \vec{\tilde{m}}_k + (\mathbf{A N_{d_k}}^{-1}\mathbf{A}^T)^{-1}\mathbf{A N_{d_k}}^{-1}\vec{d_k}, \qquad (VI.12)$$

where $\vec{d_k} = \vec{d} - \mathbf{A}\vec{\tilde{m}}_k$. Each $k$ step, called noise iteration, consists of a full mapping run (i.e. order of hundreds CG iterations to solve Eq.VI.4). For the current two-season analysis, we perform only 2 noise iterations, which are sufficient to reduce the noise bias to a level that is negligible compared to the statistical errors.

## 2. Data Filtering and the Transfer Function on Large Scales

The pipeline described above is completely developed in a maximum-likelihood framework, however it is commonly required to apply suitable filters to the data in order to remove or reduce spurious signals. A simple way to implement various type of filtering procedures is to consider $\vec{d} \rightarrow \mathbf{F}\vec{d}$, where $\mathbf{F}$ represents the filtering operator. This gives a biased solution for $\vec{\tilde{m}}$, however it does not require to estimate (if possible at all) $\mathbf{F}^T$. The ACTpol pipeline includes two of such filters to reduce scan-synchronous signal, called pre- and post-filter. It is reasonable to expect that thermal fluctuations of the optics, ground, or magnetic pickup can be modulated with the azimuth scan. For this reason a simple function $\mathbf{F} \rightarrow f(\mathrm{az}, t)$ of the azimuthal coordinate and time can be removed from the data before projecting onto a sky map via Eq. VI.4.

As no prior knowledge of this function can be assumed (unless we exactly know the nature of the scan-synchronous signal), we need to implement a parametric model, fit for the free parameters using the data $\vec{d}$, and then remove the estimated contribution from the data before mapping. For the specific case of ACTpol, we model the scan-synchronous signal as:

$$f(\mathrm{az}, t) = \sum_{\ell=0}^{8} \alpha_\ell P_\ell\big(cos(\mathrm{az})\big) + \sum_{k=0}^{10} \beta_k \Big(\frac{t}{t_0}\Big)^k, \qquad (VI.13)$$

where $P_\ell\big(cos(\mathrm{az})\big)$ are the Legendre polynomials, and $\alpha_\ell$ and $\beta_k$ are the coefficients determined as fit from the data. The pre- and post-filter are based on the same mathematical model but applied at different stages of the map-making pipeline:

- Pre-filter: the filter is applied during the data pre-processing phase, when we estimate the right-hand side of Eq. VI.4;

- Post-filter: the filter is applied after the map is made, and it consists of projecting the map into time streams, filtering the data as described above, and then projecting back onto the map.

For the case of the pre-filter, the fit of the free parameters is performed using noise-dominated data; whereas for the post-filter the time streams are generated from a signal-dominated map, thus increasing the efficiency of the filter. Although successful in reducing spurious contaminations, the filters introduce a transfer function $T_\ell$, such that the measured power spectrum from the map is $\tilde{C}_\ell = C_\ell T_\ell$. In other words, CMB modes may partially contribute to the fit and be removed during the subtraction of the function $f(\mathrm{az}, t)$ from the data. We expect the transfer function to be mostly dominated by the post-filter, because it is performed in the signal-dominated regime where the CMB has the biggest weight. Therefore, the characterization of the transfer function is fundamental to assess which multipoles are mostly affected by the filtering procedures and to apply specific cuts to avoid biases in the cosmological parameter constraints.

The characterization of the transfer function requires computationally-expensive simulations of the full pipeline. However as pointed out in Section VI.C.1, the noise matrix is constructed from the data itself, thus we do not have a model from which generate realistic simulations of TODs. One solution we adopted in the ACTpol pipeline consists of injecting a simulated sky into the TODs, meaning that the data vector becomes $\vec{d} \to \vec{d} + \mathbf{A}\vec{m}_{\mathrm{sim}}$. If we consider the operator $\mathcal{M}$ to represent the ACTpol map-making pipeline, and the operator $\mathcal{P}$ to be the power spectrum estimation pipeline, than the transfer function can be determined as

$$T_\ell = \frac{\mathcal{P}\left[\mathcal{M}[\vec{d} + \mathbf{A}\vec{m}_{\mathrm{sim}}] - \mathcal{M}[\vec{d}]\right]}{\mathcal{P}[\vec{m}_{\mathrm{sim}}]}. \tag{VI.14}$$

Currently, the transfer function is estimated to be $T_\ell \simeq 1$ for multipoles $\ell > 500$. On large scales, the power is suppressed at the $1\% - 5\%$ level for $\ell = 300$ with a weak dependency on the details of the scanning patter in each patch. The effect becomes more important as we look at scales greater than $1°$ in the sky, thus making this filtering procedure not suited

for large-scale E- and B-mode studies. A second element of concern is the possibility of a temperature-to-polarization leakage induced by the filters. Detailed investigation of this issue led to apply the post-filter separately for temperature and polarization, making the pipeline robust against leakage.

## D. CONCLUSIONS

The map-making and the data-processing pipelines for the analysis of the season 2013+2014 data (under development at the time that this work was presented) are similar to the ones developed for the one-year data analyses. However, the inclusion of wide patches, better understanding of the data, and improved characterization of the instrument have required extensive work in terms of (i) pipeline optimization and (ii) modeling and mitigation of systematic effects. This effort and lessons learnt can be summarized as follows:

- scanning strategies that are built on high-degree of cross-linking are naturally prone to the mitigation of systematics;
- the current version of the filtering procedure does not show a strong dependence on the details of the season 2013 (deep patches) versus season 2014 (wide patches) scan strategies. This allows us to easily interpret the large-scale power estimated from cross-correlation of the season 2013 and season 2014 overlapping data;
- the transfer function tends to zero on the largest scales in the sky. This finding will drive future work focused on recovering large-scale modes in ACTpol and Advanced ACT temperature and polarization maps.

Although the pipeline for the two-year data analysis is not finalized yet, science-quality maps are currently available and reliable on scales $\ell > 1000$, which are particularly suitable for cluster-science studies. Indeed, the CMB temperature maps from the combined 2013+2014 dataset have been used to detect the signal from the kinematic Sunyaev-Zel'dovich effect via cross-correlation with the large-scale structure velocity-reconstructed field [154] and with pair-wise statistics [155].

Figure 21: D6 temperature map at different Conjugate Gradient (CG) iterations. (Top panel) the mapping run is stopped at 5 CG iterations. The initial down-weighting of the noisy large-scale modes results in an effective high-pass filtering of the map. (Bottom panel) the mapping run is stopped at 500 CG iterations. In this case, large-scale modes have reached convergence at roughly 0.5° scale.
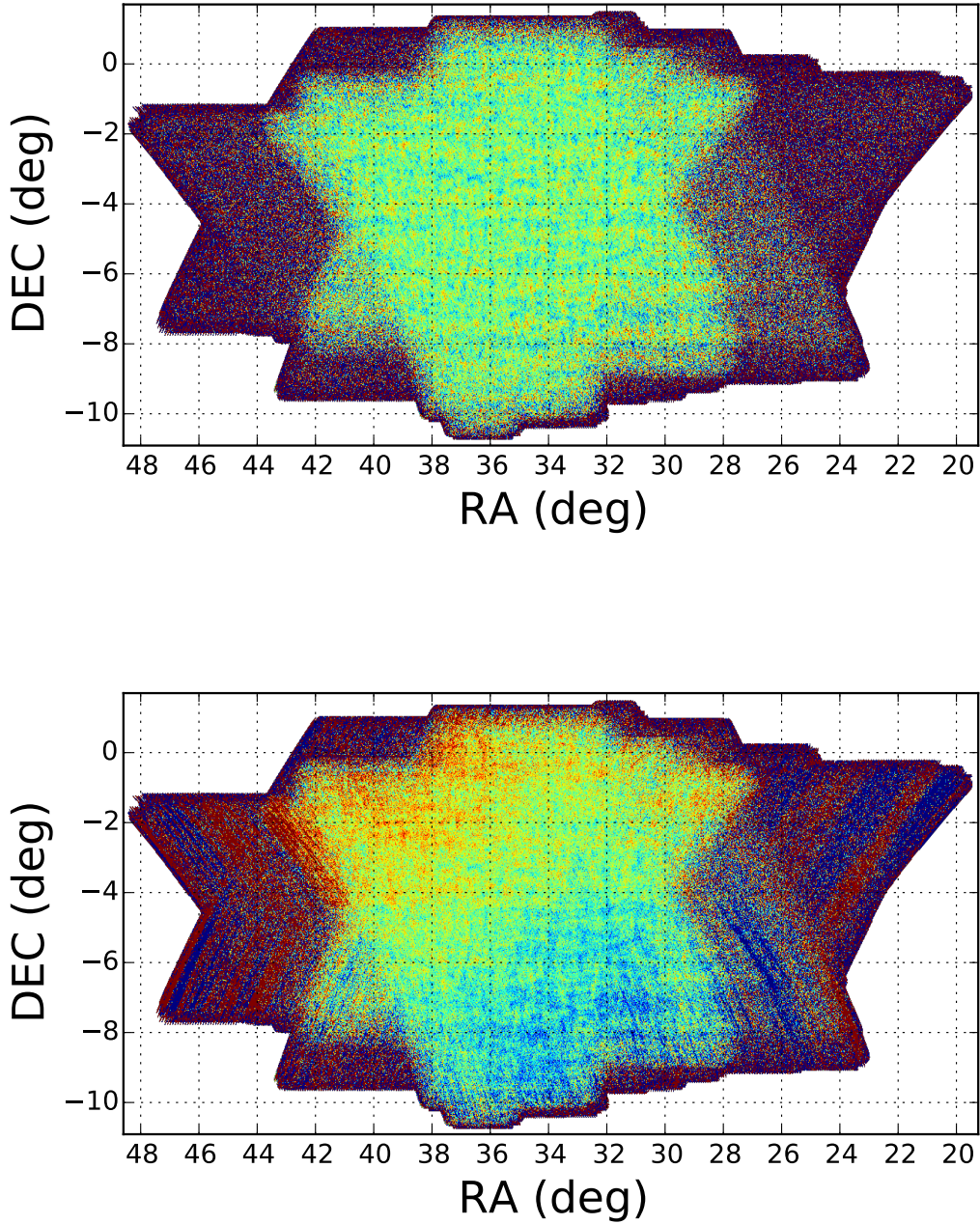
Figure 22: D6 polarization Q map at different Conjugate Gradient (CG) iterations. (Top panel) the mapping run is stopped at 5 CG iterations. The initial down-weighting of the noisy large-scale modes results in an effective high-pass filtering of the map. (Bottom panel) the mapping run is stopped at 500 CG iterations. In this case, large-scale modes have reached convergence at roughly 0.5° scale.
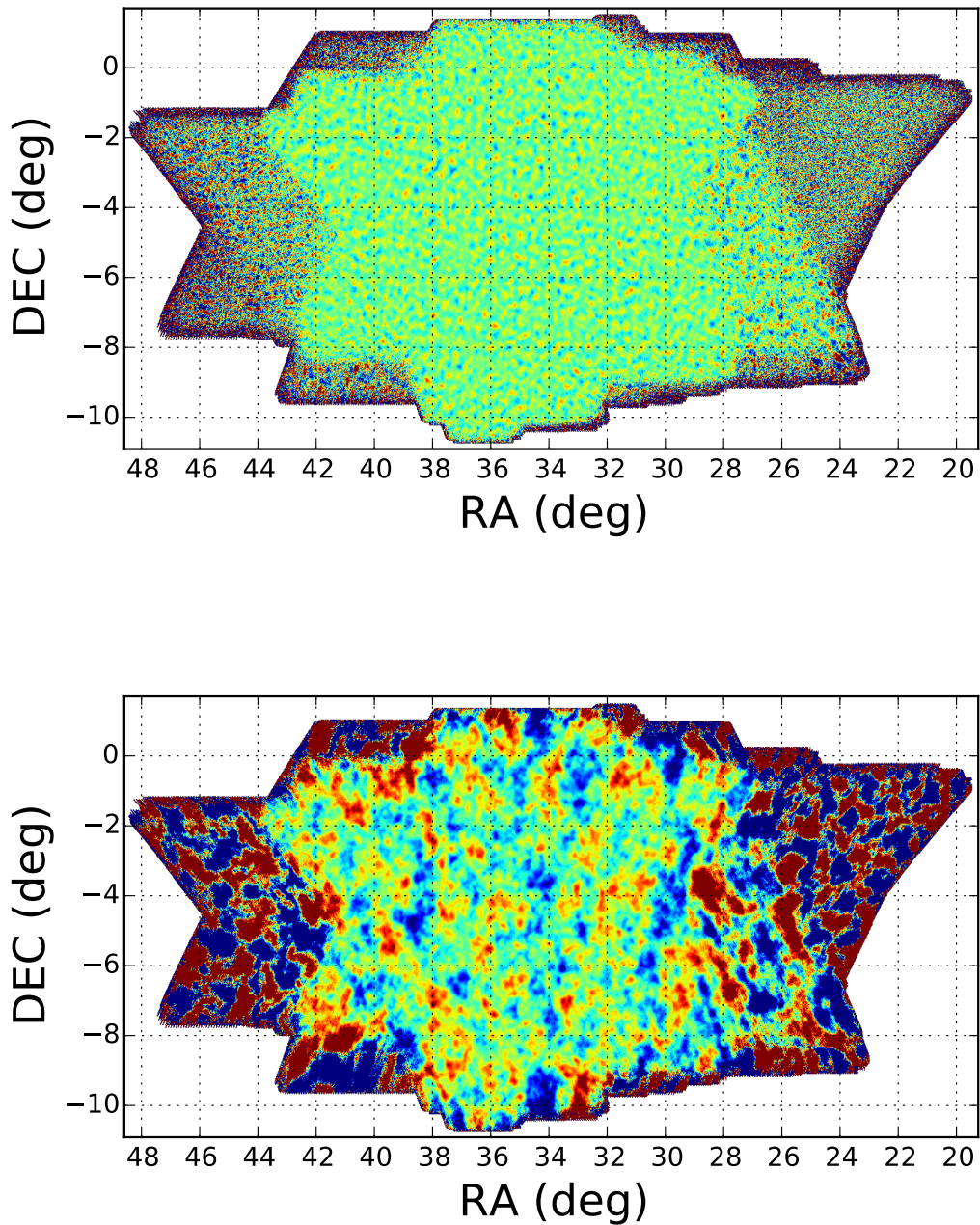
Figure 23: D6 polarization U map at different Conjugate Gradient (CG) iterations. (Top panel) the mapping run is stopped at 5 CG iterations. The initial down-weighting of the noisy large-scale modes results in an effective high-pass filtering of the map. (Bottom panel) the mapping run is stopped at 500 CG iterations. In this case, large-scale modes have reached convergence at roughly 0.5° scale.
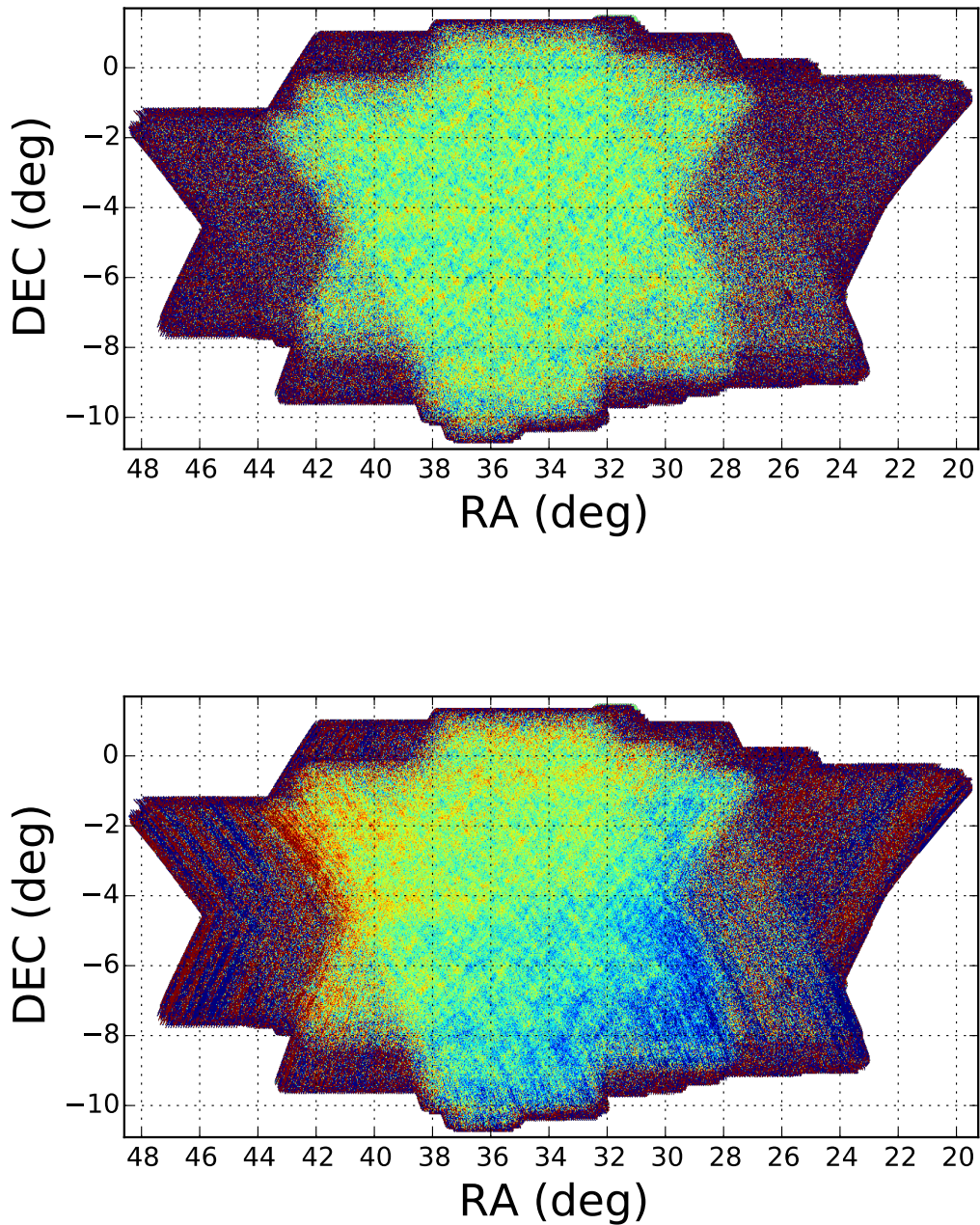
# VII. CONCLUSIONS

The possibility of explaining CMB anomalies as a statistical fluke has generated discordant opinions among the scientific community. Surely, we have all come to the conclusion that seeking a definite answer requires looking at the problem from a different point of view. The absence of large-scale correlations in the temperature sky is not expected from standard inflationary scenarios, and it is likely to happen by random chance less than 0.3% of the time in $\Lambda$CDM [4]. The CMB E-mode polarization pattern is expected to be only partially correlated ($< 50\%$) with the temperature fluctuations, and no correlation should be present with the B-mode pattern. This makes CMB polarization a valuable cosmological probe to understand if the temperature suppression is actually a suppression of the underlying density field. We presented analytical estimates for the polarization correlation functions for both $Q(\hat{n})$ and $U(\hat{n})$ Stokes parameters assuming the best-fit $\Lambda$CDM cosmology. In order to isolate the effects of the E- and B-mode polarization patterns, otherwise mixed in the Q/U maps, we also presented estimates for the local $\hat{E}(\hat{n})$ and $\hat{B}(\hat{n})$ polarization fields. The $S_{1/2}$ statistic has been applied for both solutions to Gaussian random realizations of the CMB polarization sky constrained by the observed temperature sky. We showed that this statistical measure gives similar results when applied to unconstrained realizations, highlighting that a possible detection of suppressed polarization correlations will highly exclude the hypothesis of a random fluke. By looking at the toy case of noise-only map on large scales, we pointed out that the currently proposed satellite experiments will be able to provide a compelling and possibly definite answer on this issue.

As argued in previous works, the suppression of the temperature correlation function requires a particular coupling between the low multipole moments rather than a simple suppression of first few $C_\ell$s [35]. A violation of the statistical isotropy is required for this

hypothesis to hold. Previous studies, which focused on the spatial distribution of the temperature power across the sky, showed that a dipolar power asymmetry is indeed present. In this context, we investigated the degree of statistical isotropy assuming a phenomenological dipolar modulation of the CMB temperature. This phenomenological model, which was initially proposed for a Dark Energy scenario with anisotropic stress-energy tensor, is supported by several multi-field inflationary theories. The investigation was carried out by constructing optimal estimators for the Cartesian components of the dipole vector (describing the amplitude and direction of the modulation) for different multipole ranges. We applied different statistical measures to assess the significance of the dipolar modulation, and we constrained its scale dependency via maximum-likelihood analysis. We concluded that the modulation is strongly scale dependent, and it is detected at a level between $2 - 3\ \sigma$. We finally tested our results against possible foreground contamination by using several foreground cleaned maps from the Planck team. We pointed out that future polarization measurements will help shade light on the problem.

The variety of models proposed to explain the dipolar modulation in the sky highlights that the large-scale temperature modes are particularly interesting, because they feature the direct contributions from both inflation and Dark Energy. Large-scale structure data can help isolate these two contributions, as the distribution of matter at low redshift is correlated with the ISW effect. The detection of the ISW signal, performed by stacking temperature maps centered on the location of superstructures in the universe, was found to be inconsistent with theoretical expectation from N-body simulations. We investigated whether or not such a discrepancy could be driven by missing modes in the N-body simulations due to limited box size. The analysis was carried out in the linear regime, hence we relied on the assumption that the large-scale sky is described by the CMB power spectrum. We estimated the maximum ISW signal expected from $\Lambda$CDM by following a similar procedure described in the original detection paper. We compared our estimates with a re-analysis of the CMB data from the Planck satellite to match the simulation pipeline. We found that a more accurate description of the CMB sky, along with matching the simulation and analysis pipelines, reduces lower bound of the discrepancy with $\Lambda$CDM from $3\sigma$ to $2.5\sigma$.

The results from the Planck collaboration have confirmed previously detected anomalies,

thus excluding the possibility of systematic-driven effects. In order to move forward with CMB polarization tests, ground-based experiments are now planning on targeting large portions of the sky. The ACT collaboration is transitioning to that regime as the newly-born Advanced ACT survey will soon have its first light. We presented the map-making pipeline of the ACTpol survey and the status of the current analysis, describing how the data will play a role in understanding the discrepancy between the WMAP, Planck, and SPT small-scale temperature data. In addition, we pointed out the challenges that the ground-based experiments have to face to increase the fidelity of the large-scale modes in the maps.

## 1. Future Prospects

The violation of the statistical isotropy is a promising path to understand how different anomalies are connected. If we assume that a primordial suppression in the correlation of the density perturbations is what we see in the CMB sky, then we need a framework to construct models of the universe that incorporate such a suppression. In harmonic space, this suppression requires the introduction of correlations between different Fourier modes, thus questioning the validity of the cosmological principle. With such a new framework, we will be able to make predictions on the correlation function and the statistical isotropy of different cosmological fields. Therefore, we will be able — for the first time — to compare $\Lambda$CDM with alternative models. In terms of cosmological probes, 21-cm surveys and high signal-to-noise CMB lensing maps will allow us to probe the 3D density field in the Hubble volume and to help disentangle primordial effects from low redshift ones.

# BIBLIOGRAPHY

[1]  S. Perlmutter et al. Measurements of Omega and Lambda from 42 high redshift supernovae. *Astrophys. J.*, 517:565–586, 1999.

[2]  Adam G. Riess et al. Observational evidence from supernovae for an accelerating universe and a cosmological constant. *Astron. J.*, 116:1009–1038, 1998.

[3]  D. N. Spergel et al. First year Wilkinson Microwave Anisotropy Probe (WMAP) observations: Determination of cosmological parameters. *Astrophys. J. Suppl.*, 148:175–194, 2003.

[4]  Dominik J. Schwarz, Craig J. Copi, Dragan Huterer, and Glenn D. Starkman. CMB Anomalies after Planck. *Arxiv pre-print*, 1510.07929, 2015.

[5]  P. A. R. Ade et al. Planck 2013 results. XXIII. Isotropy and statistics of the CMB. *Astron. Astrophys.*, 571:A23, 2014.

[6]  P. A. R. Ade et al. Planck 2015 results. XVI. Isotropy and statistics of the CMB. *Arxiv pre-print*, 1506.07135, 2015.

[7]  D. Blas, J. Lesgourgues, and T. Tram. The Cosmic Linear Anisotropy Solving System (CLASS). Part II: Approximation schemes. *JCAP*, 7:34, 2011.

[8]  P. A. R. Ade et al. Planck 2015 results. XIII. Cosmological parameters. *Arxiv pre-print*, 1502.01589, 2015.

[9]  A. Einstein. Die grundlage der allgemeinen relativittstheorie. *Annalen der Physik*, 354(7):769–822, 1916.

[10]  A. Friedman. Über die krümmung des raumes. *Zeitschrift für Physik*, 10(1):377–386, 1922.

[11]  Alan H. Guth. Inflationary universe: A possible solution to the horizon and flatness problems. *Phys. Rev. D*, 23:347–356, 1981.

[12]  K. N. Abazajian et al. Inflation Physics from the Cosmic Microwave Background and Large Scale Structure. *Astropart. Phys.*, 63:55–65, 2015.

[13] James M. Bardeen. Gauge-invariant cosmological perturbations. *Phys. Rev. D*, 22:1882–1905, 1980.

[14] James E. Lidsey, Andrew R. Liddle, Edward W. Kolb, Edmund J. Copeland, Tiago Barreiro, and Mark Abney. Reconstructing the inflaton potential¯an overview. *Rev. Mod. Phys.*, 69:373–410, 1997.

[15] P. A. R. Ade et al. Improved Constraints on Cosmology and Foregrounds from BICEP2 and Keck Array Cosmic Microwave Background Data with Inclusion of 95 GHz Band. *Phys. Rev. Lett.*, 116:031302, 2016.

[16] B. D. Sherwin, J. Dunkley, S. Das, et al. Evidence for Dark Energy from the Cosmic Microwave Background Alone Using the Atacama Cosmology Telescope Lensing Measurements. *Physical Review Letters*, 107(2):021302, 2011.

[17] Sean M. Carroll. The Cosmological constant. *Living Rev. Rel.*, 4:1, 2001.

[18] S. Tsujikawa. Quintessence: a review. *Classical and Quantum Gravity*, 30(21):214003, November 2013.

[19] Edmund J. Copeland, M. Sami, and Shinji Tsujikawa. Dynamics of dark energy. *Int. J. Mod. Phys.*, D15:1753–1936, 2006.

[20] P. A. R. Ade et al. Planck 2015 results. XIV. Dark energy and modified gravity. *ArXiv pre-print*, 1502.01590, 2015.

[21] A. A. Penzias and R. W. Wilson. A Measurement of Excess Antenna Temperature at 4080 Mc/s. *Astrophys. J.*, 142:419–421, 1965.

[22] R. A. Alpher, H. Bethe, and G. Gamow. The origin of chemical elements. *Phys. Rev.*, 73:803–804, 1948.

[23] R. H. Dicke, P. J. E. Peebles, P. G. Roll, and D. T. Wilkinson. Cosmic Black-Body Radiation. *Astrophys. J.*, 142:414–419, 1965.

[24] J. C. Mather et al. A preliminary measurement of the cosmic microwave background spectrum by the Cosmic Background Explorer (COBE) satellite. *Astrophys. J. Lett.*, 354:L37–L40, 1990.

[25] J. C. Mather et al. Measurement of the cosmic microwave background spectrum by the COBE FIRAS instrument. *Astrophys. J.*, 420:439–444, 1994.

[26] D. J. Fixsen. The Temperature of the Cosmic Microwave Background. *Astrophys. J.*, 707:916–920, 2009.

[27] G. F. Smoot et al. Structure in the COBE differential microwave radiometer first-year maps. *Astrophys. J. Lett.*, 396:L1–L5, 1992.

[28] U. Seljak and M. Zaldarriaga. A Line-of-Sight Integration Approach to Cosmic Microwave Background Anisotropies. *Astrophys. J.*, 469:437, 1996.

[29] W. Hu, N. Sugiyama, and J. Silk. The Physics of Microwave Background Anisotropies. *ArXiv Astrophysics e-prints*, April 1996.

[30] Marc Kamionkowski, Arthur Kosowsky, and Albert Stebbins. Statistics of cosmic microwave background polarization. *Phys. Rev.*, D55:7368–7388, 1997.

[31] Amanda Yoho, Simone Aiola, Craig J. Copi, Arthur Kosowsky, and Glenn D. Starkman. Microwave Background Polarization as a Probe of Large-Angle Correlations. *Phys. Rev.*, D91(12):123504, 2015.

[32] P. A. R. Ade et al. Planck 2013 results. XVI. Cosmological parameters. *Astron. Astrophys.*, 571:A16, 2014.

[33] R. Adam et al. Planck 2015 results. I. Overview of products and scientific results. 2015.

[34] C. L. Bennett et al. Four year COBE DMR cosmic microwave background observations: Maps and basic results. *Astrophys. J.*, 464:L1–L4, 1996.

[35] Craig J. Copi, Dragan Huterer, Dominik J. Schwarz, and Glenn D. Starkman. Large angle anomalies in the CMB. *Adv. Astron.*, 2010:847541, 2010.

[36] Craig J. Copi, Dragan Huterer, Dominik J. Schwarz, and Glenn D. Starkman. No large-angle correlations on the non-Galactic microwave sky. *Mon. Not. Roy. Astron. Soc.*, 399:295–303, 2009.

[37] C. J. Copi, D. Huterer, D. J. Schwarz, and G. D. Starkman. Large-Angle CMB Suppression and Polarization Predictions. *Mon. Not. Roy. Astron. Soc.*, 434:3590–3596, 2013.

[38] A. Yoho, C. J. Copi, G. D. Starkman, and A. Kosowsky. Probing Large-Angle Correlations with the Microwave Background Temperature and Lensing Cross Correlation. *Mon. Not. Roy. Astron. Soc.*, 442(3):2392–2397, 2014.

[39] Matias Zaldarriaga and Uros Seljak. An all sky analysis of polarization in the microwave background. *Phys. Rev.*, D55:1830–1840, 1997.

[40] Daniel Baumann and Matias Zaldarriaga. Causality and Primordial Tensor Modes. *JCAP*, 0906:013, 2009.

[41] LLoyd Knox. Determination of inflationary observables by cosmic microwave background anisotropy experiments. *Phys. Rev.*, D52:4307–4318, 1995.

[42] P. A. R. Ade et al. Planck 2013 results. I. Overview of products and scientific results. *Astron. Astrophys.*, 571:A1, 2014.

[43] A. Kogut, D. J. Fixsen, et al. The Primordial Inflation Explorer (PIXIE): a nulling polarimeter for cosmic microwave background observations. *JCAP*, 7:025, 2011.

[44] Philippe Andre et al. PRISM (Polarized Radiation Imaging and Spectroscopy Mission): A White Paper on the Ultimate Polarimetric Spectro-Imaging of the Microwave and Far-Infrared Sky. 2013.

[45] Simone Aiola, Bingjie Wang, Arthur Kosowsky, Tina Kahniashvili, and Hassan Firouzjahi. Microwave Background Correlations from Dipole Anisotropy Modulation. *Phys. Rev.*, D92:063008, 2015.

[46] C. L. Bennett, M. Halpern, G. Hinshaw, N. Jarosik, A. Kogut, M. Limon, S. S. Meyer, L. Page, D. N. Spergel, G. S. Tucker, E. Wollack, E. L. Wright, et al. First-Year Wilkinson Microwave Anisotropy Probe (WMAP) Observations: Preliminary Maps and Basic Results. *Astrophys. J. Suppl. Ser.*, 148:1–27, 2003.

[47] H. K. Eriksen, F. K. Hansen, A. J. Banday, K. M. Górski, and P. B. Lilje. Asymmetries in the Cosmic Microwave Background Anisotropy Field. *Astrophys. J.*, 605:14–20, 2004.

[48] F. K. Hansen, A. J. Banday, and K. M. Górski. Testing the cosmological principle of isotropy: local power-spectrum estimates of the WMAP data. *Mon. Not. R. Astron Soc.*, 354:641–665, 2004.

[49] M. Axelsson, Y. Fantaye, F. K. Hansen, A. J. Banday, H. K. Eriksen, and K. M. Gorski. Directional Dependence of ΛCDM Cosmological Parameters. *Astrophys. J. Lett.*, 773:L3, 2013.

[50] Y. Akrami, Y. Fantaye, A. Shafieloo, H. K. Eriksen, F. K. Hansen, A. J. Banday, and K. M. Górski. Power Asymmetry in WMAP and Planck Temperature Sky Maps as Measured by a Local Variance Estimator. *Astrophys. J. Lett.*, 784:L42, 2014.

[51] S. Adhikari. Local variance asymmetries in Planck temperature anisotropy maps. *Mon. Not. R. Astron Soc.*, 446:4232–4238, 2015.

[52] S. Flender and S. Hotchkiss. The small scale power asymmetry in the cosmic microwave background. *J. Cosmol. Astropart. Phys.*, 9:33, 2013.

[53] C. Gordon, W. Hu, D. Huterer, and T. Crawford. Spontaneous isotropy breaking: A mechanism for CMB multipole alignments. *Phys. Rev. D*, 72(10):103002, 2005.

[54] H. K. Eriksen, A. J. Banday, K. M. Górski, F. K. Hansen, and P. B. Lilje. Hemispherical Power Asymmetry in the Third-Year Wilkinson Microwave Anisotropy Probe Sky Maps. *Astrophys. J. Lett.*, 660:L81–L84, 2007.

[55] J. Hoftuft, H. K. Eriksen, A. J. Banday, K. M. Górski, F. K. Hansen, and P. B. Lilje. Increasing Evidence for Hemispherical Power Asymmetry in the Five-Year WMAP Data. *Astrophys. J.*, 699:985–989, 2009.

[56] D. Hanson and A. Lewis. Estimators for CMB statistical anisotropy. *Phys. Rev. D*, 80(6):063004, 2009.

[57] S. Prunet, J.-P. Uzan, F. Bernardeau, and T. Brunier. Constraints on mode couplings and modulation of the CMB with WMAP data. *Phys. Rev. D*, 71(8):083508, 2005.

[58] Adam Moss, Douglas Scott, James P. Zibin, and Richard Battye. Tilted physics: A cosmologically dipole-modulated sky. *Phys. Rev. D*, 84:023014, 2011.

[59] P. K. Rath and P. Jain. Testing the dipole modulation model in CMBR. *J. Cosmol. Astropart. Phys.*, 12:14, 2013.

[60] A. Kosowsky and T. Kahniashvili. Signature of Local Motion in the Microwave Sky. *Phys. Rev. Lett.*, 106(19):191301, 2011.

[61] L. Amendola, R. Catena, I. Masina, A. Notari, M. Quartin, and C. Quercellini. Measuring our peculiar velocity on the CMB with high-multipole off-diagonal correlations. *J. Cosmol. Astropart. Phys.*, 7:27, 2011.

[62] Planck Collaboration. Planck 2013 results. XXVII. Doppler boosting of the CMB: Eppur si muove. *Astron. Astrophys.*, 571:A27, 2014.

[63] D. Jeong, J. Chluba, L. Dai, M. Kamionkowski, and X. Wang. Effect of aberration on partial-sky measurements of the cosmic microwave background temperature power spectrum. *Phys. Rev. D*, 89(2):023003, 2014.

[64] A. Hajian and T. Souradeep. Measuring the Statistical Isotropy of the Cosmic Microwave Background Anisotropy. *Astrophys. J. Lett.*, 597:L5–L8, 2003.

[65] K. M. Górski, E. Hivon, A. J. Banday, B. D. Wandelt, F. K. Hansen, M. Reinecke, and M. Bartelmann. HEALPix: A Framework for High-Resolution Discretization and Fast Analysis of Data Distributed on the Sphere. *Astrophys. J.*, 622:759–771, 2005.

[66] Planck Collaboration. Planck 2013 results. XII. Diffuse component separation. *Astron. Astrophys.*, 571:A12, 2014.

[67] J. Bobin, F. Sureau, J.-L. Starck, A. Rassat, and P. Paykari. Joint Planck and WMAP CMB map reconstruction. *Astron. Astrophys.*, 563:A105, 2014.

[68] D. Foreman-Mackey, D. W. Hogg, D. Lang, and J. Goodman. emcee: The MCMC Hammer. *Publ. Astron. Soc. Pac.*, 125:306–312, 2013.

[69] A. Challinor and F. van Leeuwen. Peculiar velocity effects in high-resolution microwave background experiments. *Phys. Rev. D*, 65(10):103001, 2002.

[70] A. R. Liddle. Information criteria for astrophysical model selection. *Mon. Not. R. Astron Soc.*, 377:L74–L78, May 2007.

[71] Robert E. Kass and Adrian E. Raftery. Bayes factors. *Journal of the American Statistical Association*, 90(430):pp. 773–795, 1995.

[72] A. L. Erickcek, M. Kamionkowski, and S. M. Carroll. A hemispherical power asymmetry from inflation. *Phys. Rev. D*, 78(12):123520, 2008.

[73] A. L. Erickcek, S. M. Carroll, and M. Kamionkowski. Superhorizon perturbations and the cosmic microwave background. *Phys. Rev. D*, 78(8):083012, 2008.

[74] A. L. Erickcek, C. M. Hirata, and M. Kamionkowski. A scale-dependent power asymmetry from isocurvature perturbations. *Phys. Rev. D*, 80(8):083507, 2009.

[75] L. Dai, D. Jeong, M. Kamionkowski, and J. Chluba. The pesky power asymmetry. *Phys. Rev. D*, 87(12):123005, 2013.

[76] D. H. Lyth. The CMB modulation from inflation. *J. Cosmol. Astropart. Phys.*, 8:7, 2013.

[77] J. F. Donoghue, K. Dutta, and A. Ross. Nonisotropy in the CMB power spectrum in single field inflation. *Phys. Rev. D*, 80(2):023526, 2009.

[78] L. Wang and A. Mazumdar. Small non-Gaussianity and dipole asymmetry in the cosmic microwave background. *Phys. Rev. D*, 88(2):023512, 2013.

[79] Z.-G. Liu, Z.-K. Guo, and Y.-S. Piao. Obtaining the CMB anomalies with a bounce from the contracting phase to inflation. *Phys. Rev. D*, 88(6):063539, 2013.

[80] J. McDonald. Isocurvature and curvaton perturbations with red power spectrum and large hemispherical asymmetry. *J. Cosmol. Astropart. Phys.*, 7:43, 2013.

[81] A. R. Liddle and M. Cortês. Cosmic Microwave Background Anomalies in an Open Universe. *Phys. Rev. Lett.*, 111(11):111302, 2013.

[82] A. Mazumdar and L. Wang. CMB dipole asymmetry from a fast roll phase. *J. Cosmol. Astropart. Phys.*, 10:49, 2013.

[83] G. D'Amico, R. Gobbetti, M. Kleban, and M. Schillo. Large-scale anomalies from primordial dissipation. *J. Cosmol. Astropart. Phys.*, 11:13, 2013.

[84] Y.-F. Cai, W. Zhao, and Y. Zhang. Cosmic microwave background power asymmetry from primordial sound speed parameter. *Phys. Rev. D*, 89(2):023005, 2014.

[85] Z. Chang, X. Li, and S. Wang. Quadrupole–octopole alignment of CMB related to primordial power spectrum with dipolar modulation in anisotropic spacetime. 2013.

[86] K. Kohri, C.-M. Lin, and T. Matsuda. Scale-dependent CMB asymmetry from primordial configuration. *J. Cosmol. Astropart. Phys.*, 8:26, 2014.

[87] J. McDonald. Hemispherical power asymmetry from scale-dependent modulated re-heating. *J. Cosmol. Astropart. Phys.*, 11:41, 2013.

[88] S. Kanno, M. Sasaki, and T. Tanaka. A viable explanation of the CMB dipolar statistical anisotropy. *Progress of Theoretical and Experimental Physics*, 2013(11):110001, 2013.

[89] Z.-G. Liu, Z.-K. Guo, and Y.-S. Piao. CMB anomalies from an inflationary model in string theory. *European Physical Journal C*, 74:3006, 2014.

[90] Z. Chang and S. Wang. Implications of primordial power spectra with statistical anisotropy on CMB temperature fluctuation and polarizations. 2013.

[91] J. McDonald. Hemispherical power asymmetry from a space-dependent component of the adiabatic power spectrum. *Phys. Rev. D*, 89(12):127303, 2014.

[92] M. H. Namjoo, S. Baghram, and H. Firouzjahi. Hemispherical asymmetry and local non-Gaussianity: A consistency condition. *Phys. Rev. D*, 88(8):083527, 2013.

[93] A. Akbar Abolhasani, S. Baghram, H. Firouzjahi, and M. H. Namjoo. Asymmetric Sky from the Long Mode Modulations. 2013.

[94] H. Firouzjahi, J.-O. Gong, and M. H. Namjoo. Scale-dependent hemispherical asymmetry from general initial state during inflation. *J. Cosmol. Astropart. Phys.*, 11:37, 2014.

[95] M. H. Namjoo, A. Akbar Abolhasani, S. Baghram, and H. Firouzjahi. CMB hemispherical asymmetry: long mode modulation and non-Gaussianity. *J. Cosmol. Astropart. Phys.*, 8:2, 2014.

[96] M. Zarei. Dipole Modulation in Tensor Modes: Signatures in CMB Polarization. 2014.

[97] M. H. Namjoo, A. A. Abolhasani, H. Assadullahi, S. Baghram, H. Firouzjahi, and D. Wands. Expected dipole asymmetry in CMB polarization. *J. Cosmol. Astropart. Phys.*, 5:15, 2015.

[98] C. T. Byrnes and E. R. M. Tarrant. Scale-dependent non-Gaussianity and the CMB Power Asymmetry. 2015.

[99] T. Kobayashi, M. Cortês, and A. R. Liddle. A separate universe view of the asymmetric sky. *J. Cosmol. Astropart. Phys.*, 5:29, 2015.

[100] S. Jazayeri, Y. Akrami, H. Firouzjahi, A. R. Solomon, and Y. Wang. Inflationary power asymmetry from primordial domain walls. *J. Cosmol. Astropart. Phys.*, 11:44, 2014.

[101] E. Calabrese, R. Hložek, N. Battaglia, et al. Precision epoch of reionization studies with next-generation CMB experiments. *J. Cosmol. Astropart. Phys.*, 8:10, 2014.

[102] Simone Aiola, Arthur Kosowsky, and Bingjie Wang. Gaussian Approximation of Peak Values in the Integrated Sachs-Wolfe Effect. *Phys. Rev.*, D91:043510, 2015.

[103] A. van Engelen, R. Keisler, O. Zahn, et al. A Measurement of Gravitational Lensing of the Microwave Background Using South Pole Telescope Data. *Astrophys. J.*, 756:142, 2012.

[104] T. Delubac et al. Baryon Acoustic Oscillations in the Ly{\alpha} forest of BOSS DR11 quasars. *ArXiv e-prints*, 2014.

[105] R. K. Sachs and A. M. Wolfe. Perturbations of a Cosmological Model and Angular Variations of the Microwave Background. *Astrophys. J.*, 147:73, 1967.

[106] M. Kamionkowski and D. N. Spergel. Large-angle cosmic microwave background anisotropies in an open universe. *Astrophys. J.*, 432:7–16, 1994.

[107] T. Giannantonio, R. Scranton, R. G. Crittenden, R. C. Nichol, S. P. Boughn, A. D. Myers, and G. T. Richards. Combined analysis of the integrated Sachs-Wolfe effect and cosmological implications. *Phys. Rev. D*, 77(12):123520, 2008.

[108] R. G. Crittenden and N. Turok. Looking for a Cosmological Constant with the Rees-Sciama Effect. *Phys. Rev. Lett.*, 76:575–578, 1996.

[109] P. Fosalba and E. Gaztañaga. Measurement of the gravitational potential evolution from the cross-correlation between WMAP and the APM Galaxy Survey. *Mon. Not. R. Astron Soc.*, 350:L37–L41, 2004.

[110] C. L. Francis and J. A. Peacock. Integrated Sachs-Wolfe measurements with photometric redshift surveys: 2MASS results and future prospects. *Mon. Not. R. Astron Soc.*, 406:2–13, 2010.

[111] N. Afshordi, Y.-S. Loh, and M. A. Strauss. Cross-correlation of the cosmic microwave background with the 2MASS galaxy survey: Signatures of dark energy, hot gas, and point sources. *Phys. Rev. D*, 69(8):083524, 2004.

[112] S. Boughn and R. Crittenden. A correlation between the cosmic microwave background and large-scale structure in the Universe. *Nature*, 427:45–47, 2004.

[113] M. R. Nolta et al. First Year Wilkinson Microwave Anisotropy Probe Observations: Dark Energy Induced Correlation with Radio Sources. *Astrophys. J.*, 608:10–15, 2004.

[114] N. Padmanabhan, C. M. Hirata, U. Seljak, D. J. Schlegel, J. Brinkmann, and D. P. Schneider. Correlating the CMB with luminous red galaxies: The integrated Sachs-Wolfe effect. *Phys. Rev. D*, 72(4):043525, 2005.

[115] A. Rassat, K. Land, O. Lahav, and F. B. Abdalla. Cross-correlation of 2MASS and WMAP 3: implications for the integrated Sachs-Wolfe effect. *Mon. Not. R. Astron Soc.*, 377:1085–1094, 2007.

[116] U. Sawangwit, T. Shanks, R. D. Cannon, S. M. Croom, N. P. Ross, and D. A. Wake. Cross-correlating WMAP5 with 1.5 million LRGs: a new test for the ISW effect. *Mon. Not. R. Astron Soc.*, 402:2228–2244, 2010.

[117] P. Vielva, E. Martínez-González, and M. Tucci. Cross-correlation of the cosmic microwave background and radio galaxies in real, harmonic and wavelet spaces: detection of the integrated Sachs-Wolfe effect and dark energy constraints. *Mon. Not. R. Astron Soc.*, 365:891–901, 2006.

[118] A. Cabré, E. Gaztañaga, M. Manera, P. Fosalba, and F. Castander. Cross-correlation of Wilkinson Microwave Anisotropy Probe third-year data and the Sloan Digital Sky Survey DR4 galaxy survey: new evidence for dark energy. *Mon. Not. R. Astron Soc.*, 372:L23–L27, 2006.

[119] S. Ho, C. Hirata, N. Padmanabhan, U. Seljak, and N. Bahcall. Correlation of CMB with large-scale structure. I. Integrated Sachs-Wolfe tomography and cosmological implications. *Phys. Rev. D*, 78(4):043519, 2008.

[120] Planck Collaboration. Planck 2013 results. XIX. The integrated Sachs-Wolfe effect. *ArXiv e-prints*, 2013.

[121] C. Hernández-Monteagudo, A. J. Ross, et al. The SDSS-III Baryonic Oscillation Spectroscopic Survey: constraints on the integrated Sachs-Wolfe effect. *Mon. Not. R. Astron Soc.*, 438:1724–1740, 2014.

[122] A. Kovács, I. Szapudi, B. R. Granett, and Z. Frei. Cross-correlation of WMAP7 and the WISE full data release. *Mon. Not. R. Astron Soc.*, 431:L28–L32, 2013.

[123] S. Ferraro, B. D. Sherwin, and D. N. Spergel. A WISE measurement of the ISW effect. *ArXiv e-prints*, 2014.

[124] A. J. Nishizawa. Integrated Sachs Wolfe Effect and Rees Sciama Effect. *ArXiv e-prints*, 2014.

[125] B. R. Granett, M. C. Neyrinck, and I. Szapudi. An Imprint of Superstructures on the Microwave Background due to the Integrated Sachs-Wolfe Effect. *Astrophys. J.*, 683:L99–L102, 2008.

[126] G. Hinshaw, J. L. Weiland, R. S. Hill, N. Odegard, D. Larson, et al. Five-Year Wilkinson Microwave Anisotropy Probe Observations: Data Processing, Sky Maps, and Basic Results. *ApJS*, 180:225–245, 2009.

[127] J. K. Adelman-McCarthy et al. The Sixth Data Release of the Sloan Digital Sky Survey. *ApJS*, 175:297–313, 2008.

[128] C. Hernández-Monteagudo and R. E. Smith. On the signature of z 0.6 superclusters and voids in the Integrated Sachs-Wolfe effect. *Mon. Not. R. Astron Soc.*, 435:1094–1107, 2013.

[129] B. R. Granett, M. C. Neyrinck, and I. Szapudi. Dark Energy Detected with Supervoids and Superclusters. *ArXiv e-prints*, 2008.

[130] S. Nadathur, S. Hotchkiss, and S. Sarkar. The integrated Sachs-Wolfe imprint of cosmic superstructures: a problem for $\Lambda$CDM. *JCAP*, 6:42, 2012.

[131] S. Flender, S. Hotchkiss, and S. Nadathur. The stacked ISW signal of rare superstructures in $\Lambda$CDM. *JCAP*, 2:13, 2013.

[132] M. J. Rees and D. W. Sciama. Large-scale Density Inhomogeneities in the Universe. *Nature*, 217:511–516, 1968.

[133] Y.-C. Cai, B. Li, S. Cole, C. S. Frenk, and M. Neyrinck. The integrated Sachs-Wolfe effect in f(R) gravity. *Mon. Not. R. Astron Soc.*, 439:2978–2989, 2014.

[134] B. Chen, R. Kantowski, and X. Dai. Embedded Lensing Time Delays, the Fermat Potential, and the Integrated Sachs-Wolfe Effect. *ArXiv e-prints*, 2013.

[135] P. Pápai, I. Szapudi, and B. R. Granett. Integrated Sachs-Wolfe Imprint of Superstructures on Linear Scales. *Astrophys. J.*, 732:27, 2011.

[136] W. A. Watson et al. The Jubilee ISW project - I. Simulated ISW and weak lensing maps and initial power spectra results. *Mon. Not. R. Astron Soc.*, 438:412–425, 2014.

[137] S. Hotchkiss, S. Nadathur, S. Gottlöber, I. T. Iliev, A. Knebe, W. A. Watson, and G. Yepes. The Jubilee ISW Project II: observed and simulated imprints of voids and superclusters on the cosmic microwave background. *ArXiv e-prints*, 2014.

[138] G. Hinshaw, D. Larson, E. Komatsu, D. N. Spergel, et al. Nine-year Wilkinson Microwave Anisotropy Probe (WMAP) Observations: Cosmological Parameter Results. *ApJS*, 208:19, 2013.

[139] Planck collaboration. Planck 2013 results. XV. CMB power spectra and likelihood. *ArXiv e-prints*, 2013.

[140] R. E. Smith, J. A. Peacock, A. Jenkins, S. D. M. White, C. S. Frenk, F. R. Pearce, P. A. Thomas, G. Efstathiou, and H. M. P. Couchman. Stable clustering, the halo model and non-linear cosmological power spectra. *Mon. Not. R. Astron Soc.*, 341:1311–1332, 2003.

[141] S. Aiola, A. Kosowsky, and B. Wang - In preparation.

[142] S. Ilić, M. Langer, and M. Douspis. Detecting the integrated Sachs-Wolfe effect with stacked voids. *A&A* , 556:A51, 2013.

[143] S. C. Keller, B. P. Schmidt, et al. The SkyMapper Telescope and The Southern Sky Survey. *PASA*, 24:1–12, 2007.

[144] LSST Science Collaboration. LSST Science Book, Version 2.0. *ArXiv e-prints*, 2009.

[145] R. Dünner, M. Hasselfield, T. A. Marriage, J. Sievers, et al. The Atacama Cosmology Telescope: Data Characterization and Mapmaking. *Astrophys. J.*, 762:10, 2013.

[146] S. Naess, M. Hasselfield, J. McMahon, M. D. Niemack, et al. The Atacama Cosmology Telescope: CMB polarization at 200 l 9000. *JCAP*, 10:007, 2014.

[147] G. E. Addison, Y. Huang, D. J. Watts, C. L. Bennett, M. Halpern, G. Hinshaw, and J. L. Weiland. Quantifying discordance in the 2015 Planck CMB spectrum. *Astrophys. J.*, 818(2):132, 2016.

[148] Silvia Galli, Karim Benabed, Franois Bouchet, Jean-Franois Cardoso, Franz Elsner, Eric Hivon, Anna Mangilli, Simon Prunet, and Benjamin Wandelt. CMB Polarization can constrain cosmology better than CMB temperature. *Phys. Rev.*, D90(6):063504, 2014.

[149] R. J. Thornton et al. The Atacama Cosmology Telescope: The polarization-sensitive ACTPol instrument. *ArXiv e-prints*, 2016.

[150] F. De Bernardis, J. R. Stevens, M. Hasselfield, et al. Survey strategy optimization for the Atacama Cosmology Telescope. *ArXiv e-prints*, 2016.

[151] J.-C. Hamilton. CMB map-making and power spectrum estimation. *ArXiv Astrophysics e-prints*, October 2003.

[152] C. M. Cantalupo, J. D. Borrill, A. H. Jaffe, T. S. Kisner, and R. Stompor. MADmap: A Massively Parallel Maximum Likelihood Cosmic Microwave Background Map-maker. *Astrophys. J. Supp.*, 187:212–227, 2010.

[153] M. Tegmark. How to Make Maps from Cosmic Microwave Background Data without Losing Information. *Astrophys. J. Lett.*, 480:L87–L90, 1997.

[154] Emmanuel Schaan et al. Evidence for the kinematic Sunyaev-Zeľdovich effect with ACTPol and velocity reconstruction from BOSS. *Phys. Rev.*, D93(8):082002, 2016.

[155] F. De Bernardis, S. Aiola, E. M. Vavagiakis, M. D. Niemack, N. Battaglia, et al. Detection of the pairwise kinematic Sunyaev-Zel'dovich effect with BOSS DR11 and the Atacama Cosmology Telescope. *ArXiv e-prints*, 2016.